

..... NNT/NL : 2020AIXM0001/001ED000

# Habilitation à Diriger des Recherches

Présentée à Aix-Marseille Université

le XX janvier 2022 par

**Julián Ernesto BAUTISTA**

Dark-energy with Spectroscopic Observations of the Universe

**Discipline**

Physique et Sciences de la Matière

**Spécialité**

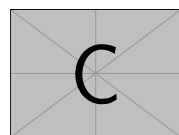
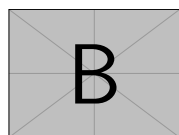
Astrophysique et Cosmologie

**Laboratoire**

Centre de Physique des Particules de Marseille

**Composition du jury**

•	Prénom NOM	Rapporteur·e
•	Affiliation	
•	Prénom NOM	Rapporteur·e
•	Affiliation	
•	Prénom NOM	Examinateur·rice
•	Affiliation	
•	Prénom NOM	Président·e du jury
•	Affiliation	
	Prénom NOM	Tuteur
	Affiliation	



Je soussigné, Julián Ernesto Bautista, déclare par la présente que le travail présenté dans ce manuscrit est mon propre travail, dans le respect des principes d'honnêteté, d'intégrité et de responsabilité inhérents à la mission de recherche. Les travaux de recherche et la rédaction de ce manuscrit ont été réalisés dans le respect à la fois de la charte nationale de déontologie des métiers de la recherche et de la charte d'Aix-Marseille Université relative à la lutte contre le plagiat.

Ce travail n'a pas été précédemment soumis en France ou à l'étranger dans une version identique ou similaire à un organisme examinateur.

Fait à Marseille, le [date]



Cette œuvre est mise à disposition selon les termes de la [Licence Creative Commons Attribution - Pas d'Utilisation Commerciale - Pas de Modification 4.0 International](#).

# Résumé

Lorem ipsum dolor sit amet, consectetuer adipiscing elit. Ut purus elit, vestibulum ut, placerat ac, adipiscing vitae, felis. Curabitur dictum gravida mauris. Nam arcu libero, nonummy eget, consectetuer id, vulputate a, magna. Donec vehicula augue eu neque. Pellentesque habitant morbi tristique senectus et netus et malesuada fames ac turpis egestas. Mauris ut leo. Cras viverra metus rhoncus sem. Nulla et lectus vestibulum urna fringilla ultrices. Phasellus eu tellus sit amet tortor gravida placerat. Integer sapien est, iaculis in, pretium quis, viverra ac, nunc. Praesent eget sem vel leo ultrices bibendum. Aenean faucibus. Morbi dolor nulla, malesuada eu, pulvinar at, mollis ac, nulla. Curabitur auctor semper nulla. Donec varius orci eget risus. Duis nibh mi, congue eu, accumsan eleifend, sagittis quis, diam. Duis eget orci sit amet orci dignissim rutrum.

Mots clés: géométrie algorithmique, complexe planaire et rectangulaire, géodésique, courbure globale non-positive

# Abstract

Lorem ipsum dolor sit amet, consectetuer adipiscing elit. Ut purus elit, vestibulum ut, placerat ac, adipiscing vitae, felis. Curabitur dictum gravida mauris. Nam arcu libero, nonummy eget, consectetuer id, vulputate a, magna. Donec vehicula augue eu neque. Pellentesque habitant morbi tristique senectus et netus et malesuada fames ac turpis egestas. Mauris ut leo. Cras viverra metus rhoncus sem. Nulla et lectus vestibulum urna fringilla ultrices. Phasellus eu tellus sit amet tortor gravida placerat. Integer sapien est, iaculis in, pretium quis, viverra ac, nunc. Praesent eget sem vel leo ultrices bibendum. Aenean faucibus. Morbi dolor nulla, malesuada eu, pulvinar at, mollis ac, nulla. Curabitur auctor semper nulla. Donec varius orci eget risus. Duis nibh mi, congue eu, accumsan eleifend, sagittis quis, diam. Duis eget orci sit amet orci dignissim rutrum.

Keywords: computational geometry, planar and rectangular complex, geodesic, global nonpositive curvature

# Acknowledgements

Le modèle de thèse AMU n'existerait pas sans la contribution des doctorants. Nous souhaitons remercier tout particulièrement [Mickaël Bojados](#), [Flora Cordoleani](#) et [Florian Caullery](#) pour leur aide précieuse et la qualité de leurs fichiers sources LaTeX. La mise à jour effectuée en 2018 doit beaucoup à l'excellent travail de [Dorian Depriester](#).

Lorem ipsum dolor sit amet, consectetuer adipiscing elit. Ut purus elit, vestibulum ut, placeat ac, adipiscing vitae, felis. Curabitur dictum gravida mauris. Nam arcu libero, nonummy eget, consectetuer id, vulputate a, magna. Donec vehicula augue eu neque. Pellentesque habitant morbi tristique senectus et netus et malesuada fames ac turpis egestas. Mauris ut leo. Cras viverra metus rhoncus sem. Nulla et lectus vestibulum urna fringilla ultrices. Phasellus eu tellus sit amet tortor gravida placerat. Integer sapien est, iaculis in, pretium quis, viverra ac, nunc. Praesent eget sem vel leo ultrices bibendum. Aenean faucibus. Morbi dolor nulla, malesuada eu, pulvinar at, mollis ac, nulla. Curabitur auctor semper nulla. Donec varius orci eget risus. Duis nibh mi, congue eu, accumsan eleifend, sagittis quis, diam. Duis eget orci sit amet orci dignissim rutrum.

Nam dui ligula, fringilla a, euismod sodales, sollicitudin vel, wisi. Morbi auctor lorem non justo. Nam lacus libero, pretium at, lobortis vitae, ultricies et, tellus. Donec aliquet, tortor sed accumsan bibendum, erat ligula aliquet magna, vitae ornare odio metus a mi. Morbi ac orci et nisl hendrerit mollis. Suspendisse ut massa. Cras nec ante. Pellentesque a nulla. Cum sociis natoque penatibus et magnis dis parturient montes, nascetur ridiculus mus. Aliquam tincidunt urna. Nulla ullamcorper vestibulum turpis. Pellentesque cursus luctus mauris.

# Contents

<b>Résumé</b>	<b>3</b>
<b>Abstract</b>	<b>4</b>
<b>Acknowledgements</b>	<b>5</b>
<b>Contents</b>	<b>6</b>
<b>1 Introduction</b>	<b>8</b>
1.1 The history of our Universe and its big open questions . . . . .	8
1.2 Evidences for the accelerated expansion of the Universe . . . . .	9
1.3 Model of an expanding Universe . . . . .	10
1.3.1 Assumptions and ingredients . . . . .	10
1.3.2 The expansion rate . . . . .	10
1.3.3 Distances in cosmology . . . . .	11
1.3.4 Dark-energy models . . . . .	12
1.4 Model of the large-scale structures . . . . .	12
1.4.1 Statistical description of perturbations . . . . .	13
1.4.2 Configuration and Fourier space . . . . .	14
1.4.3 Cosmological dependency of the power spectrum . . . . .	14
1.4.4 The amplitude of the power spectrum . . . . .	15
1.5 Cosmological probes of expansion . . . . .	16
1.5.1 Direct measurements of $H_0$ . . . . .	16
1.5.2 Type-Ia supernovae . . . . .	17
1.5.3 Big Bang nucleosynthesis . . . . .	18
1.5.4 Baryon acoustic oscillations . . . . .	19
1.5.5 The cosmic microwave background . . . . .	20
1.5.6 Redshift-space distortions . . . . .	21
1.5.7 Weak gravitational lensing . . . . .	23
<b>2 Observing the Universe with spectroscopy</b>	<b>24</b>
2.1 Selecting the objects to observe . . . . .	24
2.2 Pointing fibres to the sky . . . . .	25
2.3 From electrons to spectra . . . . .	26
2.4 From spectra to redshifts . . . . .	28
2.5 From redshifts to cosmology . . . . .	28
<b>3 The high-redshift Universe and its forests</b>	<b>29</b>
3.1 Forests as a tracer of the Universe's structures . . . . .	29
3.2 Baryon acoustic oscillations in the forests . . . . .	31
3.2.1 Transmission field . . . . .	32
3.2.2 Two-point correlation functions . . . . .	33

3.2.3	Correction matrices . . . . .	34
3.2.4	The model . . . . .	35
3.2.5	BAO constraints . . . . .	36
3.3	Impact of redshift errors . . . . .	38
3.4	Weak-lensing of forests . . . . .	41
3.5	Voids in tomographic maps . . . . .	44
<b>4</b>	<b>The mid-redshift Universe and its galaxies</b>	<b>45</b>
4.1	From redshifts to clustering catalogues . . . . .	45
4.2	Reconstruction of linear density field . . . . .	50
4.3	Mock catalogues . . . . .	51
4.4	From catalogues to clustering estimates . . . . .	52
4.4.1	Correlation function . . . . .	52
4.4.2	Power spectrum . . . . .	53
4.4.3	The clustering of eBOSS DR16 LRGs . . . . .	55
4.5	Baryon acoustic oscillations . . . . .	57
4.6	Redshift-space distortions . . . . .	59
4.7	Joint clustering analysis in Fourier and Configuration space . . . . .	63
4.8	Cross-correlation with radio surveys . . . . .	66
<b>5</b>	<b>The low-redshift Universe and its velocities</b>	<b>69</b>
5.1	Measuring peculiar velocities . . . . .	69
5.2	Combining velocities with densities . . . . .	69
5.3	Maximum likelihood method . . . . .	69
5.4	Testing general relativity with velocities . . . . .	69
<b>Conclusion</b>		<b>70</b>
<b>Bibliography</b>		<b>71</b>

# 1 Introduction

## Contents

1.1	The history of our Universe and its big open questions . . . . .	8
1.2	Evidences for the accelerated expansion of the Universe . . . . .	9
1.3	Model of an expanding Universe . . . . .	10
1.3.1	Assumptions and ingredients . . . . .	10
1.3.2	The expansion rate . . . . .	10
1.3.3	Distances in cosmology . . . . .	11
1.3.4	Dark-energy models . . . . .	12
1.4	Model of the large-scale structures . . . . .	12
1.4.1	Statistical description of perturbations . . . . .	13
1.4.2	Configuration and Fourier space . . . . .	14
1.4.3	Cosmological dependency of the power spectrum . . . . .	14
1.4.4	The amplitude of the power spectrum . . . . .	15
1.5	Cosmological probes of expansion . . . . .	16
1.5.1	Direct measurements of $H_0$ . . . . .	16
1.5.2	Type-Ia supernovae . . . . .	17
1.5.3	Big Bang nucleosynthesis . . . . .	18
1.5.4	Baryon acoustic oscillations . . . . .	19
1.5.5	The cosmic microwave background . . . . .	20
1.5.6	Redshift-space distortions . . . . .	21
1.5.7	Weak gravitational lensing . . . . .	23

### 1.1 The history of our Universe and its big open questions

If we gather all knowledge in physics humanity could learn to this day, we can build an interesting story for how our Universe evolved since *very* early times. This great story that can explain most of what we observe in the sky, while being consistent with experimental results here on Earth. However, this story has several weak spots. Either because where we do not have a satisfactory physical explanation for what we observe, or because we simply cannot observe what happens by then (and potentially we never will).

The story in a nutshell goes as follows: the “beginning” of the Universe<sup>1</sup>, also known as the *Big Bang* or *inflation*, was an epoch of exponential expansion of space that happened around 13.8 billion years ago. Inflation transformed quantum, microscopic fluctuations of space into macroscopic density fluctuations of the Universe’s constituents: quarks, photons,

---

<sup>1</sup>The actual beginning of the Universe can be seen as a complex philosophical question or simply as an ill defined physical concept. This discussion is clearly beyond the scope of this work and/or my capabilities. Here, I decide to name as beginning the first epoch of the Universe for which we have a widely known physical theory to describe it.

neutrinos and dark-matter. After inflation, the Universe continues to expand but much slowly. The average temperature of the Universe decreases adiabatically. Quarks start to gather to form protons, neutrons and relics of heavier atoms, such as deuterium, tritium, helium, lithium and so on. All this during the first few minutes of the Universe's history, in the so called *Big Bang nucleosynthesis*. After 380 thousand years, electrons rebind with protons to form neutral hydrogen, and photons scatter for their last time with them as the Universe becomes more diffuse. The photons from this epoch are observable today and are known as the *cosmic microwave background*. The Universe goes through its *dark ages*, where hydrogen is mostly neutral and stars have not yet formed. After several million years, gravity clumps hydrogen into dense clouds that reach high enough temperatures to start thermonuclear reactions in their core. The first stars are formed. Then the first galaxies. These galaxies merge into larger galaxies, galaxies form small virialized groups, large groups, clusters, super clusters. Clusters, filamentary structures and voids compose the so called cosmic web. At around half of the Universe's age, the expansion starts to speed up again, accelerating, as if gravity became repulsive on very large scales. Then, on one of the many billions of galaxies, the *Milky Way*, planet Earth formed around a somewhat isolated star, the Sun, and here we are today, observing the sky, trying to explain the whole Universe.

This story is based on the assumption that general relativity (GR) is the theory of gravity, that the Universe can be modelled as statistically homogeneous and isotropic on large enough scales, and that the Universe is composed of the standard model particles and interactions, with the addition of two exotic components: dark-energy and dark-matter.

The physical origin of dark-energy and dark-matter is a mystery and one of the weak spots of the Universe's story. Another weak spot is the physics of inflation, but observables related to that time are limited. [Any others ?] Solutions for these problems would represent major breakthroughs in physics and large teams of scientists are dedicated to them, either theoretically or experimentally.

My past work has been focused on the observations related to dark-energy. The rest of this chapter will be dedicated to explaining the problem of accelerated expansion, the dark-energy model and other possible solutions, and how do we observe the expansion.

## 1.2 Evidences for the accelerated expansion of the Universe

Not long after developing his theory of gravity, Einstein wanted to write a model for a static Universe filled with matter. Since gravity is attractive, his solution was to include a new constant term,  $\Lambda$ , in the equations. This will be later known as the *cosmological constant*, one of the simplest models of dark-energy in agreement with a wide variety of cosmological observations.

The first indirect evidences for dark-energy come from measurements of galaxy clustering in the 80's (Maddox et al. 1990; Efstathiou et al. 1990). At the end of the 90's, two independent teams measured the expansion of the Universe using type-Ia supernovae (Riess, Filippenko, et al. 1998; Perlmutter et al. 1999). Their observations could only be explained by an Universe containing around 30 per cent of matter and 70 per cent of dark energy, in the form of a cosmological constant. Few years later, first measurements of the temperature fluctuations in the cosmic microwave background were consistent with an Universe with a flat space (Balbi et al. 2000; de Bernardis et al. 2000), which in combination with measurements of clustering, supernovae and the local expansion rate (Mould et al. 2000), definitely confirmed that the Universe's expansion is accelerating. Age estimates of globular stellar clusters, which

are supposed to be among the oldest astrophysical objects, were also indicating that the Universe had to be older than the age predicted by models of an Universe only filled with matter (Chaboyer 1998). The following decade was enriched by the first measurements of the baryon acoustic oscillations in the distribution of galaxies (Eisenstein, Zehavi, et al. 2005; Cole et al. 2005), re-confirming the accelerated nature of the expansion.

Since the 2010's, we live in the so-called *precision cosmology* era, where several observatories were constructed with the main goal of improving the precision of all these measurements just discussed. Even with the most up-to-date results, with errors of the order of a few percent, there is yet no evidence for a departure from the model of Universe governed by GR, composed by 70 per cent of this mysterious cosmological constant and by 25 per cent by this mysterious dark-matter.

## 1.3 Model of an expanding Universe

### 1.3.1 Assumptions and ingredients

In order to define some important cosmological parameters, I will quickly review the basics of the current most accepted model for our Universe in the limit of very large scales, where it can be considered homogenous and isotropic. This is also known as the *background* model, since the formation of structures (see next section) can be modeled as small perturbations around it. It is also assumed that gravity is described by general relativity, which interlinks the fabric of space-time and energy densities of the Universe constituents. For these constituents, we assume the presence of *baryons* (protons, electrons, atoms), photons, neutrinos, cold dark-matter and dark-energy.

The expansion of space is usually parametrised by the scale factor  $a(t)$ , a function of time  $t$  that dictates how physical and comoving distances relate to each other. We assume that  $a(t_0) = 1$  today ( $t_0 = 13.8$  Gyr) and that  $a \rightarrow 0$  as  $t \rightarrow 0$ . The speed of the expansion and its acceleration are simply derivatives with respect to time,  $\dot{a}(t)$  and  $\ddot{a}(t)$ , respectively. The expansion rate of the Universe is defined as  $H(t) = \dot{a}(t)/a(t)$  and takes the Hubble constant value today,  $H(t_0) = H_0 = 100h$  km/s/Mpc  $\sim 70$  km/s/Mpc. Since the scale factor is a monotonically increasing function of time (in our simple model),  $a$  is commonly used to describe a given cosmic epoch.

One of the consequences of the expansion is that relativistic species, such as photons and massless neutrinos, loose energy or are *redshifted* as they propagate. In astronomy, the redshift  $z$  is defined as the relative difference in wavelength between the one emitted by source and the one observed. Thus, in an expanding Universe the scale factor is related to the redshift as  $a = 1/(1+z)$ . Redshift is also commonly used to describe cosmic epoch or distances. Today corresponds to  $z = 0$  while  $z \rightarrow \infty$  as  $t \rightarrow 0$ .

### 1.3.2 The expansion rate

The expansion rate can be derived from GR equations and be written as a function of redshift and the densities of each constituent

$$H^2(z) = H_0^2 [\Omega_m(1+z)^3 + \Omega_r(1+z)^4 + \Omega_{de}(z) + \Omega_k(1+z)^2] \quad (1.1)$$

where  $\Omega_x = \rho_x/\rho_{\text{crit}}$  is the ratio between the density constituent  $x$  today and the critical energy density  $\rho_{\text{crit}} = 3H_0^2/8\pi G$ , which is the density required for a flat space geometry. The

subscripts  $m$ ,  $r$ ,  $de$  and  $k$  stand for non-relativistic species (baryons, cold dark-matter and non-relativistic neutrinos), relativistic species (photons and relativistic neutrinos), dark-energy and curvature, respectively. The curvature “density” parameter is defined as a function of the others,  $\Omega_k = (1 - \sum_x \Omega_x)$ , and it is zero in a flat space geometry. Non-relativistic species dilute in an expanding universe so their energy density is proportional to  $a^{-3} = (1 + z)^3$ . Relativistic species dilute as well but have an extra factor of  $a^{-1}$  due to redshifting. Dark-energy is written as a general function of redshift. In the simplest case of a cosmological constant,  $\Omega_{de}(z) = \Omega_\Lambda$ , i.e. a constant. The dependency of curvature with  $a^{-2}$  simply comes from the field equations.

### 1.3.3 Distances in cosmology

Distances are non-trivially defined in an expanding, potentially non-flat, Universe. Therefore, different types of distances are more appropriate for certain observables. The *Hubble distance* is related to the expansion rate as

$$D_H(z) = \frac{c}{H(z)}, \quad (1.2)$$

and it is commonly used in measurements of baryon acoustic oscillations in the line-of-sight direction (see Chapters 3 and 4) or to represent the size of a causally connected region of the Universe.

The *comoving distance* to an object at redshift  $z$  is written as

$$D_C(z) = \int_0^z dz' D_H(z'). \quad (1.3)$$

This expression yields the distance travelled by a photon from a source towards us but factoring out the scale factor, effectively “removing” the effect of expansion.

The *comoving angular diameter distance*  $D_M(z)$  is useful when distances are inferred from angles, which are affected by the curvature of space. An object with comoving size  $l$  at a redshift  $z$  would be seen with an angular size  $\theta$ . This allows us to define  $D_M(z) = l/\theta(z)$  as

$$D_M(z) = D_C(z) \text{sinc}\left(\sqrt{-\Omega_k} \frac{D_C(z)}{D_H(z=0)}\right), \quad (1.4)$$

where  $\text{sinc}(x) = \sin(x)/x$ . This distance is used in observations of gravitational lensing and in measurements of the baryon acoustic oscillations in the transverse direction to the line-of-sight.

Analogously, the *luminosity distance*  $D_L(z)$  relates the flux  $f$  received by an object at redshift  $z$  with intrinsic luminosity  $L$ . We define then  $D_L(z) = \sqrt{L/4\pi f(z)}$  as

$$D_L(z) = D_M(z)(1+z). \quad (1.5)$$

This distance is used in supernova cosmology, where fluxes are used to infer dark-energy properties. Since supernovae fluxes vary by orders of magnitude, it is handy to define the *distance modulus* as the logarithm of the luminosity distance:

$$\mu(z) = 5 \log_{10} \frac{D_L(z)}{10 \text{ pc}}. \quad (1.6)$$

This definition is such that it agrees with the definition of magnitude of an object.

In all the distances defined above, the dependency to the cosmological energy densities  $\Omega_x$

happens only through  $H(z)$  (Eq. 1.1). This is how we can constrain these parameters through distance measurements. However, all cosmological distance measurements are *relative*, which means they are defined to an arbitrary normalisation<sup>2</sup>. It is only by observing the *evolution* of these relative distance measurements as a function of redshift that we can constrain cosmological parameters. Note that in all the distances defined above, the dependency with  $H_0$  only impacts this arbitrary normalisation, so it cannot be measured directly. It is useful to factor out this dependency with  $H_0$ , and write distances in units of  $h^{-1}\text{Mpc}$  (numerically equivalent to set  $H_0 = 100 \text{ km/s/Mpc}$ ). These are the units used in all works studying the large-scale structures and it is also used throughout this manuscript.

### 1.3.4 Dark-energy models

In the Eq. 1.1 for the expansion rate of the Universe, the dark-energy density term is written as a general function of redshift. As mentioned before, the simplest model is to consider a cosmological constant  $\Omega_{de}(z) = \Omega_\Lambda$ . The cosmological constant can be thought as equivalent to a fluid with relativistic pressure  $p_{de} = -\rho_{de}$ . This model can be extended by considering a different equation of state  $p_{de} = p_{de}(\rho_{de}) = w(z)\rho_{de}$ , where  $w(z)$  can be a constant or a more general function of redshift, under the condition that  $w(z) < -1/3$ , needed to obtain an accelerated expansion in a dark-energy dominated Universe. One widely known parametrisation is given by  $w(a) = w_0 + w_a(1 - a)$  (Chevallier et al. 2001; Linder 2003).

The litterature contains a huge variety of models that attempt to be more physically motivated than those just presented (see Weinberg et al. 2013, section 2.2 for a review). Some of them suggest that maybe general relativity breaks down on large enough scales, causing the expansion to accelerate. They suggest extensions or modifications to Einstein's theory of general relativity, and are commonly known as *modified gravity* models.

## 1.4 Model of the large-scale structures

The Universe is clearly not homogenous and isotropic. Matter clustered under the influence of gravity, creating the cosmic web, composed of clusters, filaments, empty regions. The model described in the previous section only describes the Universe as a whole, without any inhomogeneities. If we want to describe the evolution of the structures we need to consider an extension to the background model.

Observations of the large-scale structures and the cosmic microwave background (CMB) indicate that the matter density field today is the evolution of tiny density perturbations from the early Universe. Temperature fluctuations in the CMB are of the order of  $10^{-5}$ , while densities today can reach values several orders of magnitude larger than the average density. The most widely accepted theory is that the CMB fluctuations, and today's structures, are originated from the inflation-grown quantum fluctuations, that evolved under the influence of gravity and pressure in the hot dense plasma-like epoch of our Universe.

It is been possible to model the physics of the evolution of these tiny fluctuations using *linear perturbation theory*. The predictions of this theory are an excellent match to observations of the CMB and to the late-time distribution of matter on large scales, i.e., larger than few tens of Mpc. On smaller scales however, gravity becomes highly non-linear and more advanced calculations

---

<sup>2</sup>Two exceptions are parallax distances which are an absolute measurements based on the known distance between the Earth and the Sun and gravitational wave distances, which amplitudes depend on the distance and on the masses of the progenitors, though the masses affect the wave form as well, breaking the degeneracy.

are required. There are two main approaches to model non-linearities: theoretical calculations going beyond linear terms in perturbation theory or numerical n-body simulations. [Develop?]

The main idea of perturbation theory is to consider that the density of a given species  $x$  is given by:

$$\rho_x(\vec{x}, t) = \bar{\rho}_x(t) [1 + \delta_x(\vec{x}, t)], \quad (1.7)$$

where the bar indicates average over the whole Universe and  $\delta_x \ll 1$  is a small perturbation. The average density  $\bar{\rho}_x$  follows the background evolution described in section 1.3. A new set of equations can be derived for the evolution of  $\delta_x$  for each species depending if  $x$  denotes relativistic species (photons, hot baryons, hot neutrinos) or non-relativistic species (cold baryons, cold neutrinos or dark-matter). Only some families of models also consider fluctuations in the dark-energy density.

The evolution of  $\delta_x$  for a given species is dictated by both Boltzmann and Einstein's GR equations. Boltzmann equations describe the evolution of phase-space distributions of each constituent, considering collisions (pressure) and particle creation and annihilation. GR equations describe how each species influence gravitational potentials which in turn make perturbations grow.

Another important ingredient in these equations is the *peculiar velocities*  $\vec{v}_x(\vec{x}, t)$  of each species, particularly the non-relativistic ones since relativistic species are assumed to have  $v \sim c$ . They influence the evolution of perturbations through Boltzmann, Euler and continuity equations. These velocities are observable and are an important probe of the cosmological model and on the strength of gravity itself. They will be a key actor in Chapters 4 and 5.

### 1.4.1 Statistical description of perturbations

The value of the matter density field at a given position  $\vec{x}$  is hardly observable and therefore does not contain much cosmological information, since it is just the evolution of a single random realisation of the initial conditions. In cosmology we are mostly interested by the statistical properties of the density field, or of its perturbations. Particularly, most cosmological information is contained in the first moments of the density field, starting from the two-point function (the one-point function is zero by definition), which is defined as

$$\xi(\vec{x}, \vec{y}) = \langle \delta(\vec{x}) \delta(\vec{y}) \rangle \quad (1.8)$$

where  $\langle \cdot \rangle$  denotes an ensemble average. Given that we only have one single realisation of the Universe, we assume that averages over space (in an infinite space) are equivalent to ensemble averages.

The assumptions of homogeneity and isotropy of the background can be applied in a statistical sense to the perturbations. Statistical homogeneity makes  $\xi$  not to depend on the specific locations  $\vec{x}$  and  $\vec{y}$  but only on their separation  $\vec{r} = \vec{y} - \vec{x}$ . Statistical isotropic makes  $\xi$  no longer depend on the orientation of  $\vec{r}$ , only on its absolute value  $r = |\vec{r}|$ . Therefore, the two-point correlation function simplifies to a function of  $r$ :

$$\xi(r) = \langle \delta(\vec{x}) \delta(\vec{x} + \vec{r}) \rangle. \quad (1.9)$$

The correlation function  $\xi(r)$  is a powerful observable which can be compared to predictions from a given cosmological model.

### 1.4.2 Configuration and Fourier space

The time evolution of linear density perturbations  $\delta(\vec{x})$  is dictated by a set of second-order differential equations, containing derivatives with respect to time and space. It is thus convenient to apply Fourier transforms to these equations, where derivatives with respect to space become simple products. Separations  $\vec{r}$  in the so-called *Configuration space* become wavevectors  $\vec{k}$  in *Fourier space*. The density perturbations in Fourier space are defined by

$$\tilde{\delta}(\vec{k}) = \int d^3x e^{-i\vec{k}\cdot\vec{x}} \delta(\vec{x}), \quad (1.10)$$

and its inverse is

$$\delta(\vec{x}) = \frac{1}{(2\pi)^3} \int d^3k e^{+i\vec{k}\cdot\vec{x}} \tilde{\delta}(\vec{k}). \quad (1.11)$$

As previously, we are interested in the two (or more) point functions of the field. In Fourier space, the two-point correlation function is known as the *power spectrum* and is defined as

$$\langle \tilde{\delta}(\vec{k}) \tilde{\delta}(\vec{k}') \rangle = (2\pi)^3 P(k) \delta_{\text{Dirac}}^3(\vec{k} - \vec{k}'), \quad (1.12)$$

where  $\delta_{\text{Dirac}}^3(\vec{x})$  is a three-dimensional Dirac distribution. The assumption of spatial homogeneity is guaranteed by the properties of Fourier space, while the assumption of isotropy makes the power spectrum to be only a function of the absolute value of the wavevector  $k = |\vec{k}|$ .

When considering the evolution of perturbations in Fourier space to the linear level, each mode  $\tilde{\delta}(\vec{k})$  evolves independently of the others. We often say that there is no *mode coupling* in linear theory.

The power spectrum  $P(k)$  is an observable, as powerful as the correlation function, to constrain cosmological models. While in theory these two contain exactly the same compressed statistical information, in practice the analyses of real data use different finite ranges of scales which are affected differently by systematic effects. Therefore, analyses of real data in configuration and Fourier space complement each other. Such analyses are presented in Chapter 4.

### 1.4.3 Cosmological dependency of the power spectrum

The power spectrum  $P(k)$ , or the correlation function  $\xi(r)$ , of density perturbations are an excellent probe of the cosmological model. It encodes information accumulated of the whole Universe's history, since the Big Bang until today.

At the end of inflation, we think that perturbations were roughly Gaussian (as are quantum fluctuations of the vacuum), having a nearly scale independent power spectrum defined by

$$P_0(k) = A_s k^{n_s - 1}, \quad (1.13)$$

where  $A_s \sim 2 \times 10^{-9}$  is the amplitude of scalar perturbations and  $n_s \sim 0.96$  is the scalar spectral index. The term scalar refers to standard density (or gravitational potential) perturbations, while tensorial perturbations (of the space-time metric) refer to primordial gravitational waves. Vectorial perturbations decay and rapidly become negligible in most common cosmological models.

After inflation, the majority of the energetic budget of Universe was held by photons and neutrinos. Since their energy density decays as  $a^{-4}$ , their contribution quickly drops. This radiation-dominated era lasted until  $z \sim 5000$ , or  $t \sim 20$  kyr, when the energy density of matter

became the dominant source. Matter density decays at a slower rate, proportional to  $a^{-3}$ . Dark-energy became dominant at  $z \sim 0.5$ , or  $t \sim 9$  Gyr, since its energy density is constant (or close to constant). The actual duration of each era depends on relative values of the energy densities, parametrised by  $\Omega_x$  (see ??).

**Add figure** Matter perturbations grew at different rates during these different eras. In radiation-dominated era, large-scale modes (large values of  $r$  or small values of  $k$ ) grew while small-scale ones oscillated, due to battle between gravity and radiative pressure. These are known as *baryon acoustic oscillations*. These oscillations are imprinted in the power spectrum of the photon-baryon fluid, at the time of the CMB, and in the matter power spectrum at later times. The radiative pressure prohibited the growth of small-scale perturbations, so the matter power spectrum is damped, which results in this hill-like shape. In the matter-dominated era, the radiative pressure becomes negligible and all modes grow equally (neglecting non-linear growth). When dark-energy is dominant, the expansion accelerates and growth of structures slows down slightly.

Well after recombination, matter (baryons + dark) density perturbations obey the following differential equation, if we assume GR and linear theory:

$$\ddot{\delta}(\vec{x}, t) + 2H(z)\dot{\delta}(\vec{x}, t) - \frac{3}{2}\Omega_m H_0^2(1+z)^3\delta(\vec{x}, t) = 0. \quad (1.14)$$

If we assume that  $\delta(\vec{x}, t) = \delta(\vec{x}, t_0)G(t)/G(t_0)$ , we can factor out the spatial dependency and only solve for the time-dependent term  $G(t)$ , known as the *growth factor*. Its logarithmic derivative with respect to the scale factor  $a(t)$  is called *growth rate* of structures:

$$f(a) \equiv \frac{d \ln G(a)}{d \ln a}, \quad (1.15)$$

which is a key observable for which the predicted value depends on the cosmological parameters and on the assumed theory of gravity (e.g., GR in Eq. 1.14).

In linear theory, peculiar velocities are simply related to density perturbations via the continuity equation

$$\nabla \cdot \vec{v}(\vec{x}, a) \equiv \theta(\vec{x}, a) = -a^2 H(a) \frac{d\delta(\vec{x}, a)}{da} = -aH(a)f(a)\delta(\vec{x}, a) \quad (1.16)$$

where  $\theta$  is the velocity divergence, a convenient scalar field describing velocities. In Fourier space, the velocity field is simply proportional to the density. The velocity divergence power spectrum  $P_{\theta\theta}$  is an important ingredient for models of redshift-space distortions, as we discuss in the following section.

#### 1.4.4 The amplitude of the power spectrum

The matter power spectrum  $P(k)$  represents the variance of density perturbations at a given wavenumber  $k$ . The total variance of the density field is therefore the sum of all contributions over all available three dimensional modes. This is equivalent to the correlation function at zero separation:

$$\sigma^2 = \xi(r=0) = \frac{1}{(2\pi)^3} \int d^3 k P(k) = \frac{1}{2\pi^2} \int_0^\infty dk k^2 P(k), \quad (1.17)$$

which diverges if we use the linear prediction for the matter power spectrum. This is because the linear power spectrum is the evolution of a nearly scale invariant power spectrum, equivalent to white noise, so the variance simply keeps increasing as we consider larger ranges of scales. Therefore, it is convenient to smooth the linear density field using a three-dimensional top-hat filter with radius  $R$ . The variance of the smoothed field is then

$$\sigma_R^2 = \frac{1}{2\pi^2} \int_0^\infty dk k^2 P(k) W_R^2(k), \quad (1.18)$$

where  $W_R(k) = 3[\sin(kR) - kR \cos(kR)]/(kR)^3$  is the Fourier transform of the top-hat filter.

In studies of large-scales structures, it is common to use  $\sigma_R$  as a parameter defining the amplitude of the linear power spectrum. As discussed before, this amplitude depends on the values of  $A_s$  (Eq. 1.13) and  $h$  (which determines the age of the Universe and how long structures could have grown). Therefore  $\sigma_R$  is degenerate with  $A_s$  and  $h$  though is more representative of the amplitude of  $P(k)$  at later times. Other energy density parameters  $\Omega_x$  also affect this amplitude, but these also change the overall shape and are not degenerate with  $\sigma_R$ .

The variance  $\sigma_R$  is a decreasing function of  $R$ . Historically, the chosen values for  $R$  give variances near unity, which correspond to the regime where linear theory should break. Recently, the value of  $R = 8h^{-1}\text{Mpc}$  has been used in several analysis, though it has been argued that choosing  $R = 12 \text{ Mpc}$  (without the  $h$  dependency) is a better choice to break degeneracies (Sánchez 2020).

In measurements of redshift-space distortions and peculiar velocities, there is a degeneracy between the value of  $f$  and the amplitude of the power spectrum,  $\sigma_8$ . Therefore, measurements can only constrain the combination  $f\sigma_8$ .

## 1.5 Cosmological probes of expansion

In this section, I present the basics of the cosmological observables that allow us to learn about dark-energy. Some of these are mostly sensitive to the background evolution presented in section ??, while others depend on the matter perturbations and their statistical properties as discussed in section ??.

### 1.5.1 Direct measurements of $H_0$

The Hubble constant  $H_0$  is probably one of the first cosmological parameters to be estimated by the one giving its name (Hubble 1929). Today, there are a few techniques to estimate  $H_0$  which yield roughly independent results. See Riess 2020 for a quick review of the latest results.

The most traditional method is known as the *distance ladder*. The idea is to measure the distance-redshift relationship of objects well in the Hubble flow. The distance to the closest objects in the Solar neighbourhood can be estimated with the parallax method. The Gaia satellite has the current largest catalogue of parallax measurements, of more than a billion stars. Parallax is one of the few direct distance estimating methods. They can be used to measure the intrinsic luminosity of some objects thought to be standard candles, such as Cepheid stars, RR Lyrae, and the largest red giant stars. Distances to farther objects can be estimated using these candles. They can also be used to calibrate other brighter standard candles, such as type-Ia supernovae, which can be observed at the largest distances. Riess, Casertano, et al. 2021 contains the latest measurements using Gaia parallaxes, Cepheids and

type-Ia supernovae to determine  $H_0 = 73.0 \pm 1.4$  km/s/Mpc. Freedman et al. 2019 is latest measurement of distances using the tip of the red giant branch.

The distance to the galaxy NGC 4258 could be determined thanks to the presence of a water maser orbiting the center of this galaxy. The proper motions of several clouds orbiting close to the central massive black hole could be measured both in radial and angular directions, strongly constraining the dynamics of the system (Herrnstein et al. 1999). The most recent measurement yields  $D = 7.576 \pm 0.082$  (stat.)  $\pm 0.076$  (sys.) Mpc (M. J. Reid et al. 2019), which can be used as an alternative to Cepheids to anchor the distance ladder and provide an estimate to  $H_0$ .

Another alternative method is based on the time-delay of the signals emitted from a quasar behind a strong gravitational lens. The lens creates multiple images of the same background quasar, but the light paths have slightly different lengths. Since quasars are variable objects, the same variability is observed with a delay of several days between the different images. By modelling the distribution of matter between the quasar and us, it is possible to convert these time delays into an estimate of  $H_0$ . The “ $H_0$  Lenses in COSMOGRAIL’s Wellspring”, or H0LiCOW, collaboration produced the latest comprehensive measurement of  $H_0$  using strongly-lensed quasars (Wong et al. 2019). An alternative measurement has been performed using strong lenses from the Sloan (SLACS). They are compared to H0LiCOW in Birrer et al. 2020.

More recently, gravitational waves from a merger of two black holes were observed for the first time by the LIGO collaboration (T. L. S. Collaboration and the Virgo Collaboration 2016). Not long after, a merger of two neutron stars was observed by both LIGO and Virgo, but this time an electromagnetic counterpart was also detected (T. L. S. Collaboration and T. V. Collaboration 2017), pointing to the galaxy where the event occurred. Given the well predicted shape of the wave form and its dependency on the masses of the neutron stars, it was possible to estimate the distance to the host galaxy. Combining with a measurement of its redshift, a single event could provide an estimate of  $H_0$  (Abbott et al. 2017). This opened the field of cosmology using standard sirens, i.e., gravitational wave sources.

The cosmic microwave background can yield an estimate of  $H_0$  but it is strongly degenerate with other unknown parameters, such as curvature or dark-energy densities. Some of these degeneracies are reduced when considering the effect of gravitational lensing of the CMB or when combining with other probes of late times. Therefore, precise measurements of  $H_0$  from the CMB alone are only possible when considering more restrictive models, such as a flat space with a cosmological constant.

### 1.5.2 Type-Ia supernovae

As mentioned earlier, type-Ia supernovae (SNIa) can be used as standard candles for absolute distance measurements, if they are anchored by another method. The SNIa can also be used alone to produce relative distance measurements and constrain dark-energy. In this case, no anchor is required and the only assumption is that the SNIa intrinsic brightness does not evolve with redshift.

The main observable are the fluxes of SNIa as a function of time in different photometric bands, known as light-curves. Spectroscopic follow up observations of the explosion can confirm the type of the supernova based on the features present in their spectra. Another key ingredient is the redshift of the host galaxy of the SNIa, which is commonly measured with spectroscopy as well.

Spectro-photometric models of SNIa are used to fit the observed light-curves, yielding their apparent magnitudes at peak luminosity in a given photometric band. These models account for correlations between color and duration of light curves and the peak magnitude, reducing the intrinsic scatter in these magnitudes from 40% to roughly 15%. It is essential to obtain accurate and precise measurements of SNIa fluxes in order to obtain the best cosmological constraints. Large sets of realistic simulations of the data are required in order to correct for selection effects. The final product of the analysis is a set of distance moduli (Eq. 1.6) and their host-galaxy redshift, which can then be compared to models of expansion of the Universe.

Distance moduli depend on dark-energy through the integral of  $H^{-1}(z)$ . In order to obtain good constraints on dark-energy properties, it is important to have a large redshift coverage, at least covering the transition between matter-dominated to dark-energy-dominated eras, so  $0 < z < 1$ . The advantage of SNIa for dark-energy studies is that they can span these redshifts with a high sampling rate, which helps in the study of the expansion-rate. One of the inconveniences is that SNIa are complex and poorly understood astrophysical events, the intrinsic scatter in luminosity cannot be reduced to better than 12%, potentially limiting the gains constraining power from future experiments.

The latest comprehensive study of SNIa combines data from more than a dozen projects into a single sample, the Pantheon sample, from which dark-energy constraints were derived (D. M. Scolnic et al. 2018). The Dark Energy Survey also measured a more recent sample of few hundreds of SNe (Brout, Sako, et al. 2019; Brout, D. Scolnic, et al. 2019; Kessler et al. 2019), but not all of them have spectroscopic confirmation that they are of type Ia. Their constraints on dark-energy are not yet competitive compared to the Pantheon sample. The Zwicky Transient Facility (ZTF, Graham et al. 2019) is currently observing the Northern sky on a search for transient events and is expected to discover around 5000 spectroscopically confirmed SNIa at low redshifts ( $0 < z < 0.12$ ) until 2023. After 2023, the Rubin Observatory Legacy Survey of Space and Time (LSST) will take over in the Southern hemisphere and will discover more than 300 thousand SNIa up to  $z < 0.5$ .

While ZTF and Rubin's samples of SNIa will not decrease significantly the errors on dark-energy parameters, they cover a redshift range where other powerful probes, such as BAO or weak-lensing, lack of statistical power. Furthermore, at lower redshifts when dark-energy is dominant, SNIa are complementary to redshift-space distortions (RSD) when it comes to testing the validity of General Relativity or constraining alternate models of gravity, as solutions for dark-energy.

Not only SNIa are a great probe of the expansion history, they can also provide peculiar velocities of their host galaxies via their inferred distances. These peculiar velocities and their statistical properties can complement RSD analysis when measuring the growth-rate of structures (Eq. 1.15). Estimates of  $H(z)$  and  $f(z)$  can help break degeneracies between simple dark-energy models and more involved models of gravity (Kim et al. 2020; Graziani et al. 2020). Chapter 5 is dedicated to this topic, to which I plan to dedicate the future years of my research.

### 1.5.3 Big Bang nucleosynthesis

In the post-inflation Universe, when temperatures are below the equivalent of 100 MeV, perturbations in the matter and radiation fields are quite small and most of the physics is dictated by the interactions between protons, electrons, neutrons, and photons, as described by the Boltzmann equations. As the Universe cools down and rarefies, protons and neutrons start forming atoms of deuterium, tritium, helium and heavier elements. This process is known as the Big Bang nucleosynthesis (BBN).

The relative amount of each of the formed elements depends on the expansion rate of the Universe at that time as well as the physical density of baryons  $\omega_b = \Omega_b h^2$  and radiation  $\omega_r = \Omega_r h^2$ . Given that the energies involved are within reach of particle accelerators, these reactions can be studied with great detail on Earth, allowing us to build accurate models of the BBN (see Pitrou et al. 2021 for the latest calculations and references therein).

Observations of the primordial abundances can be compared to the predictions by BBN models. Abundances of deuterium, helium, and others can be estimated from spectroscopic observations of HII regions in metal-poor galaxies or from absorption lines of the intergalactic medium in quasar spectra. The most up-to-date measurements of the primordial helium-4 abundance yields  $Y_p = 0.2453 \pm 0.0034$  (Aver et al. 2021), while the deuterium one is  $D/H = (2.527 \pm 0.030) \times 10^{-5}$  (Pitrou et al. 2021). While observations are consistent with BBN models for deuterium and helium, the abundance of lithium-7 exhibits a factor 3 discrepancy, which is a huge problem in BBN but quite often neglected.

The temperature fluctuations in the cosmic microwave background (CMB) are also very sensitive to the physical baryon density  $\omega_b$ . Historically, the values obtained from CMB have been in good agreement with BBN measurements, showing that baryons make up to around 16% of the total matter content of the Universe, or  $\omega_b = (2.195 \pm 0.022) \times 10^{-2}$ . The agreement between two quite independent probes is one of the great successes of the current cosmological model, though they also enforce the need for a dark-matter component.

#### 1.5.4 Baryon acoustic oscillations

Baryon acoustic oscillations (BAO) is the name given to the propagation of sound waves in the primordial plasma (baryons and photons), prior to recombination. Because of the high pressure on small scales at those times, each initial density perturbation had a spherical density wave around them propagating outwards at the speed of sound in that medium. The speed of sound in the plasma is given by

$$c_s(z) \equiv \sqrt{\frac{1}{3[1 + R(z)]}} \quad (1.19)$$

where  $R(z) = 3\rho_b/4\rho_\gamma$  is the baryon-to-photon ratio. The propagation of sound waves occurred until the temperatures and densities dropped to values such that baryons no longer felt the pressure from photons, known as the *drag epoch*, which is close in time to the recombination (but technically not the same epoch). This process left a slight overdense shell around each initial perturbation with a radius given by

$$r_{\text{drag}} \equiv r_s(z_{\text{drag}}) = \int_{\infty}^{z_{\text{drag}}} dz' \frac{c_s(z')}{H(z')} \quad (1.20)$$

which is known as the *sound horizon at drag epoch*, or the BAO scale. Today,  $r_d$  has a physical size of about 147 Mpc, much larger than any collapsed structure in the Universe. As one can see from Eqs. 1.19 and 1.20,  $r_{\text{drag}}$  mainly depends on  $\omega_b$  and  $\omega_c$  assuming the CMB gives a precise estimate of  $\omega_\gamma$ . The dependency of  $r_{\text{drag}}$  is mainly through  $\omega_b$ , which is useful when constraining dark energy models for instance.

After recombination, the sound horizon scale only increases in size due to the expansion, or equivalently, its comoving size remains unchanged. Therefore, the BAO scale is a great *standard ruler* to study the expansion rate of the Universe. In practice, the BAO scale is observed statistically in the two-point function of the matter density field, so it is often classified as

an statistical standard ruler. In configuration space, the correlation function  $\xi(r)$  presents a small peak at separations corresponding to the BAO scale  $r_d$ , while in Fourier space the power spectrum  $P(k)$  contains an oscillatory pattern as a function of scale with a period proportional to the BAO scale. In Chapters 3 and 4, I present my past work in the measurement of the BAO scale using Ly $\alpha$  forests and galaxies, respectively, as tracers of the matter density field.

Given that a galaxy survey is made of angular positions and redshifts, which are true observables, the BAO peak is effectively measured as an angle  $\Delta\theta_{\text{BAO}}$  or as a difference in redshift  $\Delta z_{\text{BAO}}$ . These can be modelled as ratios of distances to the BAO scale  $r_d$  as

$$\Delta\theta_{\text{BAO}}(z_{\text{eff}}) = \frac{D_M(z_{\text{eff}})}{r_d} \quad (1.21)$$

$$\Delta z_{\text{BAO}}(z_{\text{eff}}) = \frac{D_H(z_{\text{eff}})}{r_d} \quad (1.22)$$

where  $z_{\text{eff}}$  is the effective redshift of the galaxy survey,  $D_M$  is the comoving angular diameter distance (Eq. 1.4), and  $D_H$  is the Hubble distance (Eq. 1.2).

There are two ways BAO can be used to constrain cosmological models, depending if we assume that  $r_{\text{drag}}$  is known or not. If  $r_{\text{drag}}$  is known, i.e. given by Eq. 1.20 using some value for  $\omega_b$  (given by the CMB or BBN for instance), then BAO measurements are converted to absolute distance measurements which depend only on  $H(z)$ . Therefore, BAO can constrain  $H_0$ , curvature and dark energy. If  $r_{\text{drag}}$  is supposed to be unknown but still a standard ruler, then BAO constraints the ratio of  $E(z) = H(z)/H_0$  to the combination  $H_0 r_{\text{drag}}$  which is now degenerate. This is similar to type Ia supernovae, where their absolute magnitude is degenerate with  $H_0$ . By combining several BAO measurements at different effective redshifts, BAO is a powerful probe of dark energy and curvature.

Current BAO measurements span effective redshifts from 0.1 to 2.3. The Sloan Digital Sky Survey (SDSS, Eisenstein, Weinberg, et al. 2011; Blanton, Bershadsky, et al. 2017) has measured more than 2 million redshifts spectroscopically in the past twenty years, producing the largest maps to date of the distribution of matter in the Universe. In addition to SDSS, surveys such as FastSound (Okumura et al. 2016), Vipers (Pezzotta et al. 2017), 6 degree field galaxy survey (6dFGS, Beutler et al. 2012) and WiggleZ (Parkinson et al. 2012) also produced BAO measurements using galaxies, though the volumes probed and the number of galaxies is inferior to SDSS. The latest cosmological constraints from BAO are described in Alam, Aubert, et al. 2021.

### 1.5.5 The cosmic microwave background

The cosmic microwave background (CMB) is one of the richest cosmological probes of all. The photons we receive today last scattered on baryons at a redshift of about 1100, corresponding to roughly 380 000 years after the Big Bang. It is the oldest information that we can measure from the Universe today.

The average temperature  $T_{\text{CMB}} = 2.72548 \pm 0.00057$  K (Mather et al. 1994; Fixsen 2009) of these photons, measured the last time by the COBE satellite, tell us on how much energy density from radiation there is in the Universe. From the black body Bose-Einstein distribution of photons, we have

$$\rho_\gamma = \frac{\pi^2 k^4}{15 \hbar^3 c^3} T_{\text{CMB}}^4 \quad (1.23)$$

The fluctuations around this average temperature,  $\Delta T$ , and the polarisation of these ph-

tons trace the structures back at the recombination epoch. Given its early-times nature, the temperature and polarisation fields are extremely well described by Gaussian statistics. Most of the information is therefore contained in the two point functions of these fields. Given that these fields are two dimensional, functions of the position angle in the sky ( $\theta, \phi$ ), it is convenient to decompose these fields into a basis of spherical harmonic functions  $Y_{\ell m}(\theta, \phi)$ , which amplitudes are denoted  $a_{\ell m}$ . The angular power spectrum is simply the variance of these amplitudes:  $C_{\ell} = \langle a_{\ell m} a_{\ell m}^* \rangle$ , which in linear theory is simply a function of  $\ell$  and independent of  $m$ . The temperature and both polarisation modes (E and B) can be decomposed into spherical harmonics, so we can estimate all cross power spectra, e.g.,  $C_{\ell}^{TE} = \langle a_{\ell m}^T a_{\ell m}^{E*} \rangle$  is the cross temperature and E-mode polarisation power spectrum.

The temperature and polarisation auto and cross power spectra are exquisitely well modelled by linear perturbation theory. In the most basic  $\Lambda$ CDM model, the power spectrum is a function of only six parameters: the angular scale of baryon acoustic oscillations  $\theta_*$ , the physical density of baryons  $\omega_b$  and dark-matter  $\omega_c$ , the primordial power spectrum amplitude  $A_s$  and slope  $n_s$ , and the optical depth  $\tau$ . The fact that such a model with so few free parameters can describe so well the observations is one of the greatest achievements in modern physics. A great description of the CMB physics from first principles can be found in Dodelson et al. 2020. Several codes are available to compute models for the CMB such as CAMB<sup>3</sup> (Lewis et al. 2000) and CLASS<sup>4</sup> (Lesgourgues 2011).

Explain how the power spectrum depends on the parameters

Latest measurements: Planck satellite (Planck Collaboration et al. 2020), Atacama Cosmology Telescope (ACT, Aiola et al. 2020), South Pole Telescope (SPT, Aylor et al. 2017; Balkenhol et al. 2021; Dutcher et al. 2021), BICEP/Keck (BICEP/Keck et al. 2021) for B-modes.

### 1.5.6 Redshift-space distortions

Matter is not static in the Universe. Due to gravity, matter flows from underdense regions towards overdense ones. These velocities are commonly called *peculiar velocities*. The radial component of peculiar velocities alters the observed redshift of an object, due to the Doppler effect. Therefore, the total observed redshift  $z_{\text{obs}}$  is a combination of its cosmological redshift  $z_{\text{cos}}$ , due to the expansion of the Universe, and the peculiar redshift  $z_{\text{pec}}$ , due to the Doppler effect:

$$1 + z_{\text{obs}} = (1 + z_{\text{cos}})(1 + z_{\text{pec}}) \quad (1.24)$$

where

$$z_{\text{pec}} = \sqrt{\frac{1 + \frac{\vec{v} \cdot \hat{n}}{c}}{1 - \frac{\vec{v} \cdot \hat{n}}{c}}} - 1 \approx \frac{\vec{v} \cdot \hat{n}}{c} \quad (1.25)$$

The first equality is the definition of the relativistic Doppler effect,  $\vec{v}$  is the velocity and  $\hat{n}$  is the radial unitary vector. The right-hand side is the non-relativistic approximation, which is accurate for typical velocities of matter flows in our Universe.

When converting observed redshifts into comoving distances, peculiar velocities introduce a small error such that

$$s(z_{\text{obs}}) \approx r(z_{\text{cos}}) + \frac{(1 + z_{\text{cos}})}{H(z_{\text{cos}})} \vec{v} \cdot \hat{n}, \quad (1.26)$$

where  $s$  is the *redshift-space* distance and  $r$  is the *real-space* distance. The errors caused by

---

<sup>3</sup><https://camb.info/>

<sup>4</sup>[https://lesgourg.github.io/class\\_public/class.html](https://lesgourg.github.io/class_public/class.html)

peculiar velocities distort the observed distribution of matter/galaxies since we cannot in general decouple the velocities and the Hubble flow. This effect is observable and named *redshift-space distortions* (RSD). RSD are a powerful probe of the dynamics of the matter field, i.e., on how velocities are related to the densities, and how they contribute to the growth of structures over time. More generally, observations of RSD can be used to test the validity of general relativity since it is a probe of the strength of gravity.

The density contrast of matter is modified when observed in redshift-space relative to real-space, given the redshift-space distortions. Mass conservation implies that

$$[1 + \delta_s(\vec{s})] d^3 s = [1 + \delta(\vec{x})] d^3 x, \quad (1.27)$$

such that in Fourier space we obtain, in the linear regime (Kaiser 1987)

$$\delta_s(\vec{k}) = (1 + f\mu^2)\delta(\vec{k}) \quad (1.28)$$

where  $f$  is the growth-rate of structures defined in Eq. 1.15 and  $\mu = \vec{k} \cdot \hat{n}/k$  or the cosine of the angle between the wavevector and the line of sight. The power spectrum in redshift-space assuming linear perturbations is simply

$$P_s(k, \mu) = (1 + f\mu^2)^2 P_m^{\text{lin}}(k) \quad (1.29)$$

This means that the redshift-space matter power spectrum has radial modes enhanced by a factor of  $(1 + f)^2$  (where  $f \sim 1$ ) relative to modes transverse to the line of sight. This enhancement is observable with galaxy surveys. If the normalisation of the linear matter power spectrum is parametrised by  $\sigma_8$  (Eq. 1.18), then the actual measured quantity is the product  $f\sigma_8$ . Transposed to a given effective redshift  $z_{\text{eff}}$  of a galaxy survey, we need to scale  $\sigma_8$ , which is usually defined at  $z = 0$ , using the growth factor  $D(z)$ , such that the measured quantity is  $f(z)\sigma_8 D(z)$ .

The observable  $f(z)\sigma_8 D(z)$  is mostly sensitive to the amount of dark matter  $\omega_m$ , which drives the growth of structures, and  $H(z)$ , which damps the growth (see Eq. 1.14). Therefore, it can be used to constrain dark energy models. More generally, measurements of  $f(z)\sigma_8 D(z)$  can be used to test the the validity of general relativity on large scales, which is the commonly assumed theory of gravity.

The latest most relevant measurements were performed using data from the Sloan Digital Sky Survey (SDSS), including

- the SDSS Main Galaxy Sample Cullum Howlett et al. 2015,
- the Baryon Oscillation Spectroscopic Survey (BOSS, Alam, Ata, et al. 2017),
- the extended BOSS luminous red galaxy sample (eBOSS LRG, Julian E Bautista et al. 2020; Gil-Marín et al. 2020),
- the eBOSS emission line galaxy sample (eBOSS ELG, Tamone et al. 2020; de Mattia, Ruhlmann-Kleider, et al. 2021),
- the eBOSS quasar sample (eBOSS QSO, Hou et al. 2021; Neveux et al. 2020),

In chapter 4 I present my contributions to the measurement of the growth-rate of structures using the eBOSS LRG sample (Julian E Bautista et al. 2020). The cosmological implications of SDSS growth-rate measurements are described in Alam, Aubert, et al. 2021.

### 1.5.7 Weak gravitational lensing

Photons follow space-time geodesics. Space-time is distorted in the presence of a source of gravitational potential, which is typically in the form of a mass concentration. Therefore, the matter distribution in the Universe bends photon trajectories from distant sources. This phenomenon receives the name of *gravitational lensing*, since the theory describing light propagation on a gravitational field is analogous to classical optics. Gravitational lensing is a rich cosmological probe since the distortion of photon trajectories depends on both the baryonic and dark matter. From lensing measurements we can learn about the total matter distribution in an expanding Universe.

In the case of an extended source of photons, e.g., a galaxy, light from different angular positions within the source take slightly different paths towards the observer. If this extended source is placed in the background of a mass concentration - the lens - each path will suffer a slightly different bending, which depends on the impact parameter of each photon relative to the center of this lens. Also, due to conservation of surface brightness (is this the correct name?), the total flux is also increased. The final result is an image shifted, distorted and brighter.

Lensing measurements use shifts, distortions and increase in flux to determine properties of the lenses. These measurements are hard since we do not have access to the original unlensed position, shape and flux of a given galaxy. One remarkable exception is lensing in its strong regime. When the ratio between impact parameter of the source and mass of the lens is below some threshold - the Einstein radius - multiple images of the same source are created. Strong lensing allows us to estimate the mass and density profile of a given lens. Moreover, if the source is variable in time, this variability is slightly delayed between each of the multiple images, which allows us to constrain the expansion of the Universe. As mentioned in section 1.5.1, strongly lensed quasars (variable sources) are used to constrain  $H_0$ , under the assumption that we can properly model the lens density profile.

However, statistical measurements of lensing, such as correlations with overdensities, can be performed by making assumptions on the statistical properties of the unlensed sample of galaxies.

weak regime we measure shapes and correlate themselves (shear-shear) or with the galaxy field (galaxy-shear)

Sensitive to: the amplitude of the shear power spectrum,  $S_8 = \sigma_8 \sqrt{\Omega_m / 0.3}$ .

Latest measurements: Kilo Degree Survey (KiDS, Heymans et al. 2021), Dark Energy Survey Year 3 (DES-Y3, D. Collaboration et al. 2021), Hyper Supreme Cam first year (HSC, Hikage et al. 2019)

# 2 Observing the Universe with spectroscopy

## Contents

2.1 Selecting the objects to observe . . . . .	24
2.2 Pointing fibres to the sky . . . . .	25
2.3 From electrons to spectra . . . . .	26
2.4 From spectra to redshifts . . . . .	28
2.5 From redshifts to cosmology . . . . .	28

In the last two decades, spectroscopy became one of the most powerful techniques to survey the galaxies of our Universe. Particularly thanks to its capability to obtain precise galaxy redshifts, spectroscopy allows us to build precise maps of the distribution of matter in three dimensions.

This chapter is an overview on how to observe galaxies with spectroscopy and how the data is treated from the target selection all the way to the redshifts. I expose my work on improving the spectroscopic data reduction pipeline for the extended Baryon Oscillation Spectroscopic Survey (eBOSS), for which I was the *Lead Data Scientist* for 3 years.

Naturally, this chapter will focus on the spectroscopic observations with the Sloan Digital Sky Survey (SDSS), but the majority of the concepts introduced here also apply to the Dark Energy Spectroscopic Instrument (DESI).

## 2.1 Selecting the objects to observe

The first step to build a spectroscopic survey is to pre-select objects to be observed. This step, known as *target selection*, is required since you need to know where to point the optical fibers that take the light from an object to the spectrograph. Therefore, we cannot simply observe all objects in a given field, we need to choose which targets to observe.

For the target selection, a prior *photometric or imaging* survey is required. In the first years of SDSS, a photometric survey was carried out, covering more than XXX deg<sup>2</sup> of the sky York et al. 2000. The focal plane was equipped with six rows of five charge-coupled devices (CCD), each one covered with one of the SDSS filters: *u, g, r, i or z*. J. E. Gunn et al. 1998; Doi et al. 2010. A technique named drift-scanning was used to continuously observe “stripes” of constant declination during the night. SDSS was the first of its kind to produce a systematic survey of the Universe in the optical domain.

Images were reduced using the SDSS photometric pipeline Lupton et al. 2001; Padmanabhan, Schlegel, et al. 2008. Fluxes/magnitudes and their uncertainties were computed for each detected object in five colour bands. Based on their fluxes and angular sizes relative to the point-spread function (PSF), each object received a photometric classification as star or galaxy.

The final list of objects with their respective fluxes and angular positions is the input for targeting algorithms. These algorithms aim to select a given type of object for spectroscopic follow-up, based solely on their fluxes and colors. For galaxy surveys, it is vital to be able to

Table 2.1: Surveys and their target selection algorithms

Sample	Redshift range	Reference
SDSS Main Galaxy Sample	$0.0 < z < 0.2$	Strauss et al. 2002
BOSS LOWZ galaxies	$0.2 < z < 0.4$	B. Reid et al. 2016
BOSS CMASS galaxies	$0.4 < z < 0.7$	B. Reid et al. 2016
BOSS Ly $\alpha$ forest quasars	$2.0 < z < 3.5$	N. P. Ross et al. 2012
eBOSS LRGs	$0.6 < z < 1.0$	Prakash et al. 2016
eBOSS ELGs	$0.7 < z < 1.1$	A. Raichoor et al. 2017
eBOSS quasars as tracers	$0.8 < z < 2.2$	Myers et al. 2015
eBOSS Ly $\alpha$ quasars	$2.0 < z < 3.5$	Myers et al. 2015 N. Palanque-Delabrouille et al. 2016

distinguish between galaxies - the objects of our interest - and stars - which belong to our own galaxy and have a distinct scientific purpose. Additional colour cuts also help selecting a given redshift range for particular types of galaxies.

Since we are interested in the clustering of galaxies, it is essential to obtain a relatively homogeneous angular density of targets so to avoid spurious correlations. Target selection algorithms enforce a requirement of about 15 per cent angular fluctuations on the number density of targets. Residual fluctuations have to be corrected before any clustering measurements, I will discuss about this in section 2.5.

Table 2.1 provides a summary of target selection algorithms for several types of galaxy types and redshift ranges. (see [https://www.sdss.org/science/technical\\_publications](https://www.sdss.org/science/technical_publications))

## 2.2 Pointing fibres to the sky

Once the targets are chosen, we need to define the observing strategy for spectroscopy. This strategy is defined based on several constraints, such as

- the focal plane dimensions, which is a one meter diameter plate holding 1000 optical fibers;
- the field of view of the telescope, which is about  $5 \text{ deg}^2$  for the plates;
- the number of fibers. There are a total of 1000 fibers available of which 80 are used for sky observations and 20 for standard stars;
- the size of the footprint, which is roughly  $10\,000 \text{ deg}^2$ ;
- the fiber completeness, i.e., the fraction of targets receiving an optical fiber. The completeness has to be usually above a certain threshold over all the footprint;
- exposure times and total observing time available. Exposure times are dependent on the average signal-to-noise ratio of the observed targets, which should reach a certain threshold. The total observing time of the program is roughly four to five years.
- visibility window of a given patch of the sky at a given time of the year;
- priority for fiber assignment. Some types of targets have higher priority than others, which affects the fiber completeness of the low-priority samples.

The process of dividing the sky into overlapping projections of the focal plane is called *tiling*. A detailed description of the tiling algorithm can be found in Blanton, Lin, et al. 2003. Once the tiling and fiber assignment are set, this information is sent to the plate production and drilling of holes that will hold the optical fibers. Focal plane plates are drilled a few months before observing and are unique for a particular patch of the sky and observing time. Not observing the plate at the designed times causes loss of flux due to different refraction caused by the atmosphere.

The drilled plates are sent to the Apache Point Observatory (APO) in New Mexico where the Sloan 2.5-meter Telescope is based. On the mountain, observers attach the plates into cartridges that will fit at the focal plane of the telescope. There are about 15 cartridges, each equipped with 1000 optical fibers. The fibers are plugged by hand, by one or two observers during the afternoon preceding the observation night. Plates are unplugged from their cartridge once a large enough number of exposures has been taken. A minimum of 3 exposures are taken per plate.

The light of the objects is transported by the optical fibers through the Sloan spectrographs. There are two spectrographs attached at the focal plane of the telescope. Each spectrograph receives the light from 500 fibers and passes it through a beamsplitter, dividing it into a red and blue channels. Each channel has its own grism that spreads the light over wavelength before hitting the CCDs. The blue camera observes roughly from 3500 to 6000 Å and the red camera from 6000 to 10500 Å. The resolution  $R \equiv \lambda/\Delta\lambda$  increases with wavelength from 1500 to 2000 on the blue camera and from 2000 to 2500 on the red camera.

In addition to the science exposures (observing galaxies), a small set of calibration exposures is also taken, typically at the beginning and at the end of the observing run. Flat exposures are taken with lamps that emit over all wavelengths. The light is passed through the spectrographs, so we refer to these as fiber-flats, as opposed to the exposures taken without the spectrographs, named super-flats. With another type of lamp, which emit narrow lines at some specific wavelengths, arc exposures are obtained, that are used to derive the wavelength-pixel relation.

## 2.3 From electrons to spectra

This section describes the data reduction pipeline of spectroscopic observations by the SDSS telescope, for which I contributed as the eBOSS Lead Data Scientist. This automated pipeline transforms the counts stored in CCDs into calibrated spectra, for which redshifts are estimated. The software, named `idlspc2d`, was written in Interactive Data Language (IDL) and can be found online<sup>1</sup>. The latest version used in Data Release 16 of eBOSS data is v5\_13\_0 (Ahumada et al. 2020).

The dispersed light of each object falls onto CCD detectors containing 2048x2048 square 24 $\mu$ m pixels. There are 500 traces per CCD, except when fibers are broken or unplugged by accident. The traces of each spectra are parallel and slightly curved towards the edges. They are separated by about 7 pixels.

The first step of the data reduction is to remove bias and dark, mask cosmic rays and other known bad pixels, convert counts into electrons using estimated gain values, and correct for the super-flat image (flat taken without the spectrograph).

The next step is to extract the total number of counts per wavelength and per object. One of the axis of the CCD is aligned with the wavelengths, but we do not know the wavelength

---

<sup>1</sup>[https://svn.sdss.org/public/repo/eboss/idlspc2d/tags/v5\\_13\\_0/](https://svn.sdss.org/public/repo/eboss/idlspc2d/tags/v5_13_0/)

solution at this point. The other axis is aligned with fiber number. The extraction of the fluxes is performed by bundles of 20 fibers. A set of 20 Gaussian profiles plus a third order polynomial term are fit simultaneously over the counts. From the best-fit parameters of the Gaussian, one can compute the total flux at each wavelength for each object. This fit is performed regardless of whether the fibers contain flux from sky, stars or galaxies. The extraction is performed similarly to science, flat and arc exposures.

One important aspect of extraction is: what do we use as weights in the fit? For SDSS-II and III, the extraction used the total estimated variance of each pixel, assumed to be Poisson with mean equal to the number of observed hits in the pixel. However, in SDSS-IV eBOSS we pushed the limits of the instrument by observing fainter objects. In this regime, we started to observe biases due to this weighting scheme in the extraction. The ideal extraction would use the true variance (Horne 1986), not the estimated one, as a weight. Using the estimated one yields a bias in the final fluxes. We modified the extraction algorithm such that it would use a flux-independent weight for fit, yielding unbiased fluxes. The price to pay is that this extraction is less optimal, yielding slightly larger flux uncertainties. Biased fluxes affected particularly the analysis of Ly $\alpha$  forests, as described in Chapter 3 or in the appendix of Julian E. Bautista, Nicolás G. Busca, et al. 2017.

The fiber-flat images are used to calculate the traces positions and widths (more precisely than in science images) and to correct for throughput variations across fibers. The arc images are used to calculate the wavelength solution and the dispersion in the wavelength direction based on the line widths. Sky lines in science exposures are eventually used to do small adjustments to the arc-image solution.

The flux in the sky fibers are used to fit a sky model in units of counts. A polynomial dependency over fiber index is used to account to variations over the focal plane. This sky model is then subtracted from all science spectra, including the sky spectra themselves and calibration stars. The sky-subtracted sky fibers are a good metric to evaluate the quality of sky subtraction algorithm.

The next step of the reduction is the *flux calibration*, which converts the observed counts into flux in physical units. The spectra of standard stars are the main ingredient of the flux calibration. The stars chosen for calibration are of type F, with small variations in temperature and metallicity. Physical models of their spectral emission can be obtained through complex stellar synthesis calculations, including all absorption features. The goal is to fit absorption lines to the data in order to determine the exact model for each observed star. We start by isolating the absorption lines in the observed spectrum (in units of counts) by fitting a smooth function over its shape, then dividing the whole spectrum by this model. The same is done for the physical stellar models, so the fit only uses the absorption lines information. Once the best parameters of the star are found, a calibration vector is constructed by simply taking the ratio of the observed counts to the full model including its smooth shape. A set of ten stars are fit independently and a single calibration vector is obtained from them. This final calibration vector is then applied to all other galaxy spectra in order to convert their flux into physical units. During the last years of eBOSS, I updated the set of physical stellar models from the Kurucz model to those used in DESI (ref? Allende-Prieto?) which have a larger diversity in stellar parameters and more precise absorption features. This update contributed to a significant reduction of flux calibration residuals (add Figure??) computed using stacks of spectral regions of quasars without emission or absorption lines.

Once individual science exposures are converted into physical flux units, we proceed to the coaddition of these exposures into a single set of spectra. For a given object, a B-spline

is fitted over all observed spectra, using a new wavelength grid with constant steps in  $\log_{10} \lambda$  of  $10^{-4}$ . The best-fit spline is the final coadded spectrum for this object. The coaddition is made independently for each object. At this stage, we also combine spectra from blue and red cameras into one single spectrum covering the full wavelength range of 3500 to 10500 Å. The last step of this process is the calculation of potential broadband distortions in flux caused by atmospheric differential refraction (ADR). Using information from the plate design, the position of the fibers in the plate and the actual observations (airmass, hour-angle), one can compute a correction vector that is also applied to all spectra.

During the whole reduction, pixels or whole fibers can be masked due to any issues, or when the robustness of flux calculations is compromised. Each pixel has a flux and an uncertainty estimates, the latter is expressed as an inverse variance, which can be used directly as a weight in scientific analyses.

This concludes the so-called two-dimensional reductions, that convert 2D CCD images into a set of calibrated coadded sky-subtracted 1D spectra.

## 2.4 From spectra to redshifts

The next and last step of the automated data reduction pipeline is the spectral classification and redshift measurement. A set of physical templates of stars, galaxies and quasars is fit to each spectrum by a simple  $\chi^2$  minimization. For each template, we scan over several values of redshifts to obtain the minimum  $\chi^2$ . The redshift ranges probed depend on the type of template: stars are at  $z = 0$  with allowed peculiar velocities, galaxies are in  $0 < z < 2$  and quasars in  $0 < z < 7$ . The five pairs of template-redshift producing the smaller  $\chi^2$  values are stored. Redshift uncertainties are estimated using the  $\chi^2$  profiles around the minima. If the difference between the first and second best-fit  $\chi^2$  values is smaller than a certain threshold (corresponding to roughly  $5\sigma$  for one parameter), a warning flag is set, meaning that the classification is not to be trusted.

A program of visual inspection of reduced spectra, with their automated classification and redshift estimates, is carried out following the first observations of a new survey. Visual inspection is a important step in order to verify the quality of the data reduction and the classification process. A truth table containing the visually confirmed redshifts and classifications for thousands of spectra is one of the results of the visual inspection. This truth table is used to compute the actual density of tracers that are obtained for a given target selection, as a function of redshift. Spectral features caused by problems in the reduction were then reported to the pipeline team.

During the first months of eBOSS, I coordinated a program of visual inspection where about 15 members analysed about a thousand spectra each (with some overlap for cross-checking results). This provided a truth table for the Luminous Red Galaxies from eBOSS. Similar programs were carried out for the eBOSS Emission Line Galaxies and quasars. The inspections of eBOSS quasars continued through the whole program, where a small fraction of the spectra without confident automated classifications were inspected. In DESI, a larger visual inspection program was put in place for the same goals.

## 2.5 From redshifts to cosmology

Description of catalog generation. Shall this go on the clustering part ?

# 3 The high-redshift Universe and its forests

## Contents

3.1	Forests as a tracer of the Universe's structures	29
3.2	Baryon acoustic oscillations in the forests	31
3.2.1	Transmission field	32
3.2.2	Two-point correlation functions	33
3.2.3	Correction matrices	34
3.2.4	The model	35
3.2.5	BAO constraints	36
3.3	Impact of redshift errors	38
3.4	Weak-lensing of forests	41
3.5	Voids in tomographic maps	44

Until today, the Ly $\alpha$  forest in quasar spectra has been the only tracer of large-scale structures producing measurements of baryon acoustic oscillations (BAO) at redshifts above 2. Given the higher redshifts and the smaller scales probed, the clustering of the forest also yielded competitive constraints on the sum of the mass of the neutrino species, when combining it with measurements of the cosmic microwave background (CMB) anisotropies. Current and future spectroscopic surveys plan to observe denser samples of Ly $\alpha$  forests to improve our understanding of the  $z > 2$  Universe.

In this chapter, I expose my contributions to the study of dark energy through Ly $\alpha$  forest observations. Section 3.1 introduce the main concepts used in this chapter. Section 3.2 focus on the BAO measurements from BOSS and eBOSS surveys for which I provided key contributions. My thesis<sup>1</sup> was dedicated to this topic. Section 3.3 and 3.4 present two projects carried out by my former PhD student Samantha Youles at the University of Portsmouth, UK, who graduated on the 18th of March 2022.

## 3.1 Forests as a tracer of the Universe's structures

The Ly $\alpha$  forest is the name for a series of absorption lines observed in quasar spectra caused by the presence of neutral hydrogen along the line of sight between us and the quasars. Figure XX shows an example of a optical quasar spectrum with its Ly $\alpha$  forest. These lines are seen bluewards of the Ly $\alpha$  emission peak of the quasar, which lies at the quasar rest-frame wavelength  $\lambda_{\text{rest}} = 1216 \text{ \AA}$ . The absorption is not limited to the first transition; bluewards of the Ly $\beta$  peak ( $\lambda_{\text{rest}} = 1025 \text{ \AA}$ ) we also observe Ly $\beta$  absorption lines on top of the Ly $\alpha$  ones, and similarly for all Lyman series until the Lyman break at  $912 \text{ \AA}$ .

The advantage of the forests is that it provides a tomographic view of the matter distribution along the line of sight of the quasar. This is because, as the light propagates outwards of the quasar, the Universe expands, causing the whole spectrum to be redshifted. When the

<sup>1</sup><https://tel.archives-ouvertes.fr/tel-01389967>

redshifted spectrum hits a hydrogen atom, the light being absorbed at the Ly $\alpha$  transition in the *atom* rest-frame is no longer at the Ly $\alpha$  wavelength in the *quasar* rest-frame: it is a bluer wavelength. If a given quasar sits at a redshift  $z_q$  and a given intervening atom sits at a redshift  $z_a < z_q$ , the Ly $\alpha$  photon being absorbed by the atom corresponds to a photon at  $\lambda_{\text{rest}} = 1216(1+z_a)/(1+z_q)$  Å in the quasar rest-frame. In our frame, the observed wavelength of the atom absorption, or equivalently of its Ly $\alpha$  line, is  $\lambda_{\text{obs}} = 1216(1+z_a)$  Å. Note the observed wavelength does not depend on the quasar redshift. We only need the quasar redshift to identify where the Ly $\alpha$  forest is in the observed spectrum, such that we can assign each observed wavelength to a quasar rest-frame wavelength. The result is that a single forest of lines maps the neutral hydrogen density across a large range in redshifts. One single quasar spectrum can yield a map of the large-scale distribution of matter along its line of sight over up to several hundreds of megaparsecs (Mpc).

How much neutral hydrogen is needed to create a forest of Ly $\alpha$  absorption lines? Not a lot as it turns out. Given the high cross-section of the Ly $\alpha$  resonance, very low densities of neutral hydrogen are sufficient to create a line. At redshifts  $2 < z < 4$  where Ly $\alpha$  forests are observed in the optical, typical densities found in the intergalactic medium (IGM),  $n_{\text{HI}} \sim 10^{XXX}$  cm $^{-3}$ , are enough to absorb a significant fraction of the photons. Denser regions completely absorb the light and create saturated lines (zero flux). This is the case of the so-called *high-column density systems* (HCDs), which are often associated with galaxies or proto-galaxies. The extreme cases can be observed with high-resolution spectroscopy, where we can also observe a non-saturated deuterium absorption from which we derive constraints on big-bang nucleosynthesis (BBN, see section 1.5.3).

The Ly $\alpha$  forest, and therefore the amounts of neutral hydrogen in the IGM, is tightly connected with the process of reionisation of the Universe. As more stars and quasars form, more ultraviolet light is produced, progressively ionising the neutral hydrogen. On top of that, the Universe continuously expands, diluting it. Thus, the average absorption of forests decreases with time, or increases with redshift. At redshifts above 6, most of the light bluewards of the Ly $\alpha$  emission is absorbed, while at redshifts below 1, the Ly $\alpha$  absorption is minimal. Forests from  $z_q > 6$  quasars are used to put constraints on reionisation (ref?).

The Ly $\alpha$  forest and its connection with the large-scale structures have been studied theoretically since works by James E. Gunn et al. 1965. Most of recent advances are thanks to numerical simulations. In order to simulate forests, a full hydrodynamic n-body simulations are required, including all the complex baryonic physics. Add more refs. On large scales, it has been shown that the forest can be considered as linear tracer of the underlying matter field McDonald, Miralda-Escudé, et al. 2000; McDonald 2003; McDonald, Seljak, Cen, et al. 2005. On smaller scales, the gas physics is more complex to model given the effects of pressure and thermal velocities. Feedback from supernovae explosions, AGN or star forming galaxies also play an important role to model the small-scale clustering (Chabanier et al. 2020). The small scales are interesting due to their potential to constrain neutrino masses for instance.

The first measurements of clustering using the Ly $\alpha$  forests were based solely on the two-point statistics along the same line of sight (Croft, Weinberg, et al. 1999; McDonald, Seljak, Burles, et al. 2006). Given the good wavelength sampling of a forest, limited by the resolution of our spectrographs, the small scales are easily accessible in the radial/wavelength direction. This type of measurement is still performed today and allow us to obtain tight upper limits on the total mass of neutrino species (Nathalie Palanque-Delabrouille et al. 2020), when combined with measurements of the cosmic microwave background.

It is only with the Baryon Oscillation Spectroscopic Survey (BOSS) from SDSS-III that we

could study the clustering of Ly $\alpha$  forests in three dimensions. Thanks to the density of quasars observed by BOSS, of about  $15 \text{ deg}^{-2}$ , it was possible for the first time to estimate correlations using absorption from neighboring lines of sight. Also thanks to the large area of sky covered by BOSS, the first measurement of baryon acoustic oscillations (BAO) using forests was achieved N. G. Busca et al. 2013; Slosar, Iršič, et al. 2013; Kirkby et al. 2013.

Quasars also trace the matter field. While their density is not homogenous enough across the sky to measure clustering using these quasars alone, they can be cross-correlated with the forests. The cross-correlation between quasars and Ly $\alpha$  forests is interesting because it is mostly independent of the Ly $\alpha$  forest auto-correlation. This is mainly because the quasar sample has a low density (shot-noise dominated). The first measurement of BAO in the quasar-forest cross-correlation was also possible with BOSS (Font-Ribera, Kirkby, et al. 2014). The BAO constraints from the auto and cross correlations could be combined assuming that these two are independent.

Since the first measurements of BAO using forests, the BOSS and eBOSS collaborations published BAO constraints with increasingly larger samples and improved analysis. They are associated with the official SDSS Data Releases (DR):

- DR9: First measurement of large-scale Ly $\alpha$  correlations without BAO (Slosar, Font-Ribera, et al. 2011);
- DR9: First detection of BAO in the Ly $\alpha$  auto-correlation (N. G. Busca et al. 2013; Slosar, Iršič, et al. 2013; Kirkby et al. 2013);
- DR11: First detection of BAO in the quasar- Ly $\alpha$  cross-correlation (Font-Ribera, Kirkby, et al. 2014), updated auto-correlation measurement (Delubac et al. 2015);
- DR12: Final BOSS auto-correlation (Julian E. Bautista, Nicolás G. Busca, et al. 2017) and cross-correlation measurements (du Mas des Bourboux, Le Goff, et al. 2017);
- DR14: Updated measurements with eBOSS data (de Sainte Agathe et al. 2019; Blomqvist, du Mas des Bourboux, et al. 2019);
- DR16: Final Ly $\alpha$  BAO measurements of SDSS (du Mas des Bourboux, Rich, et al. 2020).

### 3.2 Baryon acoustic oscillations in the forests

In this section I detail the methodology I used in my past work to measure BAO with a set of Ly $\alpha$  forests, highlighting my personal contributions. I consider the case of SDSS forests, which are observed in the optical domain with low-resolution spectroscopy. Forest have a rather low signal-to-noise ratio on average, so the methods are fit to this type of data. Similar methods are employed in the measurement of the line-of-sight (or one-dimensionnal) power-spectrum, but we focus on BAO here.

The main steps of the BAO analysis with Ly $\alpha$  forests are:

- estimate of the transmission field and their associated weights;
- estimate of the two-point correlation functions, including the cross-correlation with quasars;
- estimate of correction matrices due to distortions of continuum fitting and metals;
- fit of the BAO model over measured correlations.

### 3.2.1 Transmission field

As described in section 3.1, the amount of absorbed flux at a given wavelength (redshift) is related to the density of neutral hydrogen and therefore is a tracer of structures.

The main observable used to compute correlations is the so-called *transmission*  $F$ , defined as

$$F(\hat{n}, \lambda) = f(\hat{n}, \lambda) / C(\hat{n}, \lambda) = \exp\{-\tau(\hat{n}, \lambda)\} \quad (3.1)$$

where  $f(\hat{n}, \lambda)$  is the observed flux and  $C(\hat{n}, \lambda)$  is the unabsorbed/original flux level, for a quasar line-of-sight at angular position  $\hat{n}$  and observer-frame wavelength  $\lambda$ , which can be linked to the absorber redshift  $z = \lambda/\lambda_\alpha - 1$  if the absorption is due to Ly $\alpha$ . We can also express the transmission as a function of the optical depth  $\tau$  as in the right-hand side of Eq. 3.1.

The challenge is to estimate transmissions from the observed fluxes of a set of quasar spectra, particularly given that our data is low-resolution and relatively noisy. This makes it hard to “see” the unabsorbed flux level  $C$ , also known as the *continuum* level, requiring automated methods. Several past attempts to achieve this used either principal-component analysis techniques (Lee et al. 2012) where the templates were built from high-resolution and high signal-to-noise data; or maximum likelihood methods accounting for the non-Gaussian nature of the probability density function of  $F$  (N. G. Busca et al. 2013). During my PhD, I particularly tried to merge these last two methods into a single one, without success. Those methods, while more sophisticated and flexible in their modelling of  $C$ , they suffer from the additional noise added to the estimated transmission due to noisier estimates of  $C$ . The simplest method will prevail in the latest analyses, which consists in averaging forests in their rest-frame to obtain a single average shape for  $C$ , or *mean continuum*  $\bar{C}$ . This shape is then fitted to each individual forest with a linear tilt in  $\log \lambda$ , i.e.,  $C(\hat{n}, \lambda) \equiv \bar{C}(\lambda)[a_0(\hat{n}) + a_1(\hat{n}) \log \lambda]$ , where  $a_0$  and  $a_1$  are fitted coefficients per quasar.

Once the continuum level  $C$  is estimated for each forest, one can compute the transmission  $F$  and their *fluctuations*  $\delta_F$  around the mean, defined as

$$\delta_F(\hat{n}, \lambda) = \frac{F(\hat{n}, \lambda)}{\langle F \rangle} - 1 \quad (3.2)$$

where  $\langle F \rangle$  is the ensemble-averaged transmission of the Universe.

The  $\langle F \rangle$  is actually an evolving function of time (or redshift or observed-frame wavelength) and it is important to take this evolution into account when computing  $\delta_F$ . Several measurements of this quantity exist (Faucher-Giguère et al. 2008; Pâris et al. 2011; Becker et al. 2013; Kamble et al. 2020), though the latest BAO measurements do not use them directly to compute  $\delta_F$ . One could in principle use the forests themselves to estimate  $\langle F \rangle$ , by stacking forests in their observer-frame (by contrast with the mean continuum that is a stack in the quasar rest-frame), though this requires a good estimate of  $C$ . If one express  $\delta_F$  as a function of the observed flux  $f$ , the continuum  $C$  and the average transmission  $\langle F \rangle$ , one sees that there are degeneracies. The latest BAO analyses therefore fits a linear function that models the product  $C\langle F \rangle$  simultaneously.

All methods to estimate the transmission fluctuations also suffer from the fact that they use information the forests themselves to estimate  $C$  or  $C\langle F \rangle$ . This creates spurious correlations between a given pixel in a given forest and a neighboring pixel in the same forest. As I will discuss in section 3.2.3, spurious correlations are also introduced between pixels in different lines-of-sight, distorting the correlation function. We name this effect the *distortion by continuum fitting*; it needs to be correctly modelled when fitting the correlation function.

Typical ranges chosen to define the Ly $\alpha$  forest and extract the transmission field are between 1040 and 1200 Å in the quasar rest-frame. Recent analyses also consider the Ly $\beta$  forest region, between 920 and 1020 Å, where both Ly $\alpha$  and Ly $\beta$  absorption are present. The absorption in this region can be assigned a redshift that depends on the choice of  $\lambda_{\text{rest}}$ , that can be either Ly $\alpha$  = 1216 Å or Ly $\beta$  = 1025 Å. These rest-frame wavelengths are separated enough such that both can be used in clustering measurements without much contamination at separations below  $200 h^{-1} \text{Mpc}$ .

Uncertainties of the transmission fluctuations are also estimated from the data themselves. Typically two major components are taken into account when defining uncertainties: instrumental noise and the intrinsic variance of absorbers. The former is essentially the output of the data reduction pipeline, described in Chapter 2, corrected with some normalisation factor. The latter is estimated from the variance of  $\delta_F$  observed in the data. The intrinsic variance of  $\delta_F$  is an increasing function of redshift, while the instrumental noise is typically decreasing with observer-frame wavelength, since forest mostly lie at the blue end of the spectrographs. The inverse of the final pixel uncertainty squared is used as a weight in the estimates of the correlation function.

Word on DLAs ?

Word on calibration residuals and my work to find/fix the problem ?

### 3.2.2 Two-point correlation functions

Once the transmission fluctuations  $\delta_F$  and their weights  $w$  are estimated for all pixels of all forests, we compute their auto-correlation function and their cross-correlation with quasars (or any other point tracer) in three dimensions, as a function of comoving radial and transverse separations.

The first step is to convert redshifts to comoving distances using a fiducial cosmology. With angular positions and distances, we can obtain the separation  $\vec{r} = (r_\perp, r_\parallel)$  between two tracers, where  $r_\perp$  is the component orthogonal to the line-of-sight and  $r_\parallel$  is the component along the line-of-sight.

The correlations are estimated in bins of separation. We consider usually bins of  $4 h^{-1} \text{Mpc}$  from 0 to  $200 h^{-1} \text{Mpc}$  in both radial and transverse directions. For the cross-correlation with quasars, the radial separation can be negative, meaning that the absorber is closer than the quasar from us. Let  $A$  be the index of a separation bin, the auto-correlation is defined as

$$\xi_A^{\text{auto}} = \frac{\sum_{i,j \text{ if } \vec{r}_{ij} \in A} w_i w_j \delta_{F,i} \delta_{F,j}}{\sum_{i,j \text{ if } \vec{r}_{ij} \in A} w_i w_j} \quad (3.3)$$

where the indexes  $i, j$  denote a given pixel in the forest. The sum is over all pairs of absorbers for which the separation  $\vec{r}_{ij} = \vec{r}_i - \vec{r}_j$  falls inside bin  $A$ .

The cross-correlation of absorbers with quasars is estimated with the following estimator:

$$\xi_A^{\text{cross}} = \frac{\sum_{i,j \text{ if } \vec{r}_{ij} \in A} w_i w_j \delta_{F,i} \delta_{Q,j}}{\sum_{i,j \text{ if } \vec{r}_{ij} \in A} w_i w_j}, \quad (3.4)$$

which is very similar to the auto-correlation one in Eq. 3.3. The index  $i$  runs over absorbers while  $j$  runs over quasars, but there is no  $\delta_{F,j}$  term. This estimator is valid under a few assumptions: sparsity of quasars, weak cross-correlation and weak auto-correlation. These assumptions are discussed in detail in the appendix B of Font-Ribera, Miralda-Escudé, et al.

2012.

The covariance matrix is estimated using sub-samples of the full survey. Under the assumption that each sub-sample  $s$  is independent, the estimator of the covariance between  $\xi_A$  and  $\xi_B$  is

$$C_{AB} = \frac{1}{W_A W_B} \sum_s W_A^s W_B^s [\xi_A^s \xi_B^s - \bar{\xi}_A \bar{\xi}_B], \quad (3.5)$$

where  $W_A^s$  is the total weight in bin  $A$  of sub-sample  $s$  and  $W_A \equiv \sum_s W_A^s$ . This estimator has been tested with 100 realisations of synthetic datasets (mocks) and it shows to be robust at the current precision level.

The data vector contains around 50x50 bins, making the covariance too large (2500x2500) for the usual number of available sub-samples ( $\sim 1000$ ). To avoid the matrix to be singular, we apply a smoothing to it. The smoothing procedure considers that the correlation coefficients, defined as  $\rho_{AB} = C_{AB} / \sqrt{C_{AA} C_{BB}}$ , are only a function of  $\Delta r_\perp \equiv r_{\perp B} - r_{\perp A}$  and  $\Delta r_\parallel \equiv r_{\parallel B} - r_{\parallel A}$ . By averaging all correlation coefficients with the same  $(\Delta r_\perp, \Delta r_\parallel)$ , we obtain a 50x50 matrix which is now positive definite. The new covariance matrix is constructed by taking these averaged coefficients and multiplying them by the variances. This method is used to estimate covariance matrices for both auto and cross correlation functions, but also for the cross-covariance between  $\xi_A^{\text{auto}}$  and  $\xi_B^{\text{cross}}$ , used in joint fits (see section 3.2.4).

### 3.2.3 Correction matrices

There are two important effects to be taken into account when modelling the Ly $\alpha$  correlation functions: the distortion by the continuum fitting, discussed in section 3.2.1, and the contamination by metal absorption. The most recent analyses use matrices to convolve a binned cosmological model and obtain the final template to be compared to the measured binned correlations. We describe both corrections below.

The distortion matrix is built under the assumption that the “mistake” we make when fitting the continuum  $C$  is also a linear function of  $\log \lambda$ . We therefore remove completely the components of  $\delta_F(\lambda)$  that are proportional to a constant plus a slope. This procedure removes not only the potential mistake we made, but also the cosmological signal proportional to a constant plus a slope, though it is ok since these components should not contain much BAO information. This removal of a linear component of  $\delta_F$  is referred to as *projection*<sup>2</sup>. Thanks to the linearity of the problem, the model for the correlation function of the projected  $\delta_F$  field can be written as a linear function of the true cosmological correlation function. For the case of a binned correlation function, this relation can be written with the help of a matrix, the *distortion matrix*. The distortion matrix was first introduced in Julian E. Bautista, Nicolás G. Busca, et al. 2017 for the BAO analysis of DR12 forests, where we showed that the distortion matrix was correctly describing the clustering of mock forests after continuum fitting.

The contamination due to *metal*<sup>3</sup> absorption is mainly due to four transitions of silicon atoms for which their rest-frame wavelength is close to the Ly $\alpha$  transition. When computing the auto-correlation of forests, metal absorption creates confusion because it is interpreted as a distinct Ly $\alpha$  absorber when in fact it is the same. For example, the SiIII absorption happens at  $\lambda_{\text{rest}} = 1207 \text{ \AA}$ , close to Ly $\alpha$  for which  $\lambda_{\text{rest}} = 1216 \text{ \AA}$ . In comoving coordinates, assuming a standard fiducial cosmology, this corresponds to  $\Delta r_\parallel \approx 21 h^{-1} \text{ Mpc}$  at  $z \sim 2.3$ . At these radial

---

<sup>2</sup>This is equivalent to the removal of modes contaminated by photometric systematics in galaxy clustering, as studied in Paviot et al. 2022.

<sup>3</sup>The term *metal* is used in astronomy for elements heavier than helium.

separations and when  $r_{\perp} \sim 0$ , we see a spike in the correlation function. This peak is not due to Ly $\alpha$  absorption separated by  $21 h^{-1}$ Mpc but it is the cross-correlation between Ly $\alpha$  and SiIII absorption at near zero separation. It is the same region in the Universe absorbing both in Ly $\alpha$  and in SiIII, though the latter has a smaller amplitude. This happens for all metals with rest-frame wavelenghts close to Ly $\alpha$ . For instance, one of the SiII transitions creates a spike at  $111 h^{-1}$ Mpc, right at the BAO peak. Since Delubac et al. 2015, I worked on carefully adding metal absorption to mock forests in order to quantify their impact on BAO constraints. In Julian E. Bautista, Nicolás G. Busca, et al. 2017, we introduced a model for the Ly $\alpha$ -metal cross-correlation to be fitted altogether with the BAO model. Similarly to the distortion modelling, the Ly $\alpha$ -metal correlations can be described as a matrix times the Ly $\alpha$ -Ly $\alpha$  correlation function. This matrix is referred to as the *metal matrix*. The amplitude of Ly $\alpha$ -metal correlations is a free parameter in the BAO fits. We found that marginalising over these amplitudes makes BAO constraints slightly larger, though more conservative and robust.

### 3.2.4 The model

The model used to fit for the BAO scale on the measured correlation functions is based on a linear matter power spectrum with some empirical terms that account for redshift-space distortions, non-linear clustering, high column density systems and binning effects. The model is constructed in Fourier space and it is Fourier transformed to obtain  $\xi(r_{\perp}, r_{\parallel})$ . The latest version of the model is described in du Mas des Bourboux, Rich, et al. 2020 and I shortly present it in this section.

The model can be written, in Fourier space, as

$$P^{\text{model}}(\vec{k}) = b_i b_j (1 + \beta_i \mu_k^2) (1 + \beta_j \mu_k^2) P_{\text{QL}}(\vec{k}) F_{\text{NL}}(\vec{k}) G_{\text{bin}}(\vec{k}), \quad (3.6)$$

where  $\vec{k}$  is the wavevector, with modulus  $k$  and  $\mu_k = k_{\parallel}/k$ ;  $b_i$  and  $\beta_i$  are the linear bias and redshift-space distortions parameters, respectively, and  $i$  is a index referring to absorbers or quasars;  $G_{\text{bin}}$  accounts for the binning of the correlation function,  $F_{\text{NL}}$  is a empirical term that accounts for the non-linear effects on small scales, and  $P_{\text{QL}}$  is the linear matter power spectrum with a empirical anisotropic damping applied to the BAO peak component. The linear matter power spectrum is computed from a Boltzmann solver code, such as CAMB (Lewis et al. 2000).

The non-linear term  $F_{\text{NL}}$  is only included for the quasar-Ly $\alpha$  cross-correlation and accounts for the effect of Fingers-of-God on small-scales as well as an eventual contribution from uncertainties of redshift estimates, which can be relatively large for quasars ( $\sim 500$  km/s). This term can be modelled as a Gaussian or as a Lorentzian, as a function of a velocity dispersion parameter  $\sigma_v$  (in units of km/s). The impact of redshift errors was studied in detail in Youles et al. 2022 and it is also described in section 3.3.

The effect of high-column density systems, if indentified and modelled when fitting the continuum, is negligible. For the HCDs that are not identified, the extended absorption (called “wings”) causes  $k_{\parallel}$ -dependent broadening of the clustering (Font-Ribera and Miralda-Escudé 2012; Rogers et al. 2018). This effect is modelled through effective biases  $b_i^{\text{eff}}$  and RSD parameters  $\beta_i^{\text{eff}}$  that depend on the biases of the Ly $\alpha$  forest and those from HCDs, plus a function that depends on the distribution of column densities of the unidentified HCDs.

The metal correlations are accounted as additive terms to the Ly $\alpha$  correlations

$$\xi_A^{\text{model}} = \xi_A^{\text{Ly}\alpha \times \text{Ly}\alpha} + \sum_m \xi_A^{\text{Ly}\alpha \times m} + \sum_{m_1, m_2} \xi_A^{m_1 \times m_2}, \quad (3.7)$$

where each  $\xi^{m_1 \times m_2}$  can be written as a metal matrix  $M_{A,B}$  times the  $\xi_B^{\text{Ly}\alpha \times \text{Ly}\alpha}$  as mentioned in section 3.2.3. The metal matrix is defined as

$$M_{A,B} = \frac{1}{W_A} \sum_{(m,n) \in A, (m,n) \in B} w_m w_n, \quad (3.8)$$

where  $(m, n) \in A$  refers to pixel separations computed assuming Ly $\alpha$  absorption, while  $(m, n) \in B$  refers to pixels separations computed assuming metal absorption. This formalism was introduced in Blomqvist, Pieri, et al. 2018.

Quasars emit UV photons which ionise their surroundings slightly more than the average intergalactic medium. This is known as the *proximity effect* and it changes the average properties of Ly $\alpha$  absorption and therefore its clustering. When considering forests around a given quasar but not to its own forest, we refer to it as the transverse proximity effect. This effect is accounted for in the quasar- Ly $\alpha$  cross-correlation with the following parametric form:

$$\xi^{TP} = \xi_0^{TP} \left( \frac{1 h^{-1} \text{Mpc}}{r} \right)^2 \exp(-r/r_{UV}) \quad (3.9)$$

where  $r^2 = r_{\parallel}^2 + r_{\perp}^2$ ,  $r_{UV} = 300 h^{-1} \text{Mpc}$  is fixed and  $\xi_0^{TP}$  is a fitted amplitude.

The spectroscopic data reduction pipeline described in section 2.3 also introduces spurious correlations between spectra. For instance, sky-subtraction and flux calibration are two processes that induce correlation between two pixels at the same observed wavelength but in two distinct lines-of-sight, provided they are observed with the same spectrograph (set of 500 fibers). These correlations have been studied using quasar spectral regions deprovided of Ly $\alpha$  absorption, such as the MgII spectral region ( $\lambda_{\text{rf}} \in [2600, 2760] \text{\AA}$ ). An empirical model for this effect is included: a Gaussian, function of  $r_{\perp}$ , centered in  $r_{\perp} = 0$  but only when  $r_{\parallel} = 0$ . Due to the effect of distortion caused by continuum fitting, these spurious correlations due to data reduction also propagate to pairs with  $r_{\parallel} \neq 0$ . The amplitude and characteristic length of this effect are two free parameters in the fit of the Ly $\alpha$  auto-correlation function.

The correlation function model accounts for the distortion matrix, as discussed in section 3.2.3. The distorted correlations are written as

$$\xi_A^{\text{dist}} = \sum_{A'} D_{AA'} \xi_{A'}^{\text{model}}. \quad (3.10)$$

It is also possible to add arbitrary smooth functions of separation in order to account for any unexplained correlations and improve the fit to the data. These functions are used to marginalise over any potential information on BAO coming from the full-shape of the correlation functions, which is avoided. This is commonly done in galaxy clustering analysis as I will show in Chapter 4.

### 3.2.5 BAO constraints

The last essential ingredient to be added to the model of correlations are the Alcock-Paczynski (AP) parameters. Thanks to the observed baryon acoustic scale, which we know should be isotropic and have a comoving size of  $r_d \sim 105 h^{-1} \text{Mpc}$ , the AP parameters can be well constrained with the data. These AP parameters account for small differences between the assumed fiducial cosmology, used to convert redshifts into distances, and the measured cosmology extracted from the observed BAO peak position.

We commonly use two AP parameters, encoding radial and transverse dilation effects. They

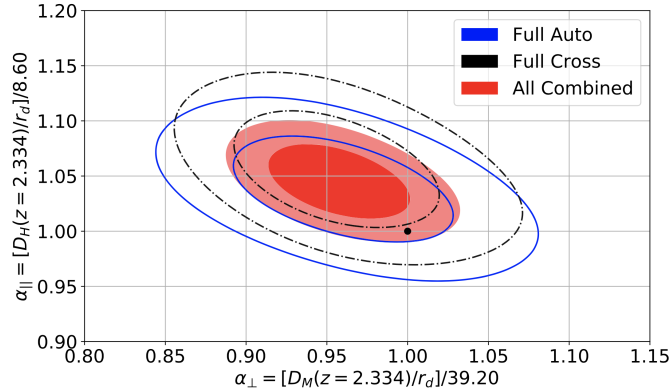


Figure 3.1: BAO constraints from the SDSS DR16 sample of Ly $\alpha$  forests. The contours show the 68 and 95 per cent confidence levels for the Alcock-Paczynski parameters  $\alpha_{\perp}$  and  $\alpha_{\parallel}$  from the fits to the Ly $\alpha$ -Ly $\alpha$  auto-correlation (blue solid), the quasar-Ly $\alpha$  cross-correlation (black, dash-dotted), and the joint fit of auto+cross (red shades). Given the high level of shot-noise of the quasar sample, the covariance between constraints from the auto and cross correlation are found to be negligible. Extracted Figure 12 from du Mas des Bourboux, Rich, et al. 2020.

can be written as ratios of the observed  $\Delta z_{\text{BAO}}$  and  $\Delta \theta_{\text{BAO}}$  at a given effective redshift  $z_{\text{eff}}$  from equations 1.22 and 1.21 of section 1.5.4, yielding

$$\alpha_{\parallel}(z_{\text{eff}}) = \frac{D_H(z_{\text{eff}})}{D_H^{\text{fid}}(z_{\text{eff}})} \frac{r_d^{\text{fid}}}{r_d} \quad (3.11)$$

$$\alpha_{\perp}(z_{\text{eff}}) = \frac{D_M(z_{\text{eff}})}{D_M^{\text{fid}}(z_{\text{eff}})} \frac{r_d^{\text{fid}}}{r_d} \quad (3.12)$$

where  $D_H$  and  $D_M$  are respectively the Hubble and comoving angular diameter distances (Eqs. 1.2 and 1.4).

The AP parameters  $\alpha_{\parallel}$  and  $\alpha_{\perp}$  are used to scale separations when computing the correlation function model as

$$\xi(r'_{\perp}, r'_{\parallel}) = \xi(\alpha_{\perp} r_{\perp}, \alpha_{\parallel} r_{\parallel}), \quad (3.13)$$

and they are let free when fitting correlations. The BAO constraints are defined by the posteriors of  $\alpha_{\perp}$  and  $\alpha_{\parallel}$ , after marginalising over all other free parameters of the model.

Figure 3.1 shows the current BAO constraints from the SDSS DR16 sample of Ly $\alpha$  forests (containing both Ly $\alpha$  and Ly $\beta$  absorption) and quasars (du Mas des Bourboux, Rich, et al. 2020). The marginalised constraints from the joint fit of auto and cross-correlations are

$$D_H(z = 2.334)/r_d = 8.99^{+0.20}_{-0.19} \quad (3.14)$$

$$D_M(z = 2.334)/r_d = 37.5^{+1.2}_{-1.1} \quad (3.15)$$

$$\rho(D_H/r_d, D_M/r_d) = -0.45 \quad (3.16)$$

which represent a 2.2 per cent BAO measurement in the radial direction and a 3.2 per cent in the transverse direction.

### 3.3 Impact of redshift errors

This section concerns work led by Samantha Youles, PhD candidate under my supervision at the University of Portsmouth between 2018 and 2022. The full details are presented in Youles et al. 2022.

A key element in the BAO analysis using forests is the quasar redshifts, which can be challenging to measure precisely when compared to galaxy redshifts. Quasar spectra are basically composed of thermal continuous emission from their accretion disk around their supermassive black holes in the centre of their host galaxies plus some broad emission lines. Typical quasar spectra from SDSS or DESI do not present detected narrow absorption or emission lines from the host galaxy itself, which would considerably improve the uncertainties on their redshifts. Previous studies using quasars as tracers for clustering (Zarrouk et al. 2018; Lyke et al. 2020) estimated that quasar redshift uncertainties range from 100 km/s at  $z \sim 1$  to 400 km/s at  $z \sim 2$ , while galaxies (LRGs or ELGs) have redshift uncertainties below  $\sim 50$  km/s. Of course, these uncertainties depend on the spectrograph and on which broad emission lines are visible for a given quasar.

In addition to statistical uncertainties in the determination of redshift, Shen et al. 2016 has shown that redshifts derived from broad emission lines of quasars have intrinsic scatter and systematic shifts of the order of hundreds of km/s with respect to the host galaxy redshift. Current redshift fitting algorithms based on templates do not account for these shifts. While Youles et al. 2022 studies the impact of scatter, we did not study in detail the impact of systematic shifts.

The uncertainties in the redshift measurements smear the two-point statistics of the quasars over separations along the line-of-sight. The smearing directly impacts the BAO measurement, particularly reducing the signal-to-noise ratio of estimates of  $\alpha_{\parallel}$  (see section 3.2.4).

Non-linearities induce large peculiar velocities on scales below a few Mpc and are commonly modelled as a random scatter in the radial direction. These non-linearities are known as *fingers-of-God* (FoG) and they smear the two-point statistics in a similar manner than redshift errors, though I will show the differences.

In this section, these two types of extra scatter in quasar redshifts are parametrised by

- $\sigma_{v,z}$  as the scatter induced by uncertainties in redshift determination, or redshift errors.
- $\sigma_{v,\text{FoG}}$  as the scatter induced by non-linear motions on small scales, or Fingers-of-God.

Using DESI mock catalogues of the 5-year sample of Ly $\alpha$  forests and quasars, we studied the impact of each of these types of extra scatter on the clustering and on BAO constraints. We discovered a new feature arising from redshift errors that modifies the shape of the two-point statistics in a non-trivial manner, though it does not impact BAO constraints expected with DESI.

Figure 3.2 presents correlation functions, both for the quasar- Ly $\alpha$  cross-correlation and for the Ly $\alpha$  auto-correlation, in averages over  $\mu_r \equiv r_{\parallel}/r$ . There are three sets of mocks

- 1) fiducial ones where  $\sigma_{v,\text{FoG}} = 150$  km/s and  $\sigma_{v,z} = 0$ ,
- 2) mocks with  $\sigma_{v,\text{FoG}} = 500$  km/s and  $\sigma_{v,z} = 0$  and
- 3) mocks with  $\sigma_{v,\text{FoG}} = 150$  km/s and  $\sigma_{v,z} = 500$  km/s.

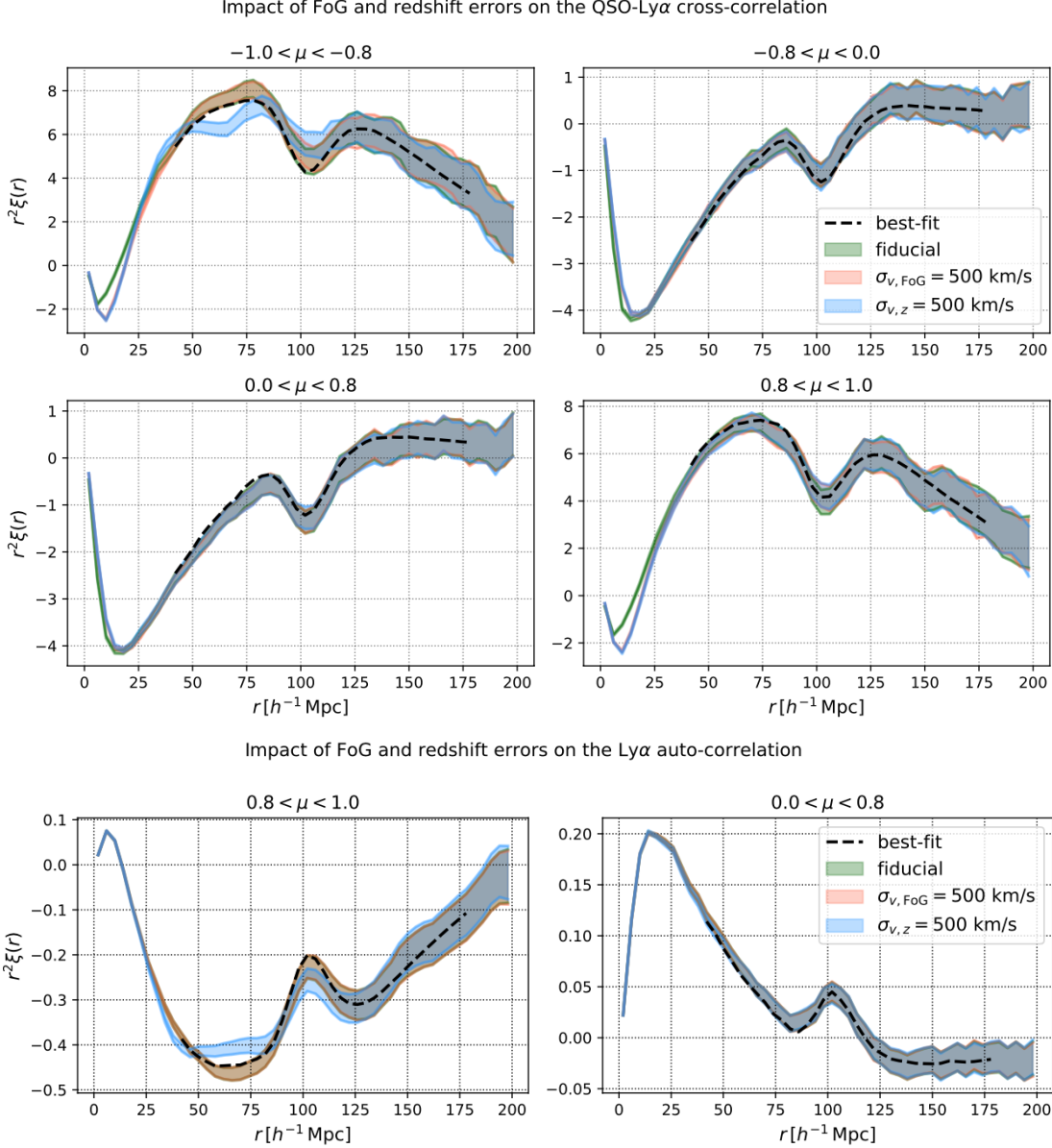


Figure 3.2: Wedges of the correlation functions versus comoving separation. Top four panels show the QSOx Ly $\alpha$  cross-correlation (top four panels) while the bottom two panels show the Ly $\alpha$  auto-correlation of forests. These are estimated from DESI mock catalogues reproducing the full 5-year sample. The green bands show the measurement from the standard mocks, with a small value of  $\sigma_{v,\text{FoG}} = 150 \text{ km/s}$  and no redshift errors; the pink bands (indistinguishable from the green in the cross-correlation) correspond to the mocks generated with an extreme value of  $\sigma_{v,\text{FoG}} = 500 \text{ km/s}$ ; the blue bands show the results for mocks with large redshift errors of  $\sigma_{v,z} = 500 \text{ km/s}$ . These measurements are computed from the average of 10 realisations of the complete 5-year DESI survey, and the width of the bands corresponds to the scatter between realisations. Note that  $\mu > 0$  ( $\mu < 0$ ) corresponds to configurations where the Ly $\alpha$  pixels are behind (in front of) the neighbouring quasar.

Each set of mocks contains ten realisations, results are averaged for each set. The colour bands show the scatter amongst realisations and are equivalent to the noise expected for the 5-year sample. We can see that FoG (orange bands) do not have a significant impact except on the cross-correlation on small scales. However, redshift errors do create a new oscillatory feature both in the auto and cross-correlations at separations of  $20\text{--}50 h^{-1}\text{Mpc}$  but only those along the line-of-sight. Using other mock catalogues with increasing values of  $\sigma_{v,z}$  (not shown here) makes these features stronger. This work puts in evidence this effect for the first time.

In Youles et al. 2022, we claim that the oscillatory features appearing when adding redshift errors to quasars is due to two main factors: the smoothing of emission lines in the continua and the clustering of the quasars. These two factors *combined* create this new effect. The smoothing of the mean continuum is illustrated in Figure 3.3 for increasingly large values of  $\sigma_{v,z}$ . These oscillatory features defined by the difference between true and estimated continua are imprinted on the clustering thanks to the fact that quasars themselves are clustered.

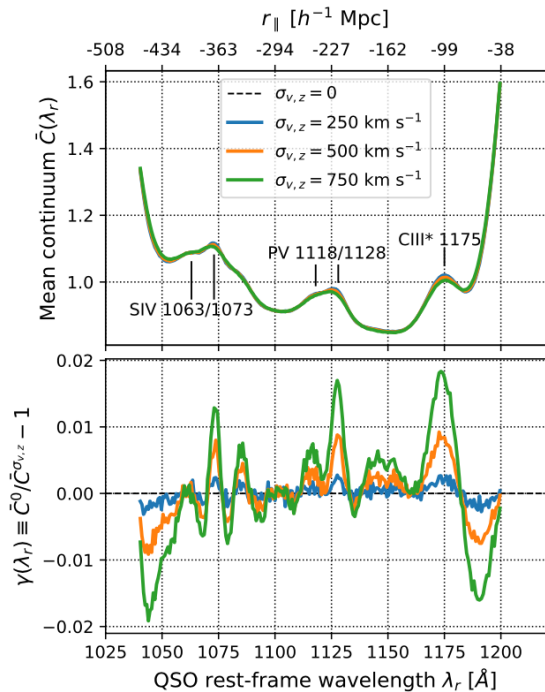


Figure 3.3: Effect of redshift errors on the mean continuum. The top panel shows the mean continua for no-forest mocks without errors, and with increasingly large redshift errors:  $\sigma_{v,z} = 0, 250, 500$  and  $750 \text{ km/s}$ . The positions of some of the strongest emission lines are annotated. The lower panel shows the ratio between the continua with and without redshift errors. The top axis on the top panel shows the radial separations between pixels and the quasar, assuming that the quasar is at redshift  $z_q = 2.3$ .

We tested our hypothesis by creating two special sets of mock catalogues, one where quasars are deprovided of forest absorption, and one where quasars are not clustered. With the first set of mocks, features are still present with the same amplitudes as the standard mocks. This points to the fact that the Ly $\alpha$  forest and their correlations do not play a role in this effect. For the second set of mocks, the features disappear in the correlation functions, demonstrating

that the quasar clustering is a key ingredient to explain the effect.

While this model is satisfactory to explain the features in the cross-correlation, the auto-correlation seems to require an additional ingredient that we could not identify. We leave this investigation for future work.

We performed BAO fits on all sets of mocks for different values of  $\sigma_{v,z}$  and  $\sigma_{v,\text{FoG}}$ . We employ the exact same model described in section 3.2.4, though we did not include metals or high-column density systems. We do not attempt to model the effect of redshift errors when fitting for BAO. We see an increased value for the  $\chi^2$  of the fits when increasing the value of  $\sigma_{v,z}$ , simply because these features are not modelled properly. The inferred BAO parameters  $\alpha_{\parallel}$  and  $\alpha_{\perp}$  do not see significant shifts or trends versus  $\sigma_{v,z}$  other than a slight increase in their uncertainties.

We believe that for the final analysis of the 5-year DESI sample the impact of redshift errors has to be correctly modelled in order to reduce the uncertainties in BAO parameters or to extract cosmological information from the full-shape of the correlation function Cuceu et al. 2021.

### 3.4 Weak-lensing of forests

This section also concerns work led by Samantha Youles, PhD candidate under my supervision at the University of Portsmouth between 2018 and 2022.

Weak-gravitational lensing is a powerful cosmological probe since it is sensitive to the total (baryons and dark) matter density field, as discussed in section 1.5.7. The quasar and Ly $\alpha$  forest samples used in the measurement of BAO lie at  $2.0 < z < 4.0$  and are subject to the effect of lensing from the matter distribution between  $0 < z < 2.0$ . Current BAO analysis such as the one described in section 3.2 do not take any lensing effect into account. In this section we describe how one could potentially extract weak-lensing information from a realistic set of Ly $\alpha$  forests.

Until now, no measurement of weak gravitational lensing with sources at  $z \sim 2$  has been produced, though it has been studied theoretically and with simplified simulations. Croft, Romeo, et al. 2018, Metcalf, Croft, et al. 2018, and Metcalf, Tessore, et al. 2020 looked into a regular grid of mock quasars with arcminute separations, populated with Gaussian random forests. The close, regular spacing of the forests created a near-continuous field enabling the use of a quadratic estimator adapted from 21cm intensity mapping analyses Pourtsidou et al. 2014; Pourtsidou et al. 2015. Even though these techniques are able to reconstruct the lensing potential, they are not yet readily applicable to real survey data given its non-regular sampling, noise, volumes and densities probed.

Figure 3.4 illustrates the impact of lensing over a pair of Ly $\alpha$  forests caused by an intervening overdensity. The lens creates an image of the pair at a slightly larger angle with respect to the observer, virtually increasing the transverse separation  $r_{\perp}$  between the two forests to a larger value  $r_{\perp}^L$ . Of course, the expected correlation function between two given pixels is unchanged and given by  $\xi(r_{\perp}, r_{\parallel}) = \langle \delta_1 \delta_2 \rangle$  where the brackets indicate an ensemble average. When observing a set of lensed quasars, the measured correlations are wrongly assigned to the separation given by  $(r_{\perp}^L, r_{\parallel}) \neq (r_{\perp}, r_{\parallel})$ . Here we assume that the radial separations changes are negligible,  $r_{\parallel}^L \sim r_{\parallel}$ . If one could measure the correlation function uniquely using pairs of forests that are background of overdense lenses, the results would be a dilated correlation function in the transverse direction. Alternatively, considering only underdense lenses, the effect would be an opposite dilation in the transverse direction.

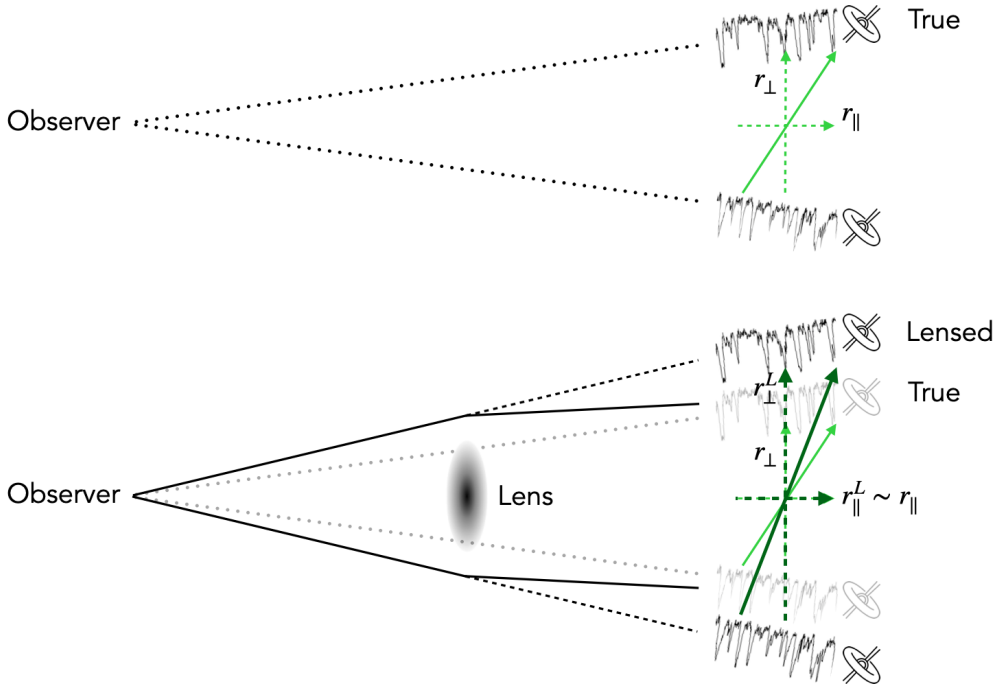


Figure 3.4: Illustration of the effect of gravitational lensing over a pair of Ly $\alpha$  forests. The top figure shows the unlensed case, the arrows define the parallel and transverse separations,  $r_{\parallel}$  and  $r_{\perp}$  respectively, of a pair of Ly $\alpha$  forest pixels (or a pixel-quasar pair). The bottom panel shows the lensed case, where an overdense region acts as a “thin” lens, creating the illusion that the background pairs are actually farther away from each other in the transverse direction. The measured correlations should be the same in both cases, though in the lensed case this correlation is assigned to a wrong transverse separation. The radial effect is relatively small.

I describe how we attempt to reconstruct the lensing signal from a simpler estimator. One should first note that when averaging correlations over all available pairs in a survey, the lensing effect from over and underdense lenses averages to a negligible net impact on the correlation function, though it increases its noise. However, we can attempt to detect a difference between the average correlation function  $\bar{\xi}(r_{\parallel}, r_{\perp})$  and the local correlation function in a given patch of the sky  $\xi(\hat{n}, r_{\parallel}, r_{\perp})$ . We can write a first-order approximate relation between the local difference  $\Delta\xi \equiv \xi(\hat{n}, r_{\parallel}, r_{\perp}) - \bar{\xi}(r_{\parallel}, r_{\perp})$  and the local convergence field  $\kappa(\hat{n})$ . In practice, each pair of forest given us an estimate of  $\xi(\hat{n}, r_{\parallel}, r_{\perp})$ , though very noisy. Our estimates of the convergence  $\hat{\kappa}(\hat{n})$  are assigned into a map by choosing  $\hat{n}$  to be the mid-point between each pair of lines of sight. Convergence maps are constructed using both the auto-correlation function of forests and the quasar- Ly $\alpha$  cross-correlation function, denoted  $\hat{\kappa}_{\alpha\alpha}$  and  $\hat{\kappa}_{q\alpha}$  respectively. Given the fact that auto- and cross-correlations are close to be independent (see section 3.2.2), the convergence maps from auto and cross can be combined into a single map, denoted  $\hat{\kappa}_{q\alpha+\alpha\alpha}$ .

Angular power spectra are computed from the estimated maps as a function of angular multipole number  $\ell$ . Since our convergence maps are quite noisy, computing the auto power spectra of these maps, e.g.  $\langle \hat{\kappa}\hat{\kappa} \rangle_{\ell}$ , is not convenient since these would also be dominated by noise. Instead, we use high signal-to-noise ratio convergence maps to compute cross angular

power spectra. In real cases, one can use a lensing convergence or potential maps derived from the cosmic microwave background or one can construct a density map of foreground sources from galaxy surveys.

We tested our methodology using simulations. We used the 5-year DESI mock catalogues of Ly $\alpha$  forests also used in the study of redshift errors (section 3.3). Gaussian lensing convergence maps were created from a fiducial cosmology and the linear matter power spectrum computed with *camb*. We displaced the quasars following these “input” convergence maps and applied our methodology to build convergence maps from the auto- and cross-correlation functions. The analysis was performed 100 times with different realisations of the convergence maps (the forests were kept the same).

Figure 3.5 shows the resulting power spectra compared to the input convergence maps as a function of multipole  $\ell$ . There are two effects to be taken into account when comparing to theory. First, the survey mask changes the amplitude of the power spectra by a factor equal to the fraction of sky covered (to first order). The resulting power is shown as a blue line. Second, the power spectra depend on the choice of maximum transverse separation  $r_{\perp}^{\max}$  between quasars used to build the convergence maps. We refer to this non-trivial function of  $\ell$  describing the variation of power with  $r_{\perp}^{\max}$  as “damping”. Both effects combined are shown as a purple line.

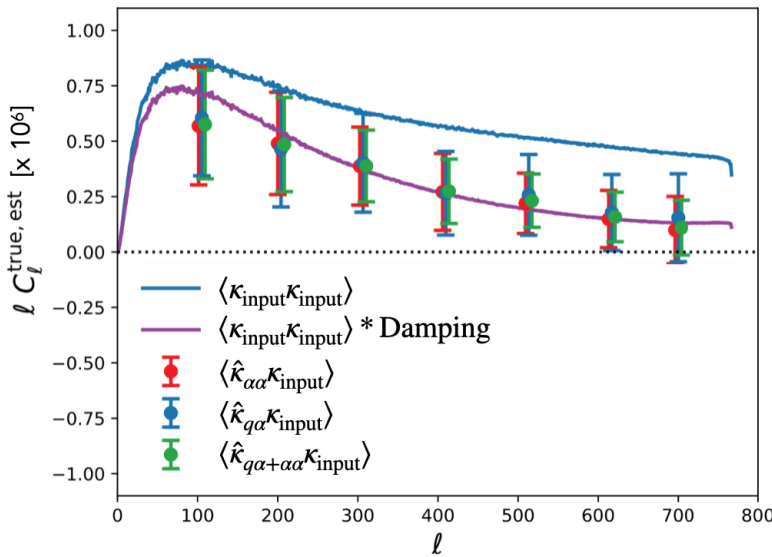


Figure 3.5: Angular power spectra of convergence maps from simulations of the 5-year DESI sample of Ly $\alpha$  forests. The blue line indicates the auto power spectra of the input convergence when accounting for effect of survey mask. The purple line also includes the effect of the choice of maximum transverse separation between lines of sight used when building the convergence maps. The points show the estimated cross power from maps computed from the auto-correlation of forests (red), the cross-correlation between quasars and forests (blue), and the combination of both (green).

There is an excellent agreement, though noisy, between estimated cross-power spectra and their input values. Of course, the “input” map is not available in a real setting so one should consider the noise of this second map (e.g. CMB lensing map) when producing realistic

forecasts.

The results presented in this section are still under development and have not yet been published. We refer the reader to S. Youles thesis for more details on methods and tests.

### **3.5 Voids in tomographic maps**

Ravoux et al. 2022

# 4 The mid-redshift Universe and its galaxies

## Contents

4.1	From redshifts to clustering catalogues	45
4.2	Reconstruction of linear density field	50
4.3	Mock catalogues	51
4.4	From catalogues to clustering estimates	52
4.4.1	Correlation function	52
4.4.2	Power spectrum	53
4.4.3	The clustering of eBOSS DR16 LRGs	55
4.5	Baryon acoustic oscillations	57
4.6	Redshift-space distortions	59
4.7	Joint clustering analysis in Fourier and Configuration space	63
4.8	Cross-correlation with radio surveys	66

At redshifts between 0 and 2, galaxies can be used as tracers of the matter distribution. With the statistics of the galaxy distribution we can measure the characteristic scale of the baryon acoustic oscillations (BAO) as well as extract information about the growth-rate of structures from the anisotropies caused by redshift-space distortions (RSD). As presented in Chapter 1, BAO and RSD are powerful probes of dark-energy and theories of gravity.

In this chapter, I overview my contributions for the study of dark-energy with galaxy clustering. Section 4.1 describes how to create a galaxy clustering catalogue from the spectroscopic observations, including corrections for all known systematic effects caused by photometry or spectroscopy. Section 4.2 describes reconstruction techniques used to increase the precision of BAO measurements. Section 4.3 presents the mock catalogues that are used to test our methodology and section 4.4 I overview the two-point statistics estimates, either in Fourier space or in configuration space. In section 4.5 I present the BAO measurements I performed with the SDSS sample of luminous red galaxies, while section 4.6 focus on the RSD constraints. Section 4.7 overviews recent work carried out by my PhD students Tyann Dumerchat and Vincenzo Aronica on the joint analysis of galaxy clustering in Fourier and configuration space.

The work described in this chapter is published in the following articles: Julian E. Bautista, Vargas-Magaña, et al. 2018; Julian E Bautista et al. 2020; Gil-Marín et al. 2020; A. J. Ross et al. 2020; Zhao et al. 2021.

## 4.1 From redshifts to clustering catalogues

An essential step in the cosmological analysis of galaxy survey data is to convert convert a list of galaxy redshifts (see Chapter 2) into a catalogue from which we can define overdensities  $\delta_n(\vec{x}) = n(\vec{x})/\bar{n} - 1$ , where  $n(\vec{x})$  is the number density of galaxies in a volume element located at position  $\vec{x}$ . The quantity  $\bar{n}$  is the average galaxy number density over the probed *volume*. Therefore, it is important to 1) define precisely what is the volume observed, or in jargon terms,

the survey window function; and 2) to make sure that the number density of galaxies is tracing the actual cosmological fluctuations and not any spurious contamination.

The simplest form of survey window function would be a function of position  $\vec{x}$  that yields 1 if  $\vec{x}$  is inside the survey volume and 0 else. One convenient way to define this function is using a large set of randomly and uniformly distributed positions encompassing the survey volume. Each random position would have a weight of either 1 or 0, depending if it is located inside or outside the observed volume. This list of positions and their weights is referred to as the *random catalogue* or the *randoms*. Typically, randoms are sampled at some arbitrary higher number density than the galaxy average number density (typically between 20 or 50 times higher), to reduce the noise in the description of the window function. As we will see next, the random catalogue is slightly more complex: the weights are used to account for observational completeness and systematic effects. In SDSS analyses, the random catalogue is a product of an angular and a radial selection function.

I describe now the procedure to define the angular footprint. The starting footprint is the one used in the process of target selection (section 2.1). Figure 4.1 displays the eBOSS footprint for three tracers (LRGs, ELGs and QSOs) compared to the BOSS footprint and the stellar density map from Gaia. Regions with bad photometric or around bright stars are masked out by removing randoms belonging to these regions (or assigning them a null weight). After tiling, fibre assignment and spectroscopic observations, the footprint can be divided into an unique set of sectors. Each sector corresponds to regions observed by one or more plates. The *fibre completeness* of each sector is defined as the ratio between the number of spectroscopically observed targets and the number of available targets in the sector. Randoms are sub-sampled or de-weighted following the fibre completeness to correct for its effect.

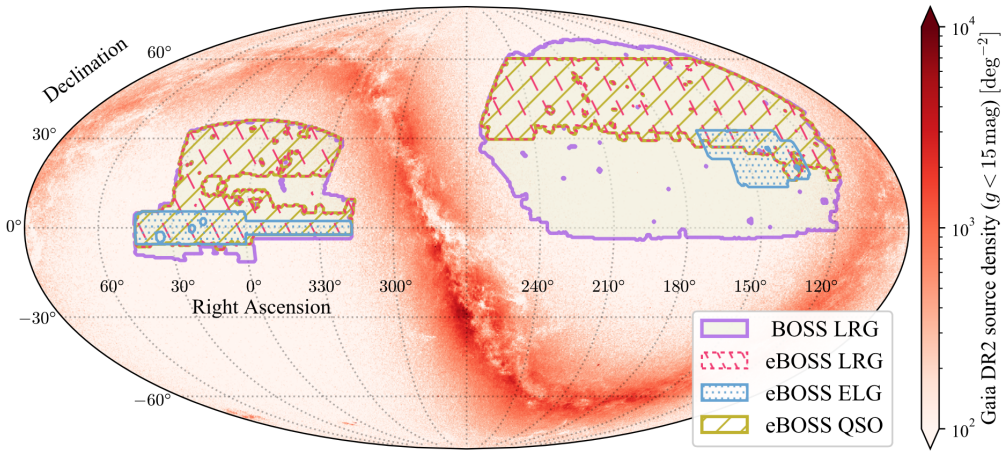


Figure 4.1: The DR16 footprint for each eBOSS tracer: Luminous Red Galaxies (LRG), Emission Line Galaxies (ELG) and quasars (QSO). The BOSS DR12 LRGs area is also shown, as well as the density map of Gaia DR2 sources with  $g < 15$  mag. Figure extracted from Zhao et al. 2021.

Some targets cannot be observed due to its proximity to another observed target and the finite size of fibres, corresponding to 62 arcseconds in the sky. We refer to these events as *fibre collisions*. Collisions might happen not only to pairs of galaxies, but to any group of targets with linking lengths smaller than 62 arcsec. Depending on the number of plates observing a giving sector, some collisions might be solved but the missing ones impact the measured clustering

on small scales if not corrected. While there are several methods to solve collisions (Guo et al. 2012; Bianchi and Will J. Percival 2017), we used the simplest up-weighting technique, where the nearest observed galaxy is up-weighted by the number of non-observed targets within the collision group. This assumes that non-observed targets are also galaxies of the same target type and that they are physically close (angularly and radially) to the observed ones. On scales above a few  $h^{-1}\text{Mpc}$ , this simple correction is a good approximation.

Two additional sets of weights are defined to correct for spurious density fluctuations contaminating cosmological fluctuations in which we are interested. These weights could be applied to randoms but we chose to apply these to the galaxy themselves.

The first set of weights corrects for angular fluctuations caused by correlations between galaxy number density and photometry-related quantities, such as Galactic extinction, stellar density, imaging depth or sky flux. They are commonly referred to as *photometric weights*. Figure 4.2 displays these correlations for the LRG sample both before and after applying correction weights. For the analysis of eBOSS DR16 LRGs, I have implemented<sup>1</sup> a multi-dimension linear regression that assumes these correlations are linear and accounts for the fact that some photometric quantities are correlated between themselves (e.g., stellar density and Galactic extinction). This multi-linear method is based on work described in Prakash et al. 2016. Of course, more advanced methods have been developed since then, based on machine learning algorithms (Rezaie, Seo, et al. 2020; Chaussidon et al. 2021). It is important to evaluate the performance of these algorithms with mock catalogues where we add artificial contamination and quantify how well we recover the initial raw power spectrum after correcting for them. There is a risk of overfitting and removing some large-scale cosmological modes which can be harmful for clustering analysis, particularly those aiming at measuring primordial non-Gaussianity (Rezaie, A. J. Ross, et al. 2021; Mueller et al. 2021).

---

<sup>1</sup>[https://github.com/julianbautista/eboss\\_clustering/blob/master/python/systematic\\_fitter.py](https://github.com/julianbautista/eboss_clustering/blob/master/python/systematic_fitter.py)

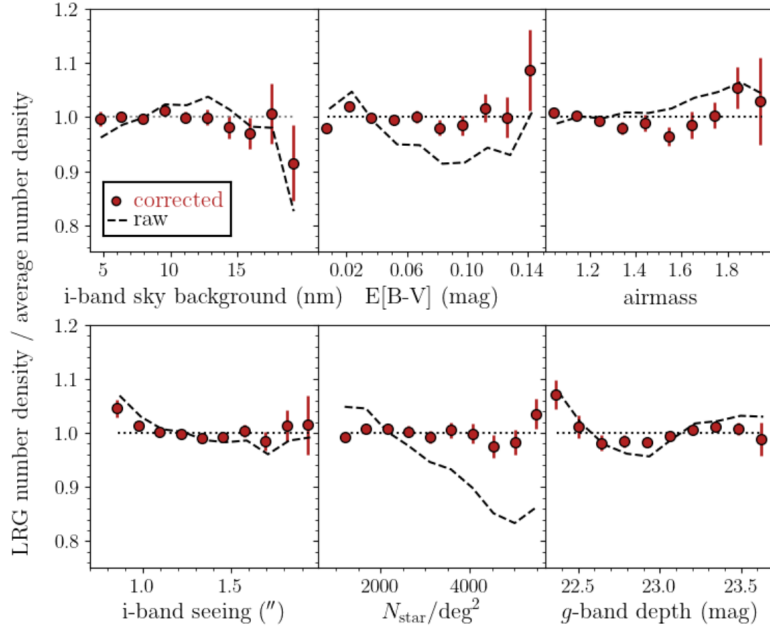


Figure 4.2: Fluctuations in the angular LRG density as a function of various imaging properties and Galactic foregrounds. The dashed curves show these fluctuations before any correction while red points show the result of applying a linear correction for stellar density and Galactic extinction. Figure extracted from A. J. Ross et al. 2020.

The second set of weights corrects for the so-called *redshift failures*, which are spectra with low signal-to-noise ratio (S/N) not yielding a statistically significant redshift measurement. If redshift failures were randomly distributed across the sky, they would not introduce any particular bias to the clustering. However, given the particular configuration and throughput of the SDSS spectrographs, these failures imprint a pattern in the sky which contaminates clustering. The left panel of Figure 4.3 displays the average failure rate of eBOSS LRGs as a function of position in the focal plane. This pattern is due to the fact that fibres at the side edges of the focal plane transport light to the edges of the CCDs which have a lower-than-average throughput. The right panel of Figure 4.3 shows the dependency of the average redshift failure rate as a function of the signal-to-noise ratio of the observation<sup>2</sup>. When modelling these dependencies of failure rates with S/N (or fibre number or focal plane position), one can correct these spurious fluctuations by assigning a weight inversely proportional to the modelled rate. These *redshift-failure weights* are assigned to the galaxies with confident redshift measurements, to compensate for the eventual non-confident ones at the same location in the focal plane.

<sup>2</sup>The signal-to-noise ratio of an observation was defined internally as a function of the signal-to-noise ratio of all observed spectra and their magnitudes.

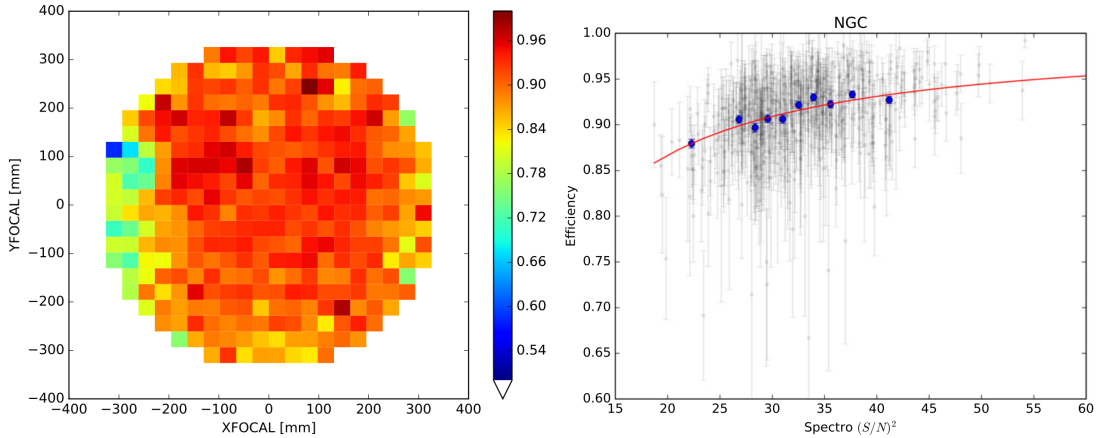


Figure 4.3: Average redshift efficiency as a function of physical position of the optical fiber in the focal plane (left panel) and as a function of the observation signal-to-noise squared (right panel). The left panel shows how redshift-failures imprint a pattern on the sky and therefore must be corrected. The right panel shows the underlying reason for the failures. The model (red line) is used to compute correction weights. Figures extracted from Julian E. Bautista, Vargas-Magaña, et al. 2018.

Once all galaxies have their correction weights (fibre collision, photometric and redshift-failure) and the randoms are corrected by fibre completeness, it is time to compute the radial selection function. The idea is to assign redshifts to randoms such that they follow the same redshift distribution as the galaxies. The redshift distribution is often quantified by the comoving galaxy (weighted) number density  $\bar{n}(z)$ . Figure 4.4 shows the comoving density of eBOSS tracers as a function of redshift. For randoms to match this distribution, we randomly assign galaxy redshifts to each random, with repetition. Another possibility would be to fit some smooth function over the observed  $\bar{n}(z)$  and draw random redshifts from the resulting model. All these methods introduce the so called *radial integral constraint*, i.e., the fact that the observed  $\bar{n}(z)$  is not the true ensemble averaged function of the Universe, but derived from the volume-limited realisation that we observe. The impact on clustering of the radial integral constraint is inversely proportional to the area of the footprint (de Mattia and Ruhlmann-Kleider 2019) and it is significant for surveys such as the eBOSS ELG (see Figure 4.1 and Tamone et al. 2020; de Mattia, Ruhlmann-Kleider, et al. 2021).

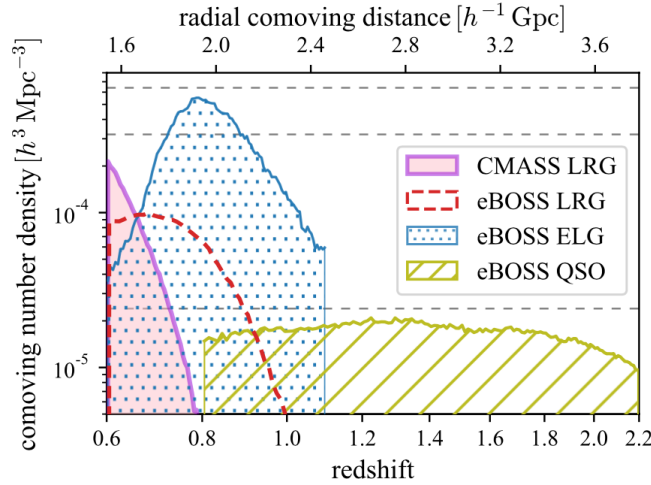


Figure 4.4: The weighted comoving number densities  $\bar{n}(z)$  of eBOSS DR16 tracers and BOSS DR12 CMASS LRGs, with all the photometric and spectroscopic systematic weights included. The comoving distances and volumes are computed assuming a flat- $\Lambda$ CDM cosmology with  $\Omega_m = 0.31$ . Figure extracted from Zhao et al. 2021.

The final step of the catalogue production consists in adding an additional set of weights to galaxies that optimise the signal-to-noise ratio of clustering measurements when the redshift distribution is not uniform. These weights were first introduced by Feldman et al. 1994 and have been applied to all clustering analysis ever since. They are commonly referred to as *FKP weights* and can be written for a galaxy  $i$  as

$$w_{i, \text{FKP}} = \frac{1}{1 + \bar{n}(z_i) P_0} \quad (4.1)$$

where  $P_0$  is a rough value of the power spectrum of the tracers at some particular scale of choice, usually BAO scales for large-scale clustering measurements. For eBOSS analyses, we chose a scale of  $k \sim 0.1 h \text{Mpc}^{-1}$  for which  $P_0 = 10000 h^{-3} \text{Mpc}^3$  for LRGs,  $P_0 = 4000 h^{-3} \text{Mpc}^3$  for ELGs and  $P_0 = 6000 h^{-3} \text{Mpc}^3$  for QSOs.

In summary, the random catalogue describes the angular and radial selection functions of the galaxy survey. Each random has a weight  $w_r = w_{\text{comp}} w_{\text{FKP}}$ , where  $w_{\text{comp}}$  accounts the spectroscopic completeness of targets and  $w_{\text{FKP}}$  are optimal weights for clustering. Each galaxy has a weight given by  $w_g = w_{\text{col}} w_{\text{photo}} w_{\text{fail}} w_{\text{FKP}}$ , where  $w_{\text{col}}$  accounts for fibre collisions,  $w_{\text{photo}}$  corrects fluctuations caused by photometry and  $w_{\text{fail}}$  corrects redshift failures. These weights are employed when computing correlation functions or power spectra (see 4.4).

## 4.2 Reconstruction of linear density field

Bulk motions of galaxies on scales of tens of Mpc impact their two-point statistics, acting as a smoothing of the clustering (Eisenstein, Seo, and White 2007). In particular, these motions smooth/broaden the BAO peak, reducing the precision on our measurement of its position. In the past decades, several methods have been proposed to reconstruct the linear density field and remove these bulk motions from a galaxy survey, therefore sharpening the BAO peak. These methods are referred to as *reconstruction* methods. Reconstruction is now an essential

part of standard BAO measurements from galaxy surveys, since they improve significantly their precision.

The simplest form of reconstruction is based on a theoretical relationship between the galaxy density field on large scales (our observable) and the displacement field connecting the observed field (Eulerian frame) to its past version (Lagrangian frame). Lagrangian perturbation theory (LPT) can predict these displacements (see F. Bernardeau et al. 2002 for a review). To first order, the relation between displacements and density is linear (Zel'dovich 1970). From the observed density field in our survey, we can compute the corresponding linear displacements and move galaxies back. Since we want to “move” the density field, we also move randoms by the same displacements. This procedure successfully removes most of the broadening of the BAO peak (Nusser and Dekel 1992; Eisenstein, Seo, Sirk, et al. 2007). The first order LPT reconstruction is often called *Zeldovich reconstruction*. Extending to second order LPT does not improve BAO reconstruction significantly (Seo, Eckel, et al. 2010) but it helps on recovering the velocity field (Kitaura et al. 2012). Zeldovich reconstruction has been used in all BAO measurements from SDSS (BOSS and eBOSS). I implemented a python version<sup>3</sup> of the Zeldovich reconstruction that uses Fast Fourier Transforms while accounting for the large angle effects (Burden, W. J. Percival, Manera, et al. 2014; Burden, W. J. Percival, and C. Howlett 2015). Alternatively, displacements can be computed in configuration space using finite difference approximations (Padmanabhan, Xu, et al. 2012) though these are slower and less precise than iterative FFTs.

Since we do not observe the actual density of matter, a bias relation between galaxy number density and matter density has to be assumed in reconstruction. Usually we assume a linear bias relation, where the bias value is estimated from the clustering of the standard galaxy catalogue. This is a reasonable approximation since reconstruction uses fluctuations on scales larger than  $\sim 15 h^{-1}\text{Mpc}$ . It is also possible to remove linear redshifts-space distortions, by assuming a value for the growth-rate of structures  $f$  (see section 1.5.6) used to convert the displacements into velocities. The radial components of the estimated velocities are then removed from each galaxy. Therefore, the clustering of reconstructed catalogues depend on the fiducial values of bias and  $f$ , but less on the distance-redshift relation (Carter et al. 2020).

There are other backward reconstruction techniques such as those based on the least action principle (LAP). First proposed by Peebles 1989, it was extended to cosmological applications by Nusser and Branchini 2000; Sarpa, Schimd, et al. 2019. Sarpa, Veropalumbo, et al. 2021 applied it for the BAO measurement of the BOSS DR12 galaxy sample.

Reconstruction is essential to improve the precision on BAO measurements. However, due to imperfections in recovering the true initial conditions, reconstruction has not yet been used in attempts to derive cosmological constraints from the full-shape of the reconstructed two-point statistics. Therefore, analysis of redshift-space distortions are based on the non reconstructed clustering (see section 4.6).

### 4.3 Mock catalogues

An important limitation in cosmology is that we only have a single realisation of our Universe. Therefore simulations are an essential tool to overcome this limitation.

We can recognise two types of simulations mainly used in cosmology. First, n-body simulations (eventually including gas) solve numerically for the formation of structures and are

---

<sup>3</sup>[https://github.com/julianbautista/eboss\\_clustering/](https://github.com/julianbautista/eboss_clustering/)

computationally expensive. They focus on the fully non-linear aspects and require a higher resolution setting, preventing them to simulate very large volumes or producing numerous realisations. N-body simulations are still the baseline for tests of perturbation theory models. See Angulo et al. 2022 for a review on cosmological n-body simulations. The second type of simulations are the so-called *mock catalogues* or simply *mocks*. They are lower resolution and do not fully describe the non-linear clustering but they are faster to produce both in large volumes and in large number of realisations. Their are key for the understanding of biases in best-fitted quantities and on their uncertainties in clustering analyses. Given the large number of realisations, mocks have been the most reliable method to estimate covariance matrices of clustering measurements. Also, mocks are used to study the impact of observational systematic effects on our measurements. All previous cosmological measurements from galaxy surveys have associated sets of n-body simulations and mock catalogues. I will describe the example I was involved in, the case of EZMOCKS produced for the eBOSS DR16 clustering measurements.

A set of 1000 EZMOCK realisations of the eBOSS survey were produced for three tracers: LRGs, ELGs and QSOs. They are fully described in Zhao et al. 2021. These mocks employ an effective Zeldovich approximation to evolve the density field in longer time steps (Chuang et al. 2015). By construction, these mocks match the large-scale clustering of the target data sample, including 2 and 3-point statistics. They have some extra free parameters to simulate a biased galaxy sample and non-linear motions on small-scales. The eBOSS EZMOCKS also include light-cone effects produced by interpolating boxes at different redshifts.

The last step in the production of EZMOCKS was the addition of systematic effects. I was responsible of implementing all known observational effects from the data onto the mocks. A simple script<sup>4</sup> gathers the information from the real catalogues and simulates fibre collisions, spurious fluctuations caused by photometry and spectroscopy. These contaminated mocks are then corrected using the same algorithms as for the real data, as described in section 4.1. The clustering before and after adding those effects is extensively compared to real data (Zhao et al. 2021) and the agreement is found to be excellent on the scales of interest for BAO and RSD measurements.

## 4.4 From catalogues to clustering estimates

Once the catalogue of galaxies and the associated random catalogue are ready, any statistical quantity can be computed, such as  $n$ -point statistics. As discussed in section 1.4, these statistics can be computed in either configuration space or Fourier space. This section describes how to obtain 2-point function estimates, in both spaces, which are the statistics I worked with.

### 4.4.1 Correlation function

The estimate of the correlation function  $\xi(\vec{r})$  is based on counting pairs of galaxies in bins of separation  $\vec{r}$  and comparing it to same numbers obtained from the random catalogue. For the estimator we use, there is no need to calculate galaxy number densities  $n(\vec{x})$  or overdensities  $\delta_n(\vec{x})$  in some mesh. To optimise the variance of the estimator while keeping it unbiased, Landy et al. 1993 proposed to include the cross-pairs between galaxies and randoms in the

---

<sup>4</sup>[https://github.com/julianbautista/eboss\\_clustering/blob/master/bin/ezmocks\\_add\\_systematics.py](https://github.com/julianbautista/eboss_clustering/blob/master/bin/ezmocks_add_systematics.py)

estimator, yielding:

$$\xi(\vec{r}_i) = \frac{DD(\vec{r}_i) - 2DR(\vec{r}_i)}{RR(\vec{r}_i)} + 1, \quad (4.2)$$

where  $DD(\vec{r}_i)$  (or  $RR(\vec{r}_i)$ ) are the normalised paircounts between galaxies (or randoms) at bin  $i$  corresponding to separation  $\vec{r}_i$ ,  $DR(\vec{r}_i)$  is the normalised cross-paircounts between galaxies and randoms. The normalisation of the paircounts is given by the total number of unique pairs in the catalogue, i.e.,  $N(N-1)/2$  if the catalogue contains  $N$  galaxies or  $N_g N_r$  for the cross pairs. When using weights as described in section 4.1, nothing changes except that each pair of galaxies (or randoms) are weighted as  $w_{ij} = w_i w_j$ , where  $w_i, w_j$  are the weights of each element of the pair.

More recently, new ways to account for fibre collisions or incompleteness have been proposed (Bianchi and Will J. Percival 2017; Will J. Percival et al. 2017) where each pair of galaxies would have a weight  $w_{ij} \neq w_i w_j$ , i.e., not a product of individual weights. This makes the calculation slightly slower since these weights have to be defined for each pair. These new estimators were first used with the eBOSS tracers (Mohammad et al. 2020) and are currently being employed within DESI.

The estimator in Eq. 4.2 changes slightly when dealing with catalogues resulting from reconstruction algorithms, where both galaxies and randoms are shifted in order to reduce the impact of bulk motions (see section 4.2). The Landy-Szalay estimator is now written as

$$\xi^{\text{recon}}(\vec{r}_i) = \frac{DD(\vec{r}_i) - 2DS(\vec{r}_i) + SS(\vec{r}_i)}{RR(\vec{r}_i)}, \quad (4.3)$$

where  $S$  represents the shifted random catalogue and the  $R$  is the usual random catalogue as before. See Padmanabhan, White, et al. 2009; Padmanabhan, Xu, et al. 2012 for a detailed derivation of this estimator.

Most analyses of the two-point correlation function do not use the full  $\xi(\vec{r}_i)$ , where  $\vec{r}_i$  are bins in 2D separations such as bins in  $(r_{\parallel}, r_{\perp})$  or  $(r, \mu_r)$ . Most analysis further compress the estimated correlation function into a new basis with fewer degrees of freedom. Some analyses uses the correlation function *wedges*  $\xi_{\mu_{r1}, \mu_r}(r)$ , which are averages of  $\xi$  over  $\mu_{r1} < \mu < \mu_{r2}$ , as already discussed in section 3.2.2. Other analyses, such as the one described in this chapter, decompose  $\xi$  into a basis of Legendre polynomials  $L_\ell(\mu_r)$  such that  $\xi(r, \mu_r) = \sum_\ell \xi_\ell(r) L_\ell(\mu_r)$ , where  $\xi_\ell(r)$  are the correlation function *multipoles*. Usually two or three wedges or multipoles are considered when comparing to clustering models.

One of the most recent codes to compute correlation function accounting for all features described above is PYCORR<sup>5</sup> which is being currently developed for DESI.

#### 4.4.2 Power spectrum

The power spectrum is the analogous of the correlation function in Fourier space. It requires a Fourier Transform of the galaxy overdensity field, which introduces some effects that have to be correctly taken into account when fitting for clustering models. The power spectrum estimation is based on work by Feldman et al. 1994; Bianchi, Gil-Marín, et al. 2015; Hand et al. 2017 and it is shortly described here.

The first step is to assign galaxies and randoms into a three-dimensional mesh, defining an

---

<sup>5</sup><https://github.com/cosmodesi/pycorr>

“overdensity” function  $F(\vec{x}_i)$  as

$$F(\vec{x}_i) = n(\vec{x}_i) - \alpha n_{\text{rand}}(\vec{x}_i), \quad (4.4)$$

where  $n_{\text{rand}}$  are the *weighted* number density of galaxies and randoms in voxel centered at  $\vec{x}_i$ ,  $\alpha$  is the ratio of the total weighted number of galaxies to the total weighted number of randoms. The field  $F(\vec{x})$  is also known as the FKP field.

The field  $F(\vec{x})$  can be Fourier transformed numerically using Fast Fourier Transform (FFT) algorithms. The power spectrum would be defined as the absolute value squared of this field. Power spectrum *multipoles* are commonly used, as it was the case in configuration space. They can be expressed as:

$$P_\ell(k) = \frac{1}{I_{22}} \left[ (2\ell + 1) \left\langle F_0(\vec{k}) F_\ell(-\vec{k}) \right\rangle_{V_k} - (1 + \alpha) I_{12} \delta_{0\ell} \right] \quad (4.5)$$

where the brackets  $\langle \cdot \rangle$  indicate average over spherical shells in k-space with radius  $|\vec{k}|$ ,  $F_\ell(\vec{k})$  are the overdensity multipoles in k-space given by

$$F_\ell(\vec{k}) = \int d^3x F(\vec{x}) e^{i\vec{k}\cdot\vec{r}} L_\ell(\hat{k}\cdot\hat{x}), \quad (4.6)$$

and the normalisation factors  $I_{ab}$  are defined as

$$I_{ab} \equiv \int d^3x [n(\vec{x})]^a [w_{\text{FKP}}(\vec{x})]^b. \quad (4.7)$$

The first term in Eq. 4.5 is the usual term defining the power spectrum, i.e., the square of the absolute value of Fourier fluctuations, while the second term is the so called *shot-noise* and only affects the power spectrum monopole.

Since we use Fourier transforms which rely on periodic boundary conditions, the mesh used to compute  $F(\vec{x})$  has to be large enough to encompass the survey volume with some padding around it. Also, because of the assumption of periodicity, the estimated power spectra will be convolved by the window/selection function of the survey. This window has to be correctly computed using the randoms and it is a key ingredient to be accounted for when modelling the clustering.

Since we use numerical FFTs, the resolution of the mesh defines the scales being probed. If the mesh has a total comoving size of  $L$  on a side and has  $N$  voxels on a side, the fundamental mode is given by  $k_F = \pi/L$  while the highest (or Nyquist) frequency is  $k_{\text{Ny}} = \pi N/L$ . Typically meshes with 512 or 1024 voxels on a side are sufficient to cover the scales of interest for BAO or RSD analyses in current survey volumes,  $0.01 < k < 0.30 (\text{Mpc}/h)^{-1}$ .

The estimated power spectra are also affected by the discreteness nature of the mesh on scales close the Nyquist frequency. The assignment of galaxies to the mesh can be optimised to reduce those effects. Also, interlacing techniques can also further reduce mesh effects. These effects and proposed solutions are described in detail in Sefusatti et al. 2016 and are implemented in the package NBODYKIT<sup>6</sup> or PYPOWER<sup>7</sup>.

---

<sup>6</sup><https://nbodykit.readthedocs.io/>

<sup>7</sup><https://github.com/cosmodesi/pypower>

### 4.4.3 The clustering of eBOSS DR16 LRGs

Figure 4.5 and 4.6 show the power spectrum  $P_\ell(k)$  and correlation function  $\xi_\ell(r)$  multipoles for  $\ell = 0, 2, 4$  for the combined sample of BOSS DR12 and eBOSS DR16 luminous red galaxies and their respective EZMOCK catalogues. Figure 4.5 shows results from standard catalogues while Figure 4.6 displays results from reconstructed catalogues.

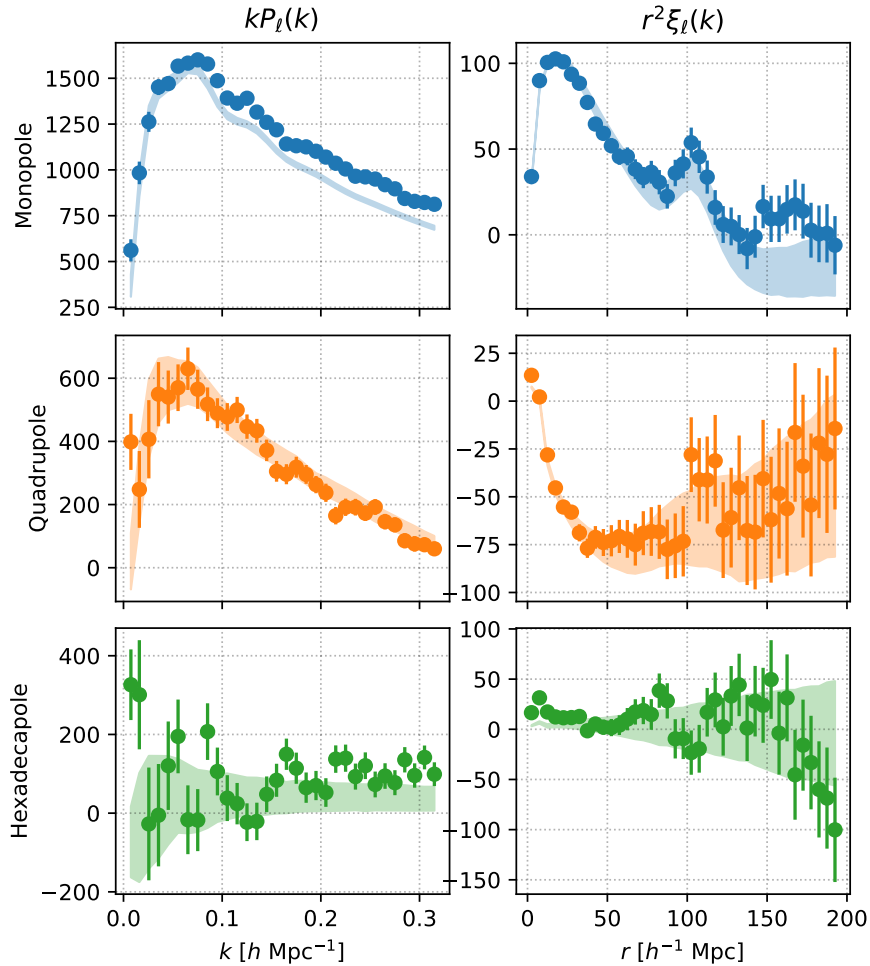


Figure 4.5: Pre-reconstruction multipoles of the two-point statistics for the combination of BOSS DR12 and eBOSS DR16 luminous red galaxies. Left panels contain the power spectrum multipoles (scaled by  $k$ ) and right panels the correlation function multipoles (scaled by  $r^2$ ). Points with errorbars are real data while shaded regions show the mean and standard deviation of 1000 realisations of EZMOCKS.

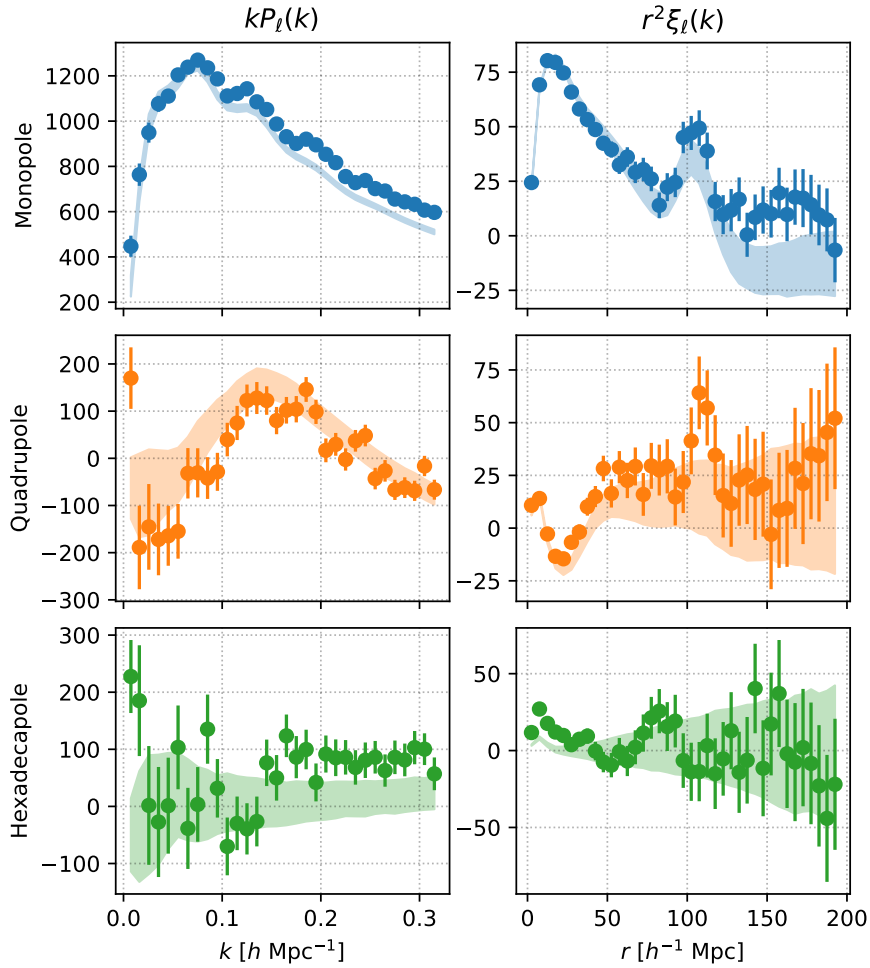


Figure 4.6: Same as Figure 4.5 but for reconstructed catalogues. We used the Zeldovich reconstruction method with removal of redshift-space distortions. The BAO features are more prominent and the quadrupole is significantly reduced compared to results with the standard catalogues.

The uncertainties on our measurements of  $P_\ell$  and  $\xi_\ell$  were derived by measuring the same statistics on the full sample of 1000 realisations of EZMOCKS. By reproducing with high fidelity the observational features and systematic effects, the covariance matrix obtained with mocks should account for the extra scatter induced by them. However on small scales the clustering of the mocks is not accurate compared to real data or to more realistic n-body simulations. Figure 4.7 shows the resulting covariance matrices normalised by the diagonal elements (correlation coefficients). We see how power spectra multipoles are generally less correlated than correlation function multipoles. Reconstruction also helps reducing these correlations. Also shown are the cross-covariance between Fourier space and configuration space measurements, which will be discussed in section 4.7. As expected, these two spaces are highly correlated since they originate from the same sample of galaxies and randoms.

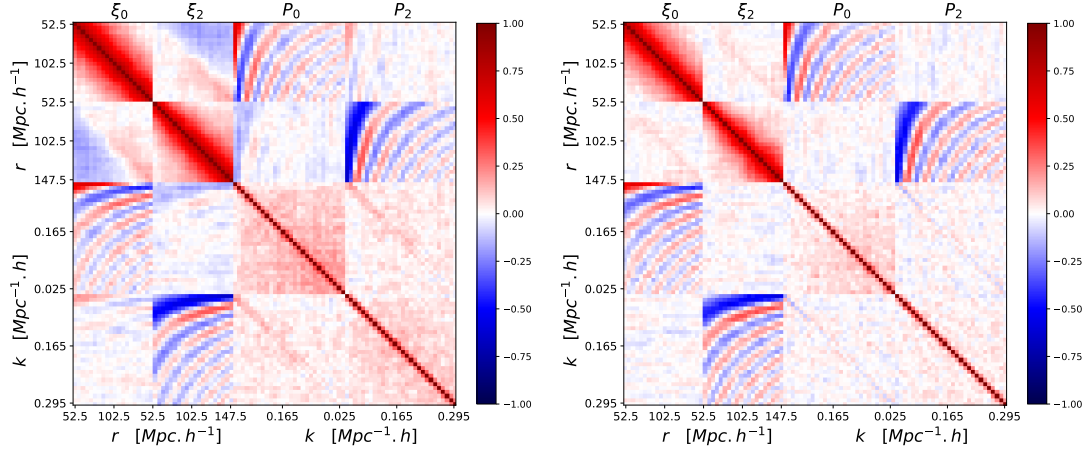


Figure 4.7: Correlation coefficients from covariance matrices obtained from 1000 measurements of power spectrum and correlation function multipoles,  $P_\ell$  and  $\xi_\ell$  respectively, from EZMOCKS reproducing the combined BOSS DR12 and eBOSS DR16 LRG sample. Left panel shows results from the standard catalogues while the right panel shows the results from Zeldovich reconstructed catalogues.

## 4.5 Baryon acoustic oscillations

The feature from baryon acoustic oscillations (BAO) is clearly visible as oscillations in the power spectrum multipoles and as a sharp peak in the correlation function multipoles (Figures 4.5 and 4.6). In this section I describe how we measure the BAO scale, which is used as a standard ruler in the study of the expansion of the Universe. The work is detailed further in Julian E Bautista et al. 2020; Gil-Marín et al. 2020.

The model used to fit BAO is based on the linear matter power spectrum with a simplified treatment of bias, redshift-space distortions and non-linearities. It is basically the same model as used in the BAO measurements from Ly $\alpha$  forests described in section 3.2.4 but without the treatment of metal absorption, high-column density systems and distortions which do not apply here. A linear bias and linear redshift-space distortions is assumed. The non-linearities that broaden the BAO peak are modelled by two Gaussian smoothing terms, one for radial separations and one for transverse separations. We also decompose the peak part from the smooth part of the model, scaling only the peak part by the dilation factors  $\alpha_{\parallel}$  and  $\alpha_{\perp}$ , defined in Eqs. 3.11 and 3.12. The fit is performed in the space of multipoles instead of fitting for the full two-point statistics. Smooth power-laws of separation are added with free amplitudes in order to marginalise any potential information coming from the smooth part of the correlation function. To account for the removal of redshift-space distortions after reconstruction, an empirical damping term is added to the model, such that the linear RSD term  $(1 + \beta\mu^2)$  becomes  $(1 + S(k)\beta\mu^2)$  where  $S(k) \equiv 1 - e^{-k^2\Sigma_{\text{rec}}^2/2}$  (Seo, Beutler, et al. 2016).

The methodology was tested with the sample of 1000 EZMOCKS and also an additional set of 84 NSERIES n-body simulations (section 4.3). In principle, BAO is a feature on large enough scales such that testing the method on approximate mocks is sufficient, although we also looked at results on more realistic n-body simulations. In order to understand potential biases

in best-fit BAO parameters, we fit for BAO on the average clustering of all available realisations for EZMOCKS and NSERIES mocks, effectively increasing the volume of the survey by a factor of 1000 and 84 respectively. Thanks to the large number of EZMOCKS, we were able to study the performance of our fitter statistically, by looking at the ensemble of 1000 individual BAO fits.

Figure 4.8 displays the results of fits to the mean clustering of mocks for catalogues pre- and post-reconstruction, also as a function of the fiducial choice for  $\Omega_m^{\text{fid}}$  used in converting distances to redshifts. First we notice how biases are much smaller for reconstructed catalogues than standard ones, likely thanks to a better modelling of non-linearities affecting the BAO peak which are reduced in the reconstructed case. Second, uncertainties of reconstructed results are reduced relative to pre-reconstruction catalogues, showing the good performance of the method to remove bulk motions. Third, there is a very weak dependency of our results with the choice of  $\Omega_m^{\text{fid}}$ , which is reassuring.

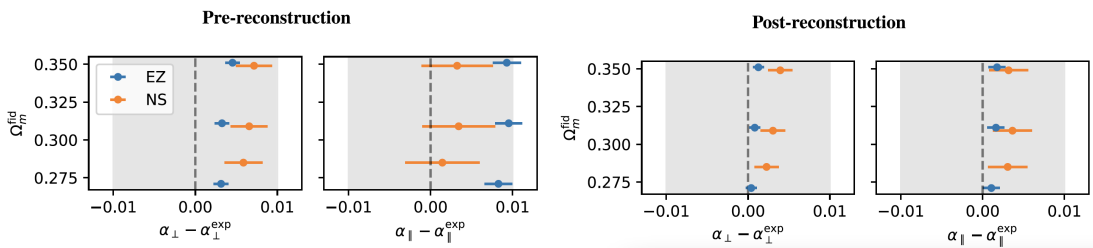


Figure 4.8: Impact of choice of fiducial cosmology in the recovered values of  $\alpha_{\parallel}$  and  $\alpha_{\perp}$  from BAO fits to the stacks of 1000 multipoles the EZMOCKS (blue) and 84 NSERIES mocks (orange), for pre- (left panels) and post-reconstruction (right panels). Associated error bars correspond to the uncertainty estimated from the mean of the mocks. The grey shaded areas correspond to 1 per cent shifts. For comparison, the uncertainty on real data is 1.9 per cent for  $\alpha_{\perp}$  and 2.6 per cent for  $\alpha_{\parallel}$  in the post-reconstruction case.

Another important test of our methodology consists in checking uncertainty estimation. With the sample of 1000 BAO measurements from mocks, we can study them statistically. Our uncertainties are derived by scanning the likelihood profile and finding the intervals where the parameters  $\alpha_{\perp}$  and  $\alpha_{\parallel}$  increase the  $\chi^2$  by unity<sup>8</sup> relative to its minimum. First, we compare the standard deviation of all best-fit values to the average uncertainty found in all 1000 mocks. If uncertainties are correctly estimated then these two numbers match. Second, we could look at the pull distribution of each parameter  $x_i$ , defined as  $Z_i \equiv (x_i - \bar{x}_i)/\sigma_{x_i}$ . If the uncertainties are well behaved and Gaussian, then we should obtain  $\bar{Z}_i = 0$  and  $\text{Var}(Z_i) = 1$ . Table 6 in Julian E Bautista et al. 2020 shows these statistics for BAO measurements. The results validate our methodology and we applied it to data.

Figure 4.9 shows the best-fit correlation function model and the BAO constraints for the eBOSS DR16 LRG sample. Converting the constraints in  $(\alpha_{\perp}, \alpha_{\parallel})$  into ratios of distances, we obtained:

$$\mathbf{D}_{\text{BAO}, \xi_\ell} = \begin{pmatrix} D_M/r_d \\ D_H/r_d \end{pmatrix} = \begin{pmatrix} 17.86 \pm 0.33 \\ 19.34 \pm 0.54 \end{pmatrix}, \quad (4.8)$$

which correspond to a BAO measurement at 1.9 per cent in the transverse direction and 2.8 per cent in the radial direction. Radial and transverse BAO measurements are correlated by

<sup>8</sup>In the case marginalised errors in one parameter. For two parameters, the 68 and 95% confidence intervals are defined by  $\Delta\chi^2 = 2.3, 5.9$  respectively.

-33% for this dataset. These are the best constraints obtained from galaxies at redshifts above 0.6.

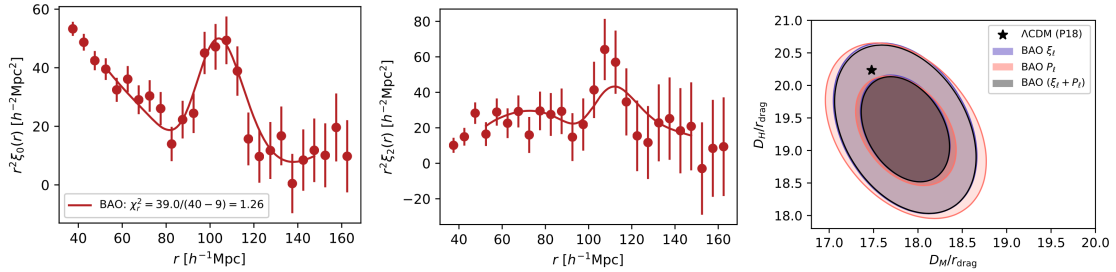


Figure 4.9: Two left panels show the best-fit model for the correlation function monopole and quadrupole for the reconstructed eBOSS LRG sample. The right panel shows the two-dimensional constraints on the distance to sound horizon ratios, for the configuration and Fourier space BAO analyses. The consensus BAO result is shown in grey. The star points to the prediction of a flat  $\Lambda$ CDM model with Planck 2018 best-fit parameters.

## 4.6 Redshift-space distortions

The analysis of redshift-space distortions (RSD) aims to measure the growth-rate of structures  $f$ , as introduced in section 1.5.6, by quantifying the anisotropies in the clustering of galaxies. As we seen before, assuming an incorrect fiducial cosmology when converting redshifts into distances also introduces anisotropies (the AP effect). Therefore in practice, an RSD analysis yields simultaneously the combination  $f(z)\sigma_8(z)$  and the distance ratios  $D_H(z)/r_{\text{drag}}, D_M(z)/r_{\text{drag}}$ .

The main differences with respect to the BAO analysis (see previous section) is that the information about anisotropies come from the full shape of the two-point statistics, not only the peak. This complicates the RSD analysis in that we need to have accurate models for the full shape of the clustering down to some scale, and we cannot add empirical terms to be marginalised over as we did in the BAO analysis. Due to non-linearities of matter clustering and galaxy bias, it is increasingly hard to model scales below those well described by linear theory. For these mildly non-linear scales, we need more advanced perturbation theory models. A huge variety of theoretical models have been developed in the past years (see F. Bernardeau et al. 2002 for a review).

In the analysis of eBOSS data, we used two types of models: the first one is based on regularised perturbation theory with second order bias and RSD correction terms (Taruya, Nishimichi, et al. 2010; Taruya, Francis Bernardeau, et al. 2012). We commonly refer to it as the *TNS model*. The second one is based on convolution Lagrangian perturbation theory with Gaussian streaming (Carlson et al. 2013; Wang et al. 2014). We refer to it as the *CLPT-GS model*. I implemented these models in python language in the package BAOPY<sup>9</sup>.

The TNS model is expressed as:

$$P_g(k, \mu_k) = D_{\text{FoG}}(k, \mu_k) [P_{g,\delta\delta}(k) + 2f\mu_k^2 P_{g,\delta\theta}(k) + f^2\mu_k^4 P_{\theta\theta}(k) + b_1^3 A(k, \mu_k, \beta) + b_1^4 B(k, \mu_k, \beta)], \quad (4.9)$$

<sup>9</sup><https://baopy.readthedocs.io/>

where  $b_1$  is the first order linear galaxy bias,  $\beta \equiv f/b_1$ ,  $(P_{g,\delta\delta}, P_{g,\delta\theta}, P_{\theta\theta})$  are the non-linear isotropic galaxy auto power spectrum, galaxy-velocity divergence cross power spectrum and the velocity divergence auto power spectrum, respectively, which are themselves functions of first and second order bias parameters. These functions are provided by the RegPT scheme, implemented in PYREGPT<sup>10</sup>. The functions  $A$  and  $B$  are the RSD correction terms. The function  $D_{\text{FoG}}$  can be either a Gaussian or a Lorentzian of  $k_{\parallel} = k\mu_k$  with characteristic scale  $\sigma_{\text{FoG}}$  corresponding to the velocity dispersion on small scales. This model is computed in Fourier space, but it can be Fourier transformed to obtain a model in configuration space.

The CLPT-GS model is uniquely defined in configuration space, and writes as:

$$1 + \xi_{g,s}(r_{\perp}, r_{\parallel}) = \int \frac{1}{\sqrt{2\pi [\sigma_{12}^2(r) + \sigma_{\text{FoG}}^2]}} [1 + \xi_g(r)] \exp \left\{ -\frac{[r_{\parallel} - y - \mu v_{12}(r)]^2}{2[\sigma_{12}^2(r) + \sigma_{\text{FoG}}^2]} \right\} dy \quad (4.10)$$

where  $\xi_g(r)$ ,  $v_{12}(r)$ , and  $\sigma_{12}(r)$  are obtained from CLPT and contains two bias terms. The dependency with  $f$  is via a scaling of the functions  $v_{12}, \sigma_{12}$  that are proportional to velocity. The integral corresponds to the convolution by velocities in the radial direction, characteristic of the Gaussian streaming formalism.

Both the TNS and CLPT-GS models had to be tested against n-body simulations. We were particularly interested in the scales of validity of these models for the case of the eBOSS LRG sample. Given the number of available realisations, we used the n-body suite of 84 realisations of NSERIES simulations produced for the BOSS CMASS sample. We fitted the average correlation function of these simulations and measured the parameters  $f\sigma_8, \alpha_{\perp}, \alpha_{\parallel}$ . Figure 4.10 presents the results compared to expected values for both TNS and CLPT-GS models. The shaded green area shows the fiducial choice to be used in the data.

---

<sup>10</sup><https://github.com/adematti/pyregpt>

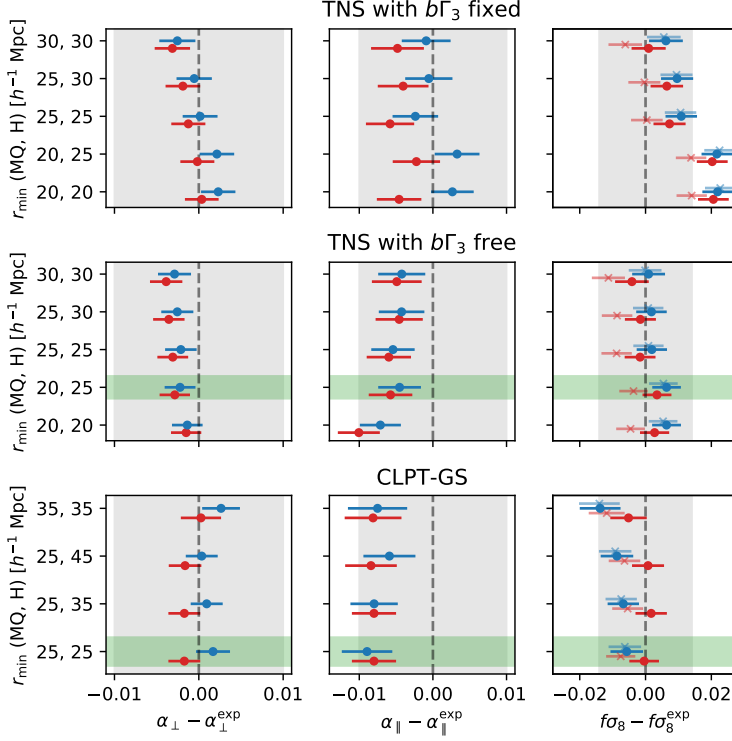


Figure 4.10: Biases in the measurement of  $f\sigma_8, \alpha_{\parallel}, \alpha_{\perp}$  obtained from full-shape fits to the average of 84 multipoles from the NSERIES mocks as a function of the separation range used. The y-axis displays the value of the minimal separation  $r_{\min}$  used in fits of the monopole, quadrupole (MQ) and hexadecapole (H). Top and mid rows display results for the TNS model when fixing or letting free the bias parameter  $b\Gamma_3$  respectively. Bottom row presents results for the CLPT-GS model. The blue circles correspond to the analysis using  $\Omega_m^{\text{fid}} = 0.286$  (the true value of simulations) while the red circles correspond to  $\Omega_m^{\text{fid}} = 0.31$ . The crosses in the  $f\sigma_8$  panels correspond to their values before the scaling of  $\sigma_8$  discussed in Figure 4.11. The gray shaded areas correspond to 1 per cent errors in  $\alpha_{\perp}, \alpha_{\parallel}$  and to 3 per cent in  $f\sigma_8$ . The green shaded area shows our choice for baseline analysis for TNS and CLPT-GS models.

Using the same simulations, we tested the dependency of our constraints to the choice of fiducial cosmology. Note that the fiducial cosmology enters twice in the modelling, first when converting redshifts to distances; second, when computing the linear matter power spectrum template  $P_m^{\text{lin}}(k)$ , used as main ingredient for both models. Figure 4.11 presents the results for three choices of fiducial cosmology. While for  $\alpha_{\perp}, \alpha_{\parallel}$  the biases or trends are negligible,  $f\sigma_8$  shows a strong dependency with  $\Omega_m^{\text{fid}}$ , shown as crosses in the figure. This dependency is mainly caused by the assumed  $\sigma_8$  value, that corresponds to the one derived from the fiducial  $P_m^{\text{lin}}(k)$  via Eq. 1.18. The resulting  $f$  of the fit is scaled by this  $\sigma_8$ . We can reduce this dependency by recomputing  $\sigma_8$  using  $R = 8\alpha h^{-1}\text{Mpc}$ , where  $\alpha \equiv \alpha_{\perp}^{(2/3)}\alpha_{\parallel}^{(1/3)}$  is the isotropic dilation factor obtained from the best-fit  $\alpha_{\perp}, \alpha_{\parallel}$ . In effect, this keeps the scale at which  $\sigma_8$  is fitted fixed relative to the data in units of  $h^{-1}\text{Mpc}$ , which only depends on  $\Omega_m^{\text{fid}}$ . This is an alternative approach to the recently proposed  $\sigma_{12}$  parametrisation (Sánchez

2020), where the radius of the top-hat function is set to  $R = 12$  Mpc (in units of Mpc) instead of  $R = 8 h^{-1}$  Mpc (in units of  $h^{-1}$  Mpc). The circles in the right panel of Figure 4.11 shows the results with the recomputed  $\sigma_8$  for each case, showing that this procedure indeed reduces the trend of  $f\sigma_8$  with  $\Omega_m^{\text{fid}}$ . This topic is also discussed in Appendix A of Alam, Aubert, et al. 2021.

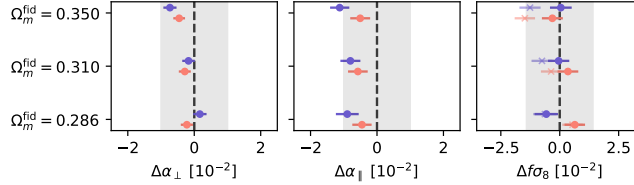


Figure 4.11: Biases in best-fit parameters for both CLPT-GS (blue) and TNS (red) models from fits to the average multipoles of 84 NSERIES mocks. Shaded grey areas show the equivalent of 1 per cent error for  $\alpha_{\perp}, \alpha_{\parallel}$  and 3 per cent for  $f\sigma_8$ . In the right panel, crosses indicate  $f\sigma_8$  values when  $\sigma_8$  is not recomputed as described in Section ???. The true cosmology of the mocks is  $\Omega_m = 0.286$ . For reference, the errors on our data sample are  $\sim 2, 3$  and 10 per cent for  $\alpha_{\perp}, \alpha_{\parallel}, f\sigma_8$  respectively.

After validating the model, we tested the impact of different halo occupation distribution (HOD) models and observational effects, both introduced in simulations. We found that none of these modifications introduces significant biases our constraints of  $(f\sigma_8, \alpha_{\perp}, \alpha_{\parallel})$ , though the shifts we observe were added as systematic uncertainties in quadrature to the statistical ones. Table 10 of Julian E Bautista et al. 2020 summarises the systematic errors which are assumed to be diagonal (no covariance between the three parameters) for simplicity. For our RSD analysis, systematic errors are about half of the statistical ones for  $f\sigma_8$  and slightly less for  $\alpha_{\perp}, \alpha_{\parallel}$ . In quadrature, final uncertainties increase by up to 20% due to systematic errors.

We also attempted to analyse our biases and uncertainties statistically with the set of 1000 EZMOCKS. However, an important caveat is that these mocks only solve approximatively the clustering, and therefore are not the better suited to test RSD fitting. We proceeded to fit the 1000 realisations and we compared the average uncertainty to the standard deviation of best-fit parameters among all mocks. These numbers agree sufficiently well, particularly for  $f\sigma_8$ . The pull distributions of each parameters do not point to any under/over estimation of uncertainties.

Figure 4.12 presents the best-fit TNS and CLPT-GS models to the correlation function multipoles of the eBOSS DR16 LRG sample. Both models are basically indistinguishable even though their are derived differently. The constraints are also similar between the two models, so we combined them into a single results by averaging their best-fit parameters and their covariances. Figure 4.13 show the final constraints on  $f\sigma_8$  and the distance ratios, compared to the same analysis in Fourier space. We also show the consensus result computed using the method by Sánchez et al. 2017, which assumes Gaussianity of each posterior distribution (see the next section for a further discussion). The final RSD constraints from the correlation function fits are:

$$\mathbf{D}_{\text{RSD}, \xi} = \begin{pmatrix} D_M/r_d \\ D_H/r_d \\ f\sigma_8 \end{pmatrix} = \begin{pmatrix} 17.42 \pm 0.40 \\ 20.46 \pm 0.70 \\ 0.460 \pm 0.050 \end{pmatrix} \quad (4.11)$$

which correspond to a 11% measurement of  $f\sigma_8$  at  $z_{\text{eff}} = 0.7$ . This uncertainty is slightly

reduced when combining with the Fourier space results and with BAO results from the previous section. The combination between Fourier and configuration space results will be discussed in the following section.

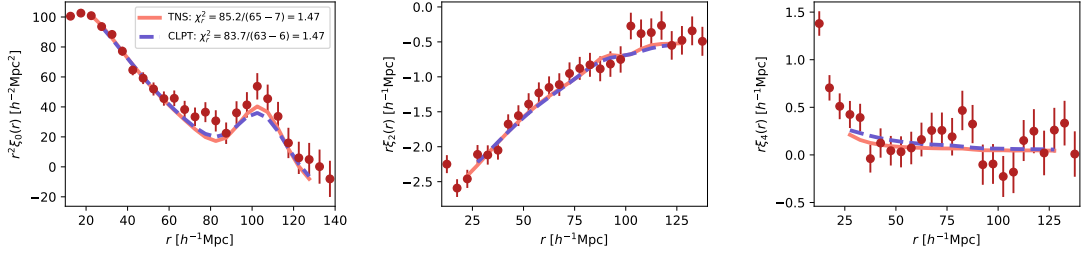


Figure 4.12: Best-fits models of redshift-space distortions (RSD) to the eBOSS DR16 LRG multipoles. Left, mid and right panel display mono, quad and hexadecapole, respectively. Note that only the monopole is scaled by  $r^2$  while the others are scaled by  $r$ . The CLPT-GS model is shown by the blue dashed line while the TNS model is shown by the red solid line.

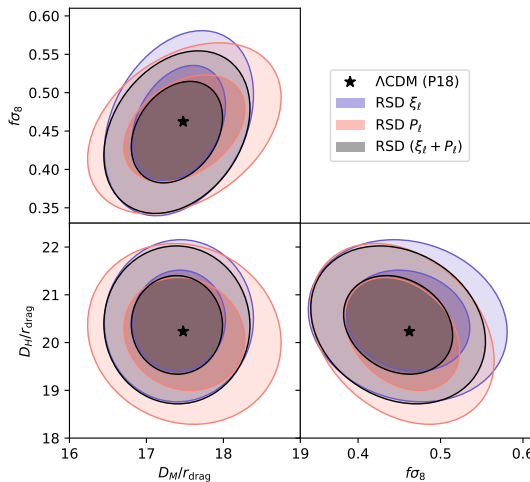


Figure 4.13: Constraints on  $D_M/r_d$ ,  $D_H/r_d$  and  $f\sigma_8$  at  $z_{\text{eff}} = 0.7$  from the full-shape RSD analysis of the completed eBOSS LRG sample. Contours show 68 and 95 per cent confidence regions for the analyses in configuration space (blue), Fourier space (red) and the combined (grey). The expected values in a flat  $\Lambda$ CDM model with best-fit parameters from Planck 2018 results is indicated as a black star.

## 4.7 Joint clustering analysis in Fourier and Configuration space

From the same catalogue of angular positions and redshifts, we can perform two different clustering analyses: one in Fourier space (FS) and the other in Configuration space (CS). How to define a consensus result from both analysis which might yield slightly different results? In this section I expose the work lead by my PhD students Tyann Dumerchat and Vincenzo Aronica on how to combine BAO and RSD constraints from both spaces into a single consensus

result.

Sánchez et al. 2017 proposed a method to combine two correlated Gaussian posteriors into a single one. I refer to it as the Gaussian approximation (GA) method. The GA method was used in BOSS (Alam, Ata, et al. 2017) and it was slightly improved in eBOSS (Julian E Bautista et al. 2020). The main idea is that we want to combine a set of vectors containing the best-fit parameters of different analysis (and their respective error matrix) into a single vector of parameters and a single error matrix. For example in BOSS and eBOSS, we aimed at combining the vectors  $\vec{p} \equiv f\sigma_8, \alpha_{\perp}, \alpha_{\parallel}$  obtained from FS and CS analyses. The GA method uses an estimate the correlations between  $\vec{p}_{\text{FS}}$  and  $\vec{p}_{\text{CS}}$ , and built a large covariance matrix used to combine the vectors and error matrices. Currently the best method to obtain these correlations between FS and CS results is using mock catalogues. This provides with an estimate of a sort of “ensemble averaged” correlations (though limited by the number of realisations). However, the real data is a single realisation of the ensemble, and the correlations between FS and CS are also susceptible to fluctuate, just as the individual parameters and their uncertainties. In Julian E Bautista et al. 2020 we developed a method to account for this fact, where we adjust the correlations for each realisation based on the vectors  $\vec{p}$  and their error matrices of that particular realisation.

In **dumerchatJoint2022**, we developed an analysis where we fit jointly the correlation function and power spectrum while accounting for their covariance. I refer to it as the joint space (JS) method. The covariance is built at the multipole level, using a set of mock catalogues. Figure 4.7 shows the correlation coefficients of CS and FS multipoles, including the cross-correlation terms. The wiggles observed in the cross-correlation terms can be simply explained by the fact that CS and FS are related via Hankel transforms (see Appendix A of **dumerchatJoint2022** for an explicit derivation). We tested and validated this framework on the BAO analysis of the eBOSS LRG sample (section 4.5) where we fit for a single  $\alpha_{\perp}$  and  $\alpha_{\parallel}$ , though amplitudes of power-laws are independent for each space. The main advantage of the JS method is that we do not assume Gaussian posteriors at the parameter level, only at the multipole level when fitting our model (which is quite common assumption). The posteriors on the resulting  $(\alpha_{\perp}, \alpha_{\parallel})$  can also be non-Gaussian. Figure 4.14 displays few examples from BAO fits to mock realisations where the CS and FS posteriors are Gaussian (left) or non-Gaussian (right panels), and the resulting combination from GA and JS methods. For the non-Gaussian cases, the GA method fails to correctly describe the posterior, underestimating uncertainties.

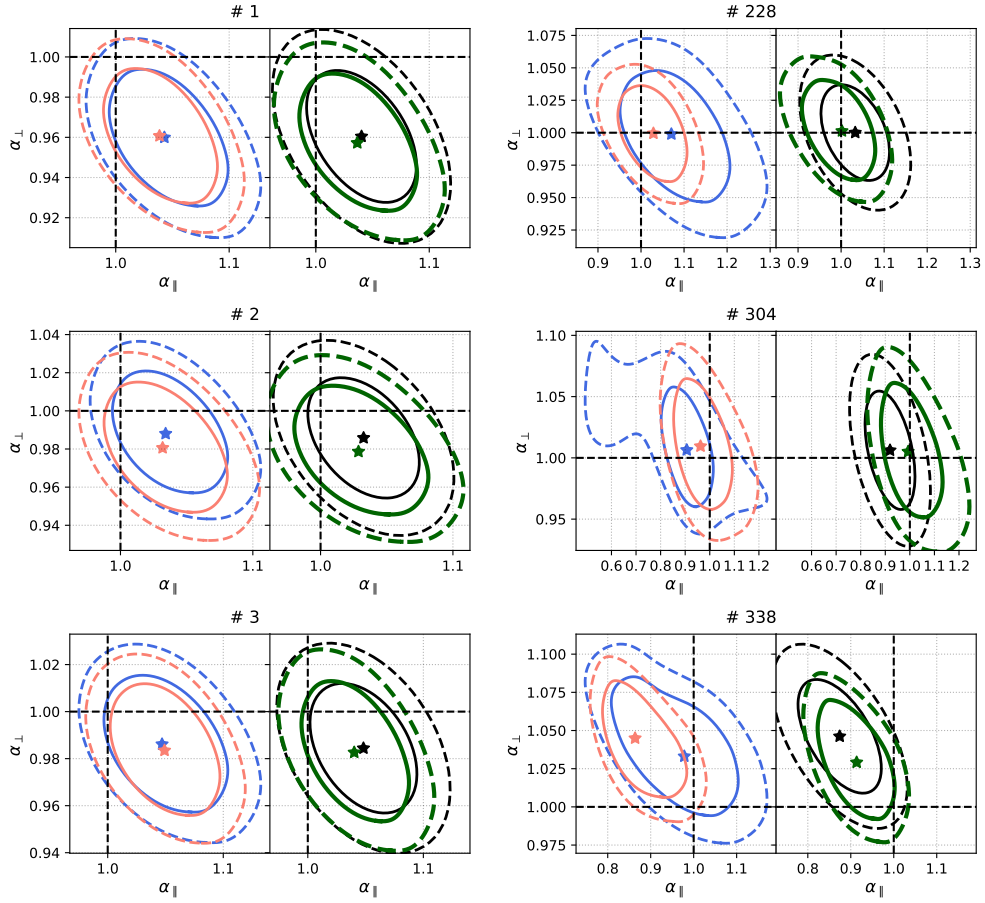


Figure 4.14: Posteriors on the BAO fits of some EZMOOCKS realisations. We display cases where contours found in configuration or Fourier space are Gaussian (left) and non Gaussian (right). Red contours are for Fourier space (FS), blue for configuration space (CS), black for the Gaussian approximation (GA) and green for the joint space (JS) fits. The expected value is the intersection of the dotted black lines, and the best fit values are described by a star for the JS and GA methods. We can see how the JS method yields better combined results that are not necessarily Gaussian. Extracted from **dumerchatJoint2022**.

Vincenzo Aronica is currently working on the application of joint space analysis for the case of redshift-space distortions (RSD). He implemented the TNS model (section 4.4.3) in Fourier and configuration space in the BAOPY package. The tests on the suite of 84 realisations of NSERIES n-body simulations are promising, though there are some subtleties to solve related to the relative normalisation (or linear bias) amplitudes between FS and CS. Currently we use the same values of biases for both space, in addition to  $\alpha_{\perp}, \alpha_{\parallel}, f\sigma_8$ . Vincenzo will recompute power spectra for a given set of mock catalogues using a consistent normalisation and window function calculations provided by PYPOWER.

The work on BAO and RSD joint fits in Fourier and configuration space will be discussed and hopefully applied to the analysis of DESI data.

## 4.8 Cross-correlation with radio surveys

The study of large-scale structures will soon be improved thanks to observations of the distribution of neutral hydrogen (HI) via the emission of photons from the 21cm hyperfine transition of the electron. Future 21cm surveys such as the Square Kilometer Array (SKA) will be able to observe the Universe with intensity mapping up to redshifts of 3, opening an alternate window to that provided by spectroscopic surveys. The term *intensity mapping* refers to the fact that we measure the integrated flux from unresolved sources at a given location in space.

During my postdoctoral stay at the University of Portsmouth, I contributed to the study of a currently available 21cm survey produced by the Green Bank Telescope (GBT). I was particularly interested in the study of cross-correlations between the 21cm observed by GBT and the eBOSS galaxies observed in the same volume. With the cross-correlation function we could infer the product of the average neutral hydrogen fraction  $\Omega_{\text{HI}}$  at redshift  $z_{\text{eff}} = 0.8$  with the bias of HI  $b_{\text{HI}}$ . These parameters are important ingredients for models of clustering of the 21cm emission. I overview the main findings of this work in this section but further details are described in Wolz et al. 2022.

The use of 21cm intensity mapping to measure the large-scale structures has been extensively studied theoretically (Bharadwaj et al. 2001; Battye et al. 2004; McQuinn et al. 2006; Chang et al. 2008) and with simulations (Mesinger et al. 2011; Villaescusa-Navarro et al. 2018 and references therein). On large scales, 21cm flux fluctuations trace those of dark matter density, while on smaller scales the physics of the gas and its connection to halos complexifies the modelling. Including redshift-space distortions, a linear model for the 21cm power spectrum is essentially the same as the linear model for galaxy clustering. In Villaescusa-Navarro et al. 2018, an extensive study using the IllustrisTNG n-body hydro simulation quantified several ingredients commonly used in more complex models of the 21cm power spectra, such as the HI content of halos, the HI probability density function, the HI bias with respect to matter and others.

The data sets we used in our study were the eBOSS luminous red galaxy (LRG) and emission line galaxy (ELG) samples in one hand, and the Green Bank Telescope (GBT) 21cm maps in the other hand. The eBOSS LRG sample is already described in section 4.1 while the ELG sample is described in Anand Raichoor et al. 2020. The GBT maps are observations of a  $100 \text{ deg}^2$  patch of sky at frequencies from 700 to 900 MHz divided into 256 channels, corresponding to HI emission between  $0.6 < z < 1.0$ , perfectly overlapping with our galaxy samples in area and redshift. The angular resolution of HI observations varies from  $0.31 \text{ deg}$  at 700 MHz to  $0.25 \text{ deg}$  at 900 MHz. In order to reduce the impact of varying PSF, all channels are convolved by an artificial beam of  $0.44 \text{ deg}$ . The maps we used are an extension to those produced by Masui et al. 2013, including extra scans which increase the area and depth. The raw data is contaminated by radio frequency interference and some channels are therefore masked. Foregrounds are removed with a technique named *FastICA*, which stands for fast independent component analysis. I was provided several maps with different number of foreground components removed. Once the final area of GBT maps was fixed, I cut the eBOSS LRG and ELG samples to the same area. Figure 4.15 shows a redshift slice (or one channel) of the foreground-cleaned GBT HI map and the LRG and ELG angular distribution in the same patch of sky.

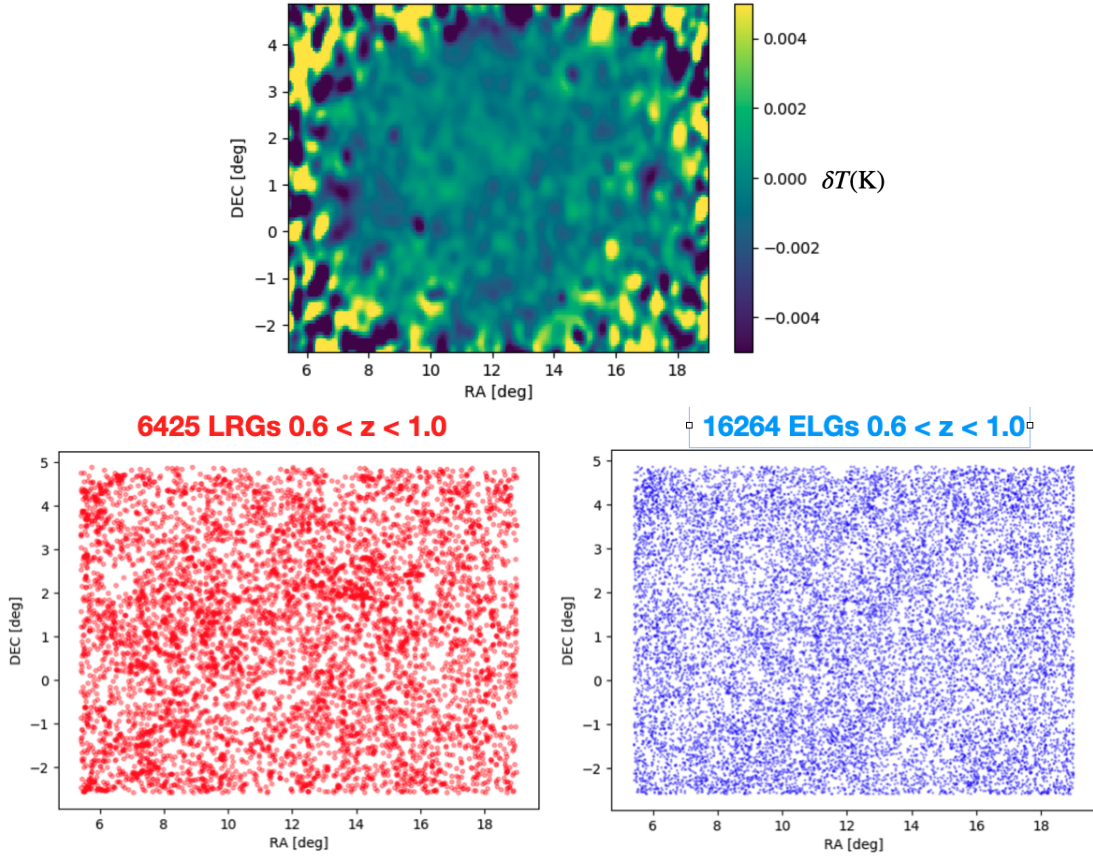


Figure 4.15: Top panel: a redshift slice of the 21cm HI map from the Green Bank Telescope after foreground removal. Bottom panels: the angular distribution of all eBOSS LRGs and ELGs falling in the same sky area.

The cross-correlations between eBOSS galaxies and 21cm temperature maps was computed in Fourier space by Wolz et al. 2022 and in configuration space by me. The cross-correlation estimator I used is the same used for the quasar- $\text{Ly}\alpha$  forest cross-correlation described in section 3.2.2, which assumes that galaxies (in this case) are shot-noise dominated and that voxels of the 21cm map are independent. These assumptions are not quite valid for our sample but I left further developments for future work. For instance, one could perform the study of cross-correlations with a maximum likelihood method (see e.g. section 5.3) or in Fourier space but correctly accounting for the convolution by the window function of these surveys, which was not explicitly done in Wolz et al. 2022.

Figure 4.16 displays the monopoles and quadrupoles of the cross-correlation function between 21cm temperature fluctuations and eBOSS galaxies. Both ELG and LRG show non-zero correlations with the temperature maps that extend to cosmological scales. In particular, we clearly see a non-zero quadrupole, which was measured for the first time in this analysis. The covariance matrix of the multipoles was computed with the jackknife technique, using 96 independent subsets of the data. Due to the estimator I used, neighbouring separation bins in the monopole are strongly correlated.

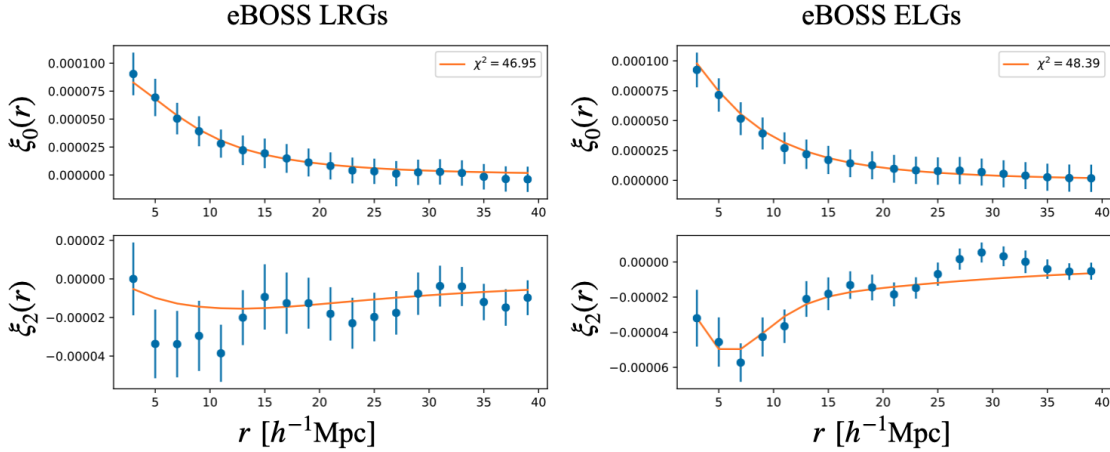


Figure 4.16: Cross-correlation function multipoles between 21cm temperature fluctuation maps from the Green Bank Telescope and the eBOSS samples of Luminous Red Galaxies (left) and Emission Line Galaxies (right). Uncertainties are computed with jackknife resampling and solid lines correspond to the best-fit models.

I attempted to fit the temperature-galaxy cross-correlation with the following model:

$$P(k, \mu) = \frac{b_{\text{gal}} b_{\text{HI}} \bar{T}_{\text{HI}}}{(1 + k^2 \mu^2 \Sigma_{\text{FoG}}^2)^2} (1 + \beta_{\text{gal}} \mu^2) (1 + \beta_{\text{HI}} \mu^2) P_{\text{lin}}(k) e^{-k^2 R_{\text{beam}}^2 (1 - \mu^2)/2} \quad (4.12)$$

which includes a term for Fingers-of-God with dispersion  $\Sigma_{\text{FoG}}$ , and a damping in the transverse (angular) direction to account for the effect of the beam of the GBT instrument, with characteristic scale  $R_{\text{beam}}$ . The solid lines in Figure 4.16 show the best-fit models, which have in total 6 free parameters. The  $\chi^2$  values are also shown in the figure, which correspond to 30 data points (24 degrees of freedom). The fits are generally well behaved. I do not show values for the best-fit parameters and their uncertainties because of the caveats I mentioned before related to the estimator and the covariance matrices. Also at the time of my analysis, we did not have mock catalogues to test my methodology.

Wolz et al. 2022 proceeded with the analysis of the cross power spectrum monopole and fitted for the amplitude of the signal, after testing our methods on mock catalogues. Using different scale ranges, we obtained constraints on the combination  $\Omega_{\text{HI}} b_{\text{HI}} r$  at  $z_{\text{eff}} = 0.8$ , where  $r$  is an empirical cross-correlation term that depends on the galaxy sample. Table 1 of Wolz et al. 2022 summarises results. For instance, for conservative choices for the analysis, we find  $\Omega_{\text{HI}} b_{\text{HI}} r = (0.48 \pm 0.12) \times 10^{-3}$  for GBT x ELGs and  $(0.38 \pm 0.12) \times 10^{-3}$  for GBT x LRGs, corresponding to 5 and  $4.2\sigma$  detections respectively.

This work is on the pathway for precision measurements with future 21cm surveys such as SKA (Square Kilometre Array Cosmology Science Working Group et al. 2020).

# 5 The low-redshift Universe and its velocities

## Contents

5.1 Measuring peculiar velocities . . . . .	69
5.2 Combining velocities with densities . . . . .	69
5.3 Maximum likelihood method . . . . .	69
5.4 Testing general relativity with velocities . . . . .	69

At low redshifts, below 0.1, peculiar velocities can be directly measured and their statistical properties can provide more information about gravity on large scales.

### 5.1 Measuring peculiar velocities

### 5.2 Combining velocities with densities

### 5.3 Maximum likelihood method

### 5.4 Testing general relativity with velocities

# Conclusion

Lorem ipsum dolor sit amet, consectetuer adipiscing elit. Ut purus elit, vestibulum ut, placerat ac, adipiscing vitae, felis. Curabitur dictum gravida mauris. Nam arcu libero, nonummy eget, consectetuer id, vulputate a, magna. Donec vehicula augue eu neque. Pellentesque habitant morbi tristique senectus et netus et malesuada fames ac turpis egestas. Mauris ut leo. Cras viverra metus rhoncus sem. Nulla et lectus vestibulum urna fringilla ultrices. Phasellus eu tellus sit amet tortor gravida placerat. Integer sapien est, iaculis in, pretium quis, viverra ac, nunc. Praesent eget sem vel leo ultrices bibendum. Aenean faucibus. Morbi dolor nulla, malesuada eu, pulvinar at, mollis ac, nulla. Curabitur auctor semper nulla. Donec varius orci eget risus. Duis nibh mi, congue eu, accumsan eleifend, sagittis quis, diam. Duis eget orci sit amet orci dignissim rutrum.

Nam dui ligula, fringilla a, euismod sodales, sollicitudin vel, wisi. Morbi auctor lorem non justo. Nam lacus libero, pretium at, lobortis vitae, ultricies et, tellus. Donec aliquet, tortor sed accumsan bibendum, erat ligula aliquet magna, vitae ornare odio metus a mi. Morbi ac orci et nisl hendrerit mollis. Suspendisse ut massa. Cras nec ante. Pellentesque a nulla. Cum sociis natoque penatibus et magnis dis parturient montes, nascetur ridiculus mus. Aliquam tincidunt urna. Nulla ullamcorper vestibulum turpis. Pellentesque cursus luctus mauris.

# Bibliography

- [Abb+17] B. P. Abbott et al. “A Gravitational-Wave Standard Siren Measurement of the Hubble Constant”. In: *Nature* 551.7678 (7678 2017), pp. 85–88. DOI: [10.1038/nature24471](https://doi.org/10.1038/nature24471) (cit. on p. 17).
- [Ahu+20] Romina Ahumada et al. “The 16th Data Release of the Sloan Digital Sky Surveys: First Release from the APOGEE-2 Southern Survey and Full Release of eBOSS Spectra”. In: *The Astrophysical Journal Supplement Series* 249 (1, 2020), p. 3. DOI: [10.3847/1538-4365/ab929e](https://doi.org/10.3847/1538-4365/ab929e) (cit. on p. 26).
- [Aio+20] Simone Aiola et al. “The Atacama Cosmology Telescope: DR4 Maps and Cosmological Parameters”. In: *Journal of Cosmology and Astroparticle Physics* 2020.12 (30, 2020), pp. 047–047. DOI: [10.1088/1475-7516/2020/12/047](https://doi.org/10.1088/1475-7516/2020/12/047) (cit. on p. 21).
- [Ala+17] Shadab Alam, Metin Ata, Stephen Bailey, Florian Beutler, Dmitry Bizyaev, Jonathan A. Blazek, Adam S. Bolton, Joel R. Brownstein, Angela Burden, Chia-Hsun Chuang, Johan Comparat, Antonio J. Cuesta, Kyle S. Dawson, Daniel J. Eisenstein, Stephanie Escoffier, Héctor Gil-Marín, Jan Niklas Grieb, Nick Hand, Shirley Ho, Karen Kinemuchi, David Kirkby, Francisco Kitaura, Elena Malanushenko, Viktor Malanushenko, Claudia Maraston, Cameron K. McBride, Robert C. Nichol, Matthew D. Olmstead, Daniel Oravetz, Nikhil Padmanabhan, Nathalie Palanque-Delabrouille, Kaike Pan, Marcos Pellejero-Ibanez, Will J. Percival, Patrick Petitjean, Francisco Prada, Adrian M. Price-Whelan, Beth A. Reid, Sergio A. Rodríguez-Torres, Natalie A. Roe, Ashley J. Ross, Nicholas P. Ross, Graziano Rossi, Jose Alberto Rubiño-Martín, Shun Saito, Salvador Salazar-Albornoz, Lado Samushia, Ariel G. Sánchez, Siddharth Satpathy, David J. Schlegel, Donald P. Schneider, Claudia G. Scóccola, Hee-Jong Seo, Erin S. Sheldon, Audrey Simmons, Anže Slosar, Michael A. Strauss, Molly E. C. Swanson, Daniel Thomas, Jeremy L. Tinker, Rita Tojeiro, Mariana Vargas Magaña, Jose Alberto Vazquez, Licia Verde, David A. Wake, Yuting Wang, David H. Weinberg, Martin White, W. Michael Wood-Vasey, Christophe Yèche, Idit Zehavi, Zhongxu Zhai, and Gong-Bo Zhao. “The Clustering of Galaxies in the Completed SDSS-III Baryon Oscillation Spectroscopic Survey: Cosmological Analysis of the DR12 Galaxy Sample”. In: *Monthly Notices of the Royal Astronomical Society* 470 (1, 2017), pp. 2617–2652. DOI: [10.1093/mnras/stx721](https://doi.org/10.1093/mnras/stx721) (cit. on pp. 22, 64).
- [Ala+21] Shadab Alam, Marie Aubert, Santiago Avila, Christophe Balland, Julian E. Bautista, Matthew A. Bershadsky, Dmitry Bizyaev, Michael R. Blanton, Adam S. Bolton, Jo Bovy, Jonathan Brinkmann, Joel R. Brownstein, Etienne Burtin, Solène Chabanier, Michael J. Chapman, Peter Doohyun Choi, Chia-Hsun Chuang, Johan Comparat, Marie-Claude Cousinou, Andrei Cuceu, Kyle S. Dawson, Sylvain de la Torre, Arnaud de Mattia, Victoria de Sainte Agathe, Hélion du Mas des Bourboux, Stephanie Escoffier, Thomas Etourneau, James Farr, Andreu Font-Ribera, Peter M. Frinchaboy, Sébastien Fromenteau, Héctor Gil-Marín, Jean-Marc Le Goff, Alma X. Gonzalez-Morales, Violeta Gonzalez-Perez, Kathleen Grabowski, Julien Guy,

- Adam J. Hawken, Jiamin Hou, Hui Kong, James Parker, Mark Klaene, Jean-Paul Kneib, Sicheng Lin, Daniel Long, Brad W. Lyke, Axel de la Macorra, Paul Martini, Karen Masters, Faizan G. Mohammad, Jeongin Moon, Eva-Maria Mueller, Andrea Muñoz-Gutiérrez, Adam D. Myers, Seshadri Nadathur, Richard Neveux, Jeffrey A. Newman, Pasquier Noterdaeme, Audrey Oravetz, Daniel Oravetz, Nathalie Palanque-Delabrouille, Kaike Pan, Romain Paviot, Will J. Percival, Ignasi Pérez-Ràfols, Patrick Petitjean, Matthew M. Pieri, Abhishek Prakash, Anand Raichoor, Corentin Ravoux, Mehdi Rezaie, James Rich, Ashley J. Ross, Graziano Rossi, Rossana Ruggeri, Vanina Ruhlmann-Kleider, Ariel G. Sánchez, F. Javier Sánchez, José R. Sánchez-Gallego, Conor Sayres, Donald P. Schneider, Hee-Jong Seo, Arman Shafieloo, Anže Slosar, Alex Smith, Julianna Stermer, Amelie Tamone, Jeremy L. Tinker, Rita Tojeiro, Mariana Vargas-Magaña, Andrei Variu, Yuting Wang, Benjamin A. Weaver, Anne-Marie Weijmans, Christophe Yèche, Pauline Zarrouk, Cheng Zhao, Gong-Bo Zhao, and Zheng Zheng. “Completed SDSS-IV Extended Baryon Oscillation Spectroscopic Survey: Cosmological Implications from Two Decades of Spectroscopic Surveys at the Apache Point Observatory”. In: *Physical Review D* 103.8 (28, 2021), p. 083533. DOI: [10.1103/PhysRevD.103.083533](https://doi.org/10.1103/PhysRevD.103.083533) (cit. on pp. 20, 22, 62).
- [AH22] Raul E. Angulo and Oliver Hahn. “Large-Scale Dark Matter Simulations”. In: *Living Reviews in Computational Astrophysics* 8 (1, 2022), p. 1. DOI: [10.1007/s41115-021-00013-z](https://doi.org/10.1007/s41115-021-00013-z) (cit. on p. 52).
- [Ave+21] Erik Aver, Danielle A. Berg, Keith A. Olive, Richard W. Pogge, John J. Salzer, and Evan D. Skillman. “Improving Helium Abundance Determinations with Leo P as a Case Study”. In: *Journal of Cosmology and Astroparticle Physics* 2021.03 (1, 2021), p. 027. DOI: [10.1088/1475-7516/2021/03/027](https://doi.org/10.1088/1475-7516/2021/03/027) (cit. on p. 19).
- [Ayl+17] K. Aylor, Z. Hou, L. Knox, K. T. Story, B. A. Benson, L. E. Bleem, J. E. Carlstrom, C. L. Chang, H.-M. Cho, R. Chown, T. M. Crawford, A. T. Crites, T. de Haan, M. A. Dobbs, W. B. Everett, E. M. George, N. W. Halverson, N. L. Harrington, G. P. Holder, W. L. Holzapfel, J. D. Hrubes, R. Keisler, A. T. Lee, E. M. Leitch, D. Luong-Van, D. P. Marrone, J. J. McMahon, S. S. Meyer, M. Millea, L. M. Mocanu, J. J. Mohr, T. Natoli, Y. Omori, S. Padin, C. Pryke, C. L. Reichardt, J. E. Ruhl, J. T. Sayre, K. K. Saffer, E. Shirokoff, Z. Staniszewski, A. A. Stark, K. Vanderlinde, J. D. Vieira, and R. Williamson. “A Comparison of Cosmological Parameters Determined from CMB Temperature Power Spectra from the South Pole Telescope and the Planck Satellite”. In: *The Astrophysical Journal* 850.1 (21, 2017), p. 101. DOI: [10.3847/1538-4357/aa947b](https://doi.org/10.3847/1538-4357/aa947b) (cit. on p. 21).
- [Bal+00] A. Balbi, P. Ade, J. Bock, J. Borrill, A. Boscaleri, P. De Bernardis, P. G. Ferreira, S. Hanany, V. Hristov, A. H. Jaffe, A. T. Lee, S. Oh, E. Pascale, B. Rabii, P. L. Richards, G. F. Smoot, R. Stompor, C. D. Winant, and J. H. P. Wu. “Constraints on Cosmological Parameters from MAXIMA-1”. In: *The Astrophysical Journal* 545 (1, 2000), pp. L1–L4. DOI: [10.1086/317323](https://doi.org/10.1086/317323) (cit. on p. 9).
- [Bal+21] L. Balkenhol et al. “Constraints on  $\Lambda$ CDM Extensions from the SPT-3G 2018 EE and TE Power Spectra”. In: *Physical Review D* 104.8 (4, 2021), p. 083509. DOI: [10.1103/PhysRevD.104.083509](https://doi.org/10.1103/PhysRevD.104.083509) (cit. on p. 21).

- [BDW04] Richard A. Battye, Rod D. Davies, and Jochen Weller. “Neutral Hydrogen Surveys for High-Redshift Galaxy Clusters and Protoclusters”. In: *Monthly Notices of the Royal Astronomical Society* 355 (1, 2004), pp. 1339–1347. DOI: [10.1111/j.1365-2966.2004.08416.x](https://doi.org/10.1111/j.1365-2966.2004.08416.x) (cit. on p. 66).
- [Bau+20] Julian E Bautista, Romain Paviot, Mariana Vargas Magaña, Sylvain de la Torre, Sébastien Fromenteau, Hector Gil-Marín, Ashley J Ross, Etienne Burtin, Kyle S Dawson, Jiamin Hou, Jean-Paul Kneib, Arnaud de Mattia, Will J Percival, Graziano Rossi, Rita Tojeiro, Cheng Zhao, Gong-Bo Zhao, Shadab Alam, Joel Brownstein, Michael J Chapman, Peter D Choi, Chia-Hsun Chuang, Stéphanie Escoffier, Axel de la Macorra, Hélion du Mas des Bourboux, Faizan G Mohammad, Jeongin Moon, Eva-Maria Müller, Seshadri Nadathur, Jeffrey A Newman, Donald Schneider, Hee-Jong Seo, and Yuting Wang. “The Completed SDSS-IV Extended Baryon Oscillation Spectroscopic Survey: Measurement of the BAO and Growth Rate of Structure of the Luminous Red Galaxy Sample from the Anisotropic Correlation Function between Redshifts 0.6 and 1”. In: *Monthly Notices of the Royal Astronomical Society* 500.1 (3, 2020), pp. 736–762. DOI: [10.1093/mnras/staa2800](https://doi.org/10.1093/mnras/staa2800) (cit. on pp. 22, 45, 57, 58, 62, 64).
- [Bau+17] Julian E. Bautista, Nicolás G. Busca, Julien Guy, James Rich, Michael Blomqvist, Hélion du Mas des Bourboux, Matthew M. Pieri, Andreu Font-Ribera, Stephen Bailey, Timothée Delubac, David Kirkby, Jean-Marc Le Goff, Daniel Margala, Anže Slosar, Jose Alberto Vazquez, Joel R. Brownstein, Kyle S. Dawson, Daniel J. Eisenstein, Jordi Miralda-Escudé, Pasquier Noterdaeme, Nathalie Palanque-Delabrouille, Isabelle Pâris, Patrick Petitjean, Nicholas P. Ross, Donald P. Schneider, David H. Weinberg, and Christophe Yèche. “Measurement of Baryon Acoustic Oscillation Correlations at  $z = 2.3$  with SDSS DR12 Ly $\alpha$ -Forests”. In: *Astronomy and Astrophysics* 603 (1, 2017), A12. DOI: [10.1051/0004-6361/201730533](https://doi.org/10.1051/0004-6361/201730533) (cit. on pp. 27, 31, 34, 35).
- [Bau+18] Julian E. Bautista, Mariana Vargas-Magaña, Kyle S. Dawson, Will J. Percival, Jonathan Brinkmann, Joel Brownstein, Benjamin Camacho, Johan Comparat, Hector Gil-Marín, Eva-Maria Mueller, Jeffrey A. Newman, Abhishek Prakash, Ashley J. Ross, Donald P. Schneider, Hee-Jong Seo, Jeremy Tinker, Rita Tojeiro, Zhongxu Zhai, and Gong-Bo Zhao. “The SDSS-IV Extended Baryon Oscillation Spectroscopic Survey: Baryon Acoustic Oscillations at Redshift of 0.72 with the DR14 Luminous Red Galaxy Sample”. In: *The Astrophysical Journal* 863.1 (2018), p. 110. DOI: [10.3847/1538-4357/aacea5](https://doi.org/10.3847/1538-4357/aacea5) (cit. on pp. 45, 49).
- [Bec+13] George D. Becker, Paul C. Hewett, Gábor Worseck, and J. Xavier Prochaska. “A Refined Measurement of the Mean Transmitted Flux in the Ly-alpha Forest over  $2 < z < 5$  Using Composite Quasar Spectra”. In: *Monthly Notices of the Royal Astronomical Society* 430 (1, 2013), pp. 2067–2081. DOI: [10.1093/mnras/stt031](https://doi.org/10.1093/mnras/stt031) (cit. on p. 32).
- [Ber+02] F. Bernardeau, S. Colombi, E. Gaztanaga, and R. Scoccimarro. “Large-Scale Structure of the Universe and Cosmological Perturbation Theory”. In: *Physics Reports* 367.1-3 (2002), pp. 1–248. DOI: [10.1016/S0370-1573\(02\)00135-7](https://doi.org/10.1016/S0370-1573(02)00135-7) (cit. on pp. 51, 59).

## Bibliography

- [Beu+12] Florian Beutler, Chris Blake, Matthew Colless, D. Heath Jones, Lister Staveley-Smith, Gregory B. Poole, Lachlan Campbell, Quentin Parker, Will Saunders, and Fred Watson. “The 6dF Galaxy Survey: z \approx 0 Measurement of the Growth Rate and Sigma\_8”. In: *Monthly Notices of the Royal Astronomical Society* 423.4 (11, 2012), pp. 3430–3444. DOI: [10.1111/j.1365-2966.2012.21136.x](https://doi.org/10.1111/j.1365-2966.2012.21136.x) (cit. on p. 20).
- [BNS01] Somnath Bharadwaj, Biman B. Nath, and Shiv K. Sethi. “Using HI to Probe Large Scale Structures at Z~3”. In: *Journal of Astrophysics and Astronomy* 22 (1, 2001), pp. 21–34. DOI: [10.1007/BF02933588](https://doi.org/10.1007/BF02933588) (cit. on p. 66).
- [Bia+15] Davide Bianchi, Héctor Gil-Marín, Rossana Ruggeri, and Will J. Percival. “Measuring Line-of-Sight-Dependent Fourier-space Clustering Using FFTs”. In: *Monthly Notices of the Royal Astronomical Society* 453 (1, 2015), pp. L11–L15. DOI: [10.1093/mnrasl/slv090](https://doi.org/10.1093/mnrasl/slv090) (cit. on p. 53).
- [BP17] Davide Bianchi and Will J. Percival. “Unbiased Clustering Estimation in the Presence of Missing Observations”. In: *Monthly Notices of the Royal Astronomical Society* 472.1 (2017), p. 1106. DOI: [10.1093/mnras/stx2053](https://doi.org/10.1093/mnras/stx2053) (cit. on pp. 47, 53).
- [BIC+21] BICEP/Keck et al. “A Demonstration of Improved Constraints on Primordial Gravitational Waves with Delensing”. In: *Physical Review D* 103.2 (26, 2021), p. 022004. DOI: [10.1103/PhysRevD.103.022004](https://doi.org/10.1103/PhysRevD.103.022004) (cit. on p. 21).
- [Bir+20] S. Birrer, A. J. Shajib, A. Galan, M. Millon, T. Treu, A. Agnello, M. Auger, G. C.-F. Chen, L. Christensen, T. Collett, F. Courbin, C. D. Fassnacht, L. V. E. Koopmans, P. J. Marshall, J.-W. Park, C. E. Rusu, D. Sluse, C. Spinelli, S. H. Suyu, S. Wagner-Carena, K. C. Wong, M. Barnabè, A. S. Bolton, O. Czoske, X. Ding, J. A. Frieman, and L. Van de Vyvere. “TDCOSMO - IV. Hierarchical Time-Delay Cosmography – Joint Inference of the Hubble Constant and Galaxy Density Profiles”. In: *Astronomy & Astrophysics* 643 (1, 2020), A165. DOI: [10.1051/0004-6361/202038861](https://doi.org/10.1051/0004-6361/202038861) (cit. on p. 17).
- [Bla+17] Michael R. Blanton, Matthew A. Bershady, et al. “Sloan Digital Sky Survey IV: Mapping the Milky Way, Nearby Galaxies, and the Distant Universe”. In: *The Astronomical Journal* 154.1 (2017), p. 28. DOI: [10.3847/1538-3881/aa7567](https://doi.org/10.3847/1538-3881/aa7567) (cit. on p. 20).
- [Bla+03] Michael R. Blanton, Huan Lin, Robert H. Lupton, F. Miller Maley, Neal Young, Idit Zehavi, and Jon Loveday. “An Efficient Targeting Strategy for Multiobject Spectrograph Surveys: The Sloan Digital Sky Survey “Tiling” Algorithm”. In: *The Astronomical Journal* 125 (1, 2003), pp. 2276–2286. DOI: [10.1086/344761](https://doi.org/10.1086/344761) (cit. on p. 26).
- [Blo+19] Michael Blomqvist, Hélion du Mas des Bourboux, Nicolás G. Busca, Victoria de Sainte Agathe, James Rich, Christophe Balland, Julian E. Bautista, Kyle Dawson, Andreu Font-Ribera, Julien Guy, Jean-Marc Le Goff, Nathalie Palanque-Delabrouille, Will J. Percival, Ignasi Pérez-Ràfols, Matthew M. Pieri, Donald P. Schneider, Anže Slosar, and Christophe Yèche. “Baryon Acoustic Oscillations from the Cross-Correlation of Ly\$\alpha\$ Absorption and Quasars in eBOSS DR14”. In: *Astronomy and Astrophysics* 629 (2019), A86. DOI: [10.1051/0004-6361/201935641](https://doi.org/10.1051/0004-6361/201935641) (cit. on p. 31).

## Bibliography

- [Blo+18] Michael Blomqvist, Matthew M. Pieri, Hélion du Mas des Bourboux, Nicolás G. Busca, Anže Slosar, Julian E. Bautista, Jonathan Brinkmann, Joel R. Brownstein, Kyle Dawson, Victoria de Sainte Agathe, Julien Guy, Will J. Percival, Ignasi Pérez-Ràfols, James Rich, and Donald P. Schneider. “The Triply-Ionized Carbon Forest from eBOSS: Cosmological Correlations with Quasars in SDSS-IV DR14”. In: *Journal of Cosmology and Astroparticle Physics* 2018.5 (2018), p. 029. DOI: [10.1088/1475-7516/2018/05/029](https://doi.org/10.1088/1475-7516/2018/05/029) (cit. on p. 36).
- [Bro+19a] D. Brout, M. Sako, D. Scolnic, R. Kessler, C. B. D’Andrea, T. M. Davis, S. R. Hinton, A. G. Kim, J. Lasker, E. Macaulay, A. Möller, R. C. Nichol, M. Smith, M. Sullivan, R. C. Wolf, S. Allam, B. A. Bassett, P. Brown, F. J. Castander, M. Childress, R. J. Foley, L. Galbany, K. Herner, E. Kasai, M. March, E. Morganson, P. Nugent, Y.-C. Pan, R. C. Thomas, B. E. Tucker, W. Wester, T. M. C. Abbott, J. Annis, S. Avila, E. Bertin, D. Brooks, D. L. Burke, A. Carnero Rosell, M. Carrasco Kind, J. Carretero, M. Crocce, C. E. Cunha, L. N. da Costa, C. Davis, J. De Vicente, S. Desai, H. T. Diehl, P. Doel, T. F. Eifler, B. Flaugher, P. Fosalba, J. Frieman, J. García-Bellido, E. Gaztanaga, D. W. Gerdes, D. A. Goldstein, D. Gruen, R. A. Gruendl, J. Gschwend, G. Gutierrez, W. G. Hartley, D. L. Hollowood, K. Honscheid, D. J. James, K. Kuehn, N. Kuropatkin, O. Lahav, T. S. Li, M. Lima, J. L. Marshall, P. Martini, R. Miquel, B. Nord, A. A. Plazas, A. Roodman, E. S. Rykoff, E. Sanchez, V. Scarpine, R. Schindler, M. Schubnell, S. Serrano, I. Sevilla-Noarbe, M. Soares-Santos, F. Sobreira, E. Suchyta, M. E. C. Swanson, G. Tarle, D. Thomas, D. L. Tucker, A. R. Walker, B. Yanny, Y. Zhang, and DES COLLABORATION. “First Cosmology Results Using Type Ia Supernovae from the Dark Energy Survey: Photometric Pipeline and Light-curve Data Release”. In: *The Astrophysical Journal* 874 (1, 2019), p. 106. DOI: [10.3847/1538-4357/ab06c1](https://doi.org/10.3847/1538-4357/ab06c1) (cit. on p. 18).
- [Bro+19b] D. Brout, D. Scolnic, et al. “First Cosmology Results Using SNe Ia from the Dark Energy Survey: Analysis, Systematic Uncertainties, and Validation”. In: *The Astrophysical Journal* 874.2 (2019), p. 150. DOI: [10.3847/1538-4357/ab08a0](https://doi.org/10.3847/1538-4357/ab08a0) (cit. on p. 18).
- [BPH15] A. Burden, W. J. Percival, and C. Howlett. “Reconstruction in Fourier Space”. In: *Monthly Notices of the Royal Astronomical Society* 453 (1, 2015), pp. 456–468. DOI: [10.1093/mnras/stv1581](https://doi.org/10.1093/mnras/stv1581) (cit. on p. 51).
- [Bur+14] A. Burden, W. J. Percival, M. Manera, Antonio J. Cuesta, Mariana Vargas Magana, and Shirley Ho. “Efficient Reconstruction of Linear Baryon Acoustic Oscillations in Galaxy Surveys”. In: *Monthly Notices of the Royal Astronomical Society* 445 (1, 2014), pp. 3152–3168. DOI: [10.1093/mnras/stu1965](https://doi.org/10.1093/mnras/stu1965) (cit. on p. 51).
- [Bus+13] N. G. Busca, T. Delubac, J. Rich, S. Bailey, A. Font-Ribera, D. Kirkby, J.-M. Le Goff, M. M. Pieri, A. Slosar, É. Aubourg, J. E. Bautista, D. Bizyaev, M. Blomqvist, A. S. Bolton, J. Bovy, H. Brewington, A. Borde, J. Brinkmann, B. Carithers, R. A. C. Croft, K. S. Dawson, G. Ebelke, D. J. Eisenstein, J.-C. Hamilton, S. Ho, D. W. Hogg, K. Honscheid, K.-G. Lee, B. Lundgren, E. Malanushenko, V. Malanushenko, D. Margala, C. Maraston, K. Mehta, J. Miralda-Escudé, A. D. Myers, R. C. Nichol, P. Noterdaeme, M. D. Olmstead, D. Oravetz, N. Palanque-Delabrouille, K. Pan, I. Pâris, W. J. Percival, P. Petitjean, N. A. Roe, E. Rollinde, N. P. Ross, G. Rossi, D. J. Schlegel, D. P. Schneider, A. Shelden, E. S. Sheldon, A. Simmons, S. Snedden, J. L. Tinker, M. Viel, B. A. Weaver, D. H. Weinberg, M. White, C. Yèche, and D. G.

- York. “Baryon Acoustic Oscillations in the Ly $\alpha$  Forest of BOSS Quasars”. In: *Astronomy and Astrophysics* 552 (1, 2013), A96. DOI: [10.1051/0004-6361/201220724](https://doi.org/10.1051/0004-6361/201220724) (cit. on pp. 31, 32).
- [CRW13] Jordan Carlson, Beth Reid, and Martin White. “Convolution Lagrangian Perturbation Theory for Biased Tracers”. In: *Monthly Notices of the Royal Astronomical Society* 429 (1, 2013), pp. 1674–1685. DOI: [10.1093/mnras/sts457](https://doi.org/10.1093/mnras/sts457) (cit. on p. 59).
- [Car+20] Paul Carter, Florian Beutler, Will J. Percival, Joseph DeRose, Risa H. Wechsler, and Cheng Zhao. “The Impact of the Fiducial Cosmology Assumption on BAO Distance Scale Measurements”. In: *Monthly Notices of the Royal Astronomical Society* 494 (1, 2020), pp. 2076–2089. DOI: [10.1093/mnras/staa761](https://doi.org/10.1093/mnras/staa761) (cit. on p. 51).
- [Cha+20] Solène Chabanier, Frédéric Bournaud, Yohan Dubois, Nathalie Palanque-Delabrouille, Christophe Yèche, Eric Armengaud, Sébastien Peirani, and Ricarda Beckmann. “The Impact of AGN Feedback on the 1D Power Spectra from the Ly $\alpha$  Forest Using the Horizon-AGN Suite of Simulations”. In: *Monthly Notices of the Royal Astronomical Society* 495 (1, 2020), pp. 1825–1840. DOI: [10.1093/mnras/staa1242](https://doi.org/10.1093/mnras/staa1242) (cit. on p. 30).
- [Cha98] B. Chaboyer. “The Age of the Universe.” In: *Physics Reports* 307 (1, 1998), pp. 23–30. DOI: [10.1016/S0370-1573\(98\)00054-4](https://doi.org/10.1016/S0370-1573(98)00054-4) (cit. on p. 10).
- [Cha+08] Tzu-Ching Chang, Ue-Li Pen, Jeffrey B. Peterson, and Patrick McDonald. “Baryon Acoustic Oscillation Intensity Mapping of Dark Energy”. In: *Physical Review Letters* 100 (1, 2008), p. 091303. DOI: [10.1103/PhysRevLett.100.091303](https://doi.org/10.1103/PhysRevLett.100.091303) (cit. on p. 66).
- [Cha+21] Edmond Chaussidon, Christophe Yèche, Nathalie Palanque-Delabrouille, Arnaud de Mattia, Adam D. Myers, Mehdi Rezaie, Ashley J. Ross, Hee-Jong Seo, David Brooks, Enrique Gaztañaga, Robert Kehoe, Michael E. Levi, Jeffrey A. Newman, Gregory Tarlé, and Kai Zhang. “Angular Clustering Properties of the DESI QSO Target Selection Using DR9 Legacy Imaging Surveys”. In: *Monthly Notices of the Royal Astronomical Society* 509.3 (2, 2021), pp. 3904–3923. DOI: [10.1093/mnras/stab3252](https://doi.org/10.1093/mnras/stab3252) (cit. on p. 47).
- [CP01] Michel Chevallier and David Polarski. “Accelerating Universes with Scaling Dark Matter”. In: *International Journal of Modern Physics D* 10 (1, 2001), pp. 213–223. DOI: [10.1142/S0218271801000822](https://doi.org/10.1142/S0218271801000822) (cit. on p. 12).
- [Chu+15] Chia-Hsun Chuang, Francisco-Shu Kitaura, Francisco Prada, Cheng Zhao, and Gustavo Yepes. “EZmocks: Extending the Zel’dovich Approximation to Generate Mock Galaxy Catalogues with Accurate Clustering Statistics”. In: *Monthly Notices of the Royal Astronomical Society* 446.3 (2015), p. 2621. DOI: [10.1093/mnras/stu2301](https://doi.org/10.1093/mnras/stu2301) (cit. on p. 52).
- [Col+05] Shaun Cole, Will J. Percival, John A. Peacock, Peder Norberg, Carlton M. Baugh, Carlos S. Frenk, Ivan Baldry, Joss Bland-Hawthorn, Terry Bridges, Russell Cannon, Matthew Colless, Chris Collins, Warrick Couch, Nicholas J. G. Cross, Gavin Dalton, Vincent R. Eke, Roberto De Propris, Simon P. Driver, George Efstathiou, Richard S. Ellis, Karl Glazebrook, Carole Jackson, Adrian Jenkins, Ofer Lahav, Ian Lewis, Stuart Lumsden, Steve Maddox, Darren Madgwick, Bruce A. Peterson, Will Sutherland, and Keith Taylor. “The 2dF Galaxy Redshift Survey: Power-

- Spectrum Analysis of the Final Data Set and Cosmological Implications". In: *Monthly Notices of the Royal Astronomical Society* 362 (1, 2005), pp. 505–534. DOI: [10.1111/j.1365-2966.2005.09318.x](https://doi.org/10.1111/j.1365-2966.2005.09318.x) (cit. on p. 10).
- [Col+21] DES Collaboration et al. "Dark Energy Survey Year 3 Results: Cosmological Constraints from Galaxy Clustering and Weak Lensing". 27, 2021 (cit. on p. 23).
- [CC17] The LIGO Scientific Collaboration and The Virgo Collaboration. "GW170817: Observation of Gravitational Waves from a Binary Neutron Star Inspiral". In: *Physical Review Letters* 119.16 (16, 2017), p. 161101. DOI: [10.1103/PhysRevLett.119.161101](https://doi.org/10.1103/PhysRevLett.119.161101) (cit. on p. 17).
- [CtV16] The LIGO Scientific Collaboration and the Virgo Collaboration. "Observation of Gravitational Waves from a Binary Black Hole Merger". In: *Physical Review Letters* 116.6 (11, 2016), p. 061102. DOI: [10.1103/PhysRevLett.116.061102](https://doi.org/10.1103/PhysRevLett.116.061102) (cit. on p. 17).
- [CRM18] Rupert A. C. Croft, Alessandro Romeo, and R. Benton Metcalf. "Weak Lensing of the Lyman  $\alpha$  Forest". In: *Monthly Notices of the Royal Astronomical Society* 477 (1, 2018), pp. 1814–1821. DOI: [10.1093/mnras/sty650](https://doi.org/10.1093/mnras/sty650) (cit. on p. 41).
- [Cro+99] Rupert A. C. Croft, David H. Weinberg, Max Pettini, Lars Hernquist, and Neal Katz. "The Power Spectrum of Mass Fluctuations Measured from the LYalpha Forest at Redshift Z=2.5". In: *The Astrophysical Journal* 520 (1, 1999), pp. 1–23. DOI: [10.1086/307438](https://doi.org/10.1086/307438); (cit. on p. 30).
- [Cuc+21] Andrei Cuceu, Andreu Font-Ribera, Benjamin Joachimi, and Seshadri Nadathur. "Cosmology beyond BAO from the 3D Distribution of the Lyman-\$\alpha\$ Forest". 25, 2021 (cit. on p. 41).
- [dBer+00] P. de Bernardis, P. A. R. Ade, J. J. Bock, J. R. Bond, J. Borrill, A. Boscaleri, K. Coble, B. P. Crill, G. De Gasperis, P. C. Farese, P. G. Ferreira, K. Ganga, M. Giacometti, E. Hivon, V. V. Hristov, A. Iacoangeli, A. H. Jaffe, A. E. Lange, L. Martinis, S. Masi, P. V. Mason, P. D. Mauskopf, A. Melchiorri, L. Miglio, T. Montroy, C. B. Netterfield, E. Pascale, F. Piacentini, D. Pogosyan, S. Prunet, S. Rao, G. Romeo, J. E. Ruhl, F. Scaramuzzi, D. Sforna, and N. Vittorio. "A Flat Universe from High-Resolution Maps of the Cosmic Microwave Background Radiation". In: *Nature* 404 (1, 2000), pp. 955–959. DOI: [10.1038/35010035](https://doi.org/10.1038/35010035) (cit. on p. 9).
- [Del+15] Timothée Delubac, Julian E. Bautista, Nicolás G. Busca, James Rich, David Kirkby, Stephen Bailey, Andreu Font-Ribera, Anže Slosar, Khee-Gan Lee, Matthew M. Pieri, Jean-Christophe Hamilton, Éric Aubourg, Michael Blomqvist, Jo Bovy, Jon Brinkmann, William Carithers, Kyle S. Dawson, Daniel J. Eisenstein, Satya Gontcho A. Gontcho, Jean-Paul Kneib, Jean-Marc Le Goff, Daniel Margala, Jordi Miralda-Escudé, Adam D. Myers, Robert C. Nichol, Pasquier Noterdaeme, Ross O'Connell, Matthew D. Olmstead, Nathalie Palanque-Delabrouille, Isabelle Pâris, Patrick Petitjean, Nicholas P. Ross, Graziano Rossi, David J. Schlegel, Donald P. Schneider, David H. Weinberg, Christophe Yèche, and Donald G. York. "Baryon Acoustic Oscillations in the Ly $\alpha$  Forest of BOSS DR11 Quasars". In: *Astronomy and Astrophysics* 574 (1, 2015), A59. DOI: [10.1051/0004-6361/201423969](https://doi.org/10.1051/0004-6361/201423969) (cit. on pp. 31, 35).

- [dMR19] Arnaud de Mattia and Vanina Ruhlmann-Kleider. “Integral Constraints in Spectroscopic Surveys”. In: *Journal of Cosmology and Astroparticle Physics* 08 (1, 2019), p. 036. DOI: [10.1088/1475-7516/2019/08/036](https://doi.org/10.1088/1475-7516/2019/08/036) (cit. on p. 49).
- [dMat+21] Arnaud de Mattia, Vanina Ruhlmann-Kleider, Anand Raichoor, Ashley J. Ross, Amélie Tamone, Cheng Zhao, Shadab Alam, Santiago Avila, Etienne Burtin, Julian Bautista, Florian Beutler, Jonathan Brinkmann, Joel R. Brownstein, Michael J. Chapman, Chia-Hsun Chuang, Johan Comparat, Hélion du Mas des Bourboux, Kyle S. Dawson, Axel de la Macorra, Héctor Gil-Marín, Violeta Gonzalez-Perez, Claudio Gorgoni, Jiamin Hou, Hui Kong, Sicheng Lin, Seshadri Nadathur, Jeffrey A. Newman, Eva-Maria Mueller, Will J. Percival, Mehdi Rezaie, Graziano Rossi, Donald P. Schneider, Prabhakar Tiwari, M. Vivek, Yuting Wang, and Gong-Bo Zhao. “The Completed SDSS-IV Extended Baryon Oscillation Spectroscopic Survey: Measurement of the BAO and Growth Rate of Structure of the Emission Line Galaxy Sample from the Anisotropic Power Spectrum between Redshift 0.6 and 1.1”. In: *Monthly Notices of the Royal Astronomical Society* 501 (1, 2021), pp. 5616–5645. DOI: [10.1093/mnras/staa3891](https://doi.org/10.1093/mnras/staa3891) (cit. on pp. 22, 49).
- [dSai+19] Victoria de Sainte Agathe, Christophe Balland, Hélion du Mas des Bourboux, Nicolás G. Busca, Michael Blomqvist, Julien Guy, James Rich, Andreu Font-Ribera, Matthew M. Pieri, Julian E. Bautista, Kyle Dawson, Jean-Marc Le Goff, Axel de la Macorra, Nathalie Palanque-Delabrouille, Will J. Percival, Ignasi Pérez-Ràfols, Donald P. Schneider, Anže Slosar, and Christophe Yèche. “Baryon Acoustic Oscillations at  $z = 2.34$  from the Correlations of Ly $\alpha$  Absorption in eBOSS DR14”. In: *Astronomy and Astrophysics* 629 (2019), A85. DOI: [10.1051/0004-6361/201935638](https://doi.org/10.1051/0004-6361/201935638) (cit. on p. 31).
- [DS20] Scott Dodelson and Fabian Schmidt. *Modern Cosmology - 2nd Edition*. 2nd ed. Elsevier, 18, 2020 (cit. on p. 21).
- [Doi+10] Mamoru Doi, Masayuki Tanaka, Masataka Fukugita, James E. Gunn, Naoki Yasuda, Željko Ivezić, Jon Brinkmann, Ernst de Haars, S. J. Kleinman, Jurek Krzesinski, and R. French Leger. “Photometric Response Functions of the Sloan Digital Sky Survey Imager”. In: *The Astronomical Journal* 139 (1, 2010), pp. 1628–1648. DOI: [10.1088/0004-6256/139/4/1628](https://doi.org/10.1088/0004-6256/139/4/1628) (cit. on p. 24).
- [dMas+20] Hélion du Mas des Bourboux Helion, James Rich, Andreu Font-Ribera, Victoria de Sainte Agathe, James Farr, Thomas Etourneau, Jean-Marc Le Goff, Andrei Cuceu, Christophe Balland, Julian E. Bautista, Michael Blomqvist, Jonathan Brinkmann, Joel R. Brownstein, Solène Chabanier, Edmond Chaussidon, Kyle Dawson, Alma X. González-Morales, Julien Guy, Brad W. Lyke, Axel de la Macorra, Eva-Maria Mueller, Adam D. Myers, Christian Nitschelm, Andrea Muñoz Gutiérrez, Nathalie Palanque-Delabrouille, James Parker, Will J. Percival, Ignasi Pérez-Ràfols, Patrick Petitjean, Matthew M. Pieri, Corentin Ravoux, Graziano Rossi, Donald P. Schneider, Hee-Jong Seo, Anže Slosar, Julianna Stermer, M. Vivek, Christophe Yèche, and Samantha Youles. “The Completed SDSS-IV Extended Baryon Oscillation Spectroscopic Survey: Baryon Acoustic Oscillations with Ly $\alpha$  Forests”. In: *The Astrophysical Journal* 901.2 (2020), p. 153. DOI: [10.3847/1538-4357/abb085](https://doi.org/10.3847/1538-4357/abb085) (cit. on pp. 31, 35, 37).

## Bibliography

- [dMas+17] Hélion du Mas des Bourboux, Jean-Marc Le Goff, Michael Blomqvist, Nicolás G. Busca, Julien Guy, James Rich, Christophe Yèche, Julian E. Bautista, Étienne Burtin, Kyle S. Dawson, Daniel J. Eisenstein, Andreu Font-Ribera, David Kirkby, Jordi Miralda-Escudé, Pasquier Noterdaeme, Nathalie Palanque-Delabrouille, Isabelle Pâris, Patrick Petitjean, Ignasi Pérez-Ràfols, Matthew M. Pieri, Nicholas P. Ross, David J. Schlegel, Donald P. Schneider, Anže Slosar, David H. Weinberg, and Pauline Zarrouk. “Baryon Acoustic Oscillations from the Complete SDSS-III Ly $\alpha$ -Quasar Cross-Correlation Function at  $z = 2.4$ ”. In: *Astronomy and Astrophysics* 608 (1, 2017), A130. DOI: [10.1051/0004-6361/201731731](https://doi.org/10.1051/0004-6361/201731731) (cit. on p. 31).
- [Dut+21] D. Dutcher et al. “Measurements of the E-Mode Polarization and Temperature-E-Mode Correlation of the CMB from SPT-3G 2018 Data”. In: *Physical Review D* 104.2 (13, 2021), p. 022003. DOI: [10.1103/PhysRevD.104.022003](https://doi.org/10.1103/PhysRevD.104.022003) (cit. on p. 21).
- [ESM90] G. Efstathiou, W. J. Sutherland, and S. J. Maddox. “The Cosmological Constant and Cold Dark Matter”. In: *Nature* 348 (1, 1990), pp. 705–707. DOI: [10.1038/348705a0](https://doi.org/10.1038/348705a0) (cit. on p. 9).
- [Eis+07] Daniel J. Eisenstein, Hee-Jong Seo, Edwin Sirk, and David N. Spergel. “Improving Cosmological Distance Measurements by Reconstruction of the Baryon Acoustic Peak”. In: *The Astrophysical Journal* 664 (1, 2007), pp. 675–679. DOI: [10.1086/518712](https://doi.org/10.1086/518712) (cit. on p. 51).
- [ESW07] Daniel J. Eisenstein, Hee-Jong Seo, and Martin White. “On the Robustness of the Acoustic Scale in the Low-Redshift Clustering of Matter”. In: *The Astrophysical Journal* 664 (1, 2007), pp. 660–674. DOI: [10.1086/518755](https://doi.org/10.1086/518755) (cit. on p. 50).
- [Eis+11] Daniel J. Eisenstein, David H. Weinberg, et al. “SDSS-III: Massive Spectroscopic Surveys of the Distant Universe, the Milky Way, and Extra-Solar Planetary Systems”. In: *The Astronomical Journal* 142 (1, 2011), p. 72. DOI: [10.1088/0004-6256/142/3/72](https://doi.org/10.1088/0004-6256/142/3/72); (cit. on p. 20).
- [Eis+05] Daniel J. Eisenstein, Idit Zehavi, David W. Hogg, Roman Scoccimarro, Michael R. Blanton, Robert C. Nichol, Ryan Scranton, Hee-Jong Seo, Max Tegmark, Zheng Zheng, Scott F. Anderson, Jim Annis, Neta Bahcall, Jon Brinkmann, Scott Burles, Francisco J. Castander, Andrew Connolly, Istvan Csabai, Mamoru Doi, Masataka Fukugita, Joshua A. Frieman, Karl Glazebrook, James E. Gunn, John S. Hendry, Gregory Hennessy, Zeljko Ivezic, Stephen Kent, Gillian R. Knapp, Huan Lin, Yeong-Shang Loh, Robert H. Lupton, Bruce Margon, Timothy A. McKay, Avery Meiksin, Jeffery A. Munn, Adrian Pope, Michael W. Richmond, David Schlegel, Donald P. Schneider, Kazuhiro Shimasaku, Christopher Stoughton, Michael A. Strauss, Mark SubbaRao, Alexander S. Szalay, István Szapudi, Douglas L. Tucker, Brian Yanny, and Donald G. York. “Detection of the Baryon Acoustic Peak in the Large-Scale Correlation Function of SDSS Luminous Red Galaxies”. In: *The Astrophysical Journal* 633.2 (2005), p. 560. DOI: [10.1086/466512](https://doi.org/10.1086/466512) (cit. on p. 10).
- [Fau+08] Claude-André Faucher-Giguère, Jason X. Prochaska, Adam Lidz, Lars Hernquist, and Matias Zaldarriaga. “A Direct Precision Measurement of the Intergalactic Ly $\alpha$  Opacity at  $2 \leq z \leq 4.2$ ”. In: *The Astrophysical Journal* 681 (1, 2008), pp. 831–855. DOI: [10.1086/588648](https://doi.org/10.1086/588648) (cit. on p. 32).

## Bibliography

- [FKP94] Hume A. Feldman, Nick Kaiser, and John A. Peacock. “Power-Spectrum Analysis of Three-dimensional Redshift Surveys”. In: *The Astrophysical Journal* 426 (1994), p. 23. DOI: [10.1086/174036](https://doi.org/10.1086/174036) (cit. on pp. 50, 53).
- [Fix09] D. J. Fixsen. “The Temperature of the Cosmic Microwave Background”. In: *The Astrophysical Journal* 707 (1, 2009), pp. 916–920. DOI: [10.1088/0004-637X/707/2/916](https://doi.org/10.1088/0004-637X/707/2/916) (cit. on p. 20).
- [Fon+14] Andreu Font-Ribera, David Kirkby, Nicolas Busca, Jordi Miralda-Escudé, Nicholas P. Ross, Anže Slosar, James Rich, Éric Aubourg, Stephen Bailey, Vaishali Bhardwaj, Julian Bautista, Florian Beutler, Dmitry Bizyaev, Michael Blomqvist, Howard Brewington, Jon Brinkmann, Joel R. Brownstein, Bill Carithers, Kyle S. Dawson, Timothée Delubac, Garrett Ebelke, Daniel J. Eisenstein, Jian Ge, Karen Kinemuchi, Khee-Gan Lee, Viktor Malanushenko, Elena Malanushenko, Moses Marchante, Daniel Margala, Demitri Muna, Adam D. Myers, Pasquier Noterdaeme, Daniel Oravetz, Nathalie Palanque-Delabrouille, Isabelle Pâris, Patrick Petitjean, Matthew M. Pieri, Graziano Rossi, Donald P. Schneider, Audrey Simmons, Matteo Viel, Christophe Yèche, and Donald G. York. “Quasar-Lyman-\$\alpha\$ Forest Cross-Correlation from BOSS DR11: Baryon Acoustic Oscillations”. In: *Journal of Cosmology and Astro-Particle Physics* 05 (1, 2014), p. 027. DOI: [10.1088/1475-7516/2014/05/027](https://doi.org/10.1088/1475-7516/2014/05/027) (cit. on p. 31).
- [FM12] Andreu Font-Ribera and Jordi Miralda-Escudé. “The Effect of High Column Density Systems on the Measurement of the Lyman- $\alpha$  Forest Correlation Function”. In: *Journal of Cosmology and Astro-Particle Physics* 2012.7 (2012), p. 028. DOI: [10.1088/1475-7516/2012/07/028](https://doi.org/10.1088/1475-7516/2012/07/028) (cit. on p. 35).
- [Fon+12] Andreu Font-Ribera, Jordi Miralda-Escudé, Eduard Arnau, Bill Carithers, Khee-Gan Lee, Pasquier Noterdaeme, Isabelle Pâris, Patrick Petitjean, James Rich, Emmanuel Rollinde, Nicholas P. Ross, Donald P. Schneider, Martin White, and Donald G. York. “The Large-Scale Cross-Correlation of Damped Lyman Alpha Systems with the Lyman Alpha Forest: First Measurements from BOSS”. In: *Journal of Cosmology and Astroparticle Physics* 2012.11 (28, 2012), pp. 059–059. DOI: [10.1088/1475-7516/2012/11/059](https://doi.org/10.1088/1475-7516/2012/11/059) (cit. on p. 33).
- [Fre+19] Wendy L. Freedman, Barry F. Madore, Dylan Hatt, Taylor J. Hoyt, In-Sung Jang, Rachael L. Beaton, Christopher R. Burns, Myung Gyoong Lee, Andrew J. Monson, Jillian R. Neeley, Mark M. Phillips, Jeffrey A. Rich, and Mark Seibert. “The Carnegie-Chicago Hubble Program. VIII. An Independent Determination of the Hubble Constant Based on the Tip of the Red Giant Branch”. In: *The Astrophysical Journal* 882.1 (29, 2019), p. 34. DOI: [10.3847/1538-4357/ab2f73](https://doi.org/10.3847/1538-4357/ab2f73) (cit. on p. 17).
- [Gil+20] Héctor Gil-Marín, Julián E. Bautista, Romain Paviot, Mariana Vargas-Magaña, Sylvain de la Torre, Sébastien Fromenteau, Shadab Alam, Santiago Ávila, Etienne Burtin, Chia-Hsun Chuang, Kyle S. Dawson, Jiamin Hou, Arnaud de Mattia, Faizan G. Mohammad, Eva-Maria Müller, Seshadri Nadathur, Richard Neveux, Will J. Percival, Anand Raichoor, Mehdi Rezaie, Ashley J. Ross, Graziano Rossi, Vanina Ruhlmann-Kleider, Alex Smith, Amélie Tamone, Jeremy L. Tinker, Rita Tojeiro, Yuting Wang, Gong-Bo Zhao, Cheng Zhao, Jonathan Brinkmann, Joel R. Brownstein, Peter D. Choi, Stephanie Escoffier, Axel de la Macorra, Jeongin Moon, Jeffrey A. Newman, Donald P. Schneider, Hee-Jong Seo, and Mariappan Vivek. “The Completed SDSS-IV Extended Baryon Oscillation Spectroscopic Survey:

- Measurement of the BAO and Growth Rate of Structure of the Luminous Red Galaxy Sample from the Anisotropic Power Spectrum between Redshifts 0.6 and 1.0". In: *Monthly Notices of the Royal Astronomical Society* 498 (1, 2020), pp. 2492–2531. DOI: [10.1093/mnras/staa2455](https://doi.org/10.1093/mnras/staa2455) (cit. on pp. 22, 45, 57).
- [Gra+19] Matthew J. Graham et al. "The Zwicky Transient Facility: Science Objectives". In: *Publications of the Astronomical Society of the Pacific* 131 (1, 2019), p. 078001. DOI: [10.1088/1538-3873/ab006c](https://doi.org/10.1088/1538-3873/ab006c) (cit. on p. 18).
- [Gra+20] R. Graziani, M. Rigault, N. Regnault, Ph Gris, A. Möller, P. Antilogus, P. Astier, M. Betoule, S. Bongard, M. Briday, J. Cohen-Tanugi, Y. Copin, H. M. Courtois, D. Fouchez, E. Gangler, D. Guinet, A. J. Hawken, Y.-L. Kim, P.-F. Léget, J. Neveu, P. Ntelis, Ph Rosnet, and E. Nuss. "Peculiar Velocity Cosmology with Type Ia Supernovae". 24, 2020 (cit. on p. 18).
- [Gun+98] J. E. Gunn, M. Carr, C. Rockosi, M. Sekiguchi, K. Berry, B. Elms, E. de Haas, Ž. Ivezić, G. Knapp, R. Lupton, G. Pauls, R. Simcoe, R. Hirsch, D. Sanford, S. Wang, D. York, F. Harris, J. Annis, L. Bartozek, W. Boroski, J. Bakken, M. Haldeman, S. Kent, S. Holm, D. Holmgren, D. Petravick, A. Protopiano, R. Rechenmacher, M. Doi, M. Fukugita, K. Shimasaku, N. Okada, C. Hull, W. Siegmund, E. Mannery, M. Blouke, D. Heidtman, D. Schneider, R. Lucinio, and J. Brinkman. "The Sloan Digital Sky Survey Photometric Camera". In: *The Astronomical Journal* 116 (1, 1998), pp. 3040–3081. DOI: [10.1086/300645](https://doi.org/10.1086/300645) (cit. on p. 24).
- [GP65] James E. Gunn and Bruce A. Peterson. "On the Density of Neutral Hydrogen in Intergalactic Space." In: *The Astrophysical Journal* 142 (1, 1965), pp. 1633–1641. DOI: [10.1086/148444](https://doi.org/10.1086/148444) (cit. on p. 30).
- [GZZ12] Hong Guo, Idit Zehavi, and Zheng Zheng. "A New Method to Correct for Fiber Collisions in Galaxy Two-point Statistics". In: *The Astrophysical Journal* 756.2 (2012), p. 127. DOI: [10.1088/0004-637X/756/2/127](https://doi.org/10.1088/0004-637X/756/2/127) (cit. on p. 47).
- [Han+17] Nick Hand, Yin Li, Zachary Slepian, and Uros Seljak. "An Optimal FFT-based Anisotropic Power Spectrum Estimator". In: *Journal of Cosmology and Astroparticle Physics* 2017.07 (3, 2017), pp. 002–002. DOI: [10.1088/1475-7516/2017/07/002](https://doi.org/10.1088/1475-7516/2017/07/002) (cit. on p. 53).
- [Her+99] J. R. Herrnstein, J. M. Moran, L. J. Greenhill, P. J. Diamond, M. Inoue, N. Nakai, M. Miyoshi, C. Henkel, and A. Riess. "A Geometric Distance to the Galaxy NGC4258 from Orbital Motions in a Nuclear Gas Disk". In: *Nature* 400.6744 (6744 1999), pp. 539–541. DOI: [10.1038/22972](https://doi.org/10.1038/22972) (cit. on p. 17).
- [Hey+21] Catherine Heymans, Tilman Tröster, Marika Asgari, Chris Blake, Hendrik Hildebrandt, Benjamin Joachimi, Konrad Kuijken, Chieh-An Lin, Ariel G. Sánchez, Jan Luca van den Busch, Angus H. Wright, Alexandra Amon, Maciej Bilicki, Jelte de Jong, Martin Crocce, Andrej Dvornik, Thomas Erben, Maria Cristina Fortuna, Fedor Getman, Benjamin Giblin, Karl Glazebrook, Henk Hoekstra, Shahab Joudaki, Arun Kannawadi, Fabian Köhlinger, Chris Lidman, Lance Miller, Nicola R. Napolitano, David Parkinson, Peter Schneider, HuanYuan Shan, Edwin Valentijn, Gijs Verdoes Kleijn, and Christian Wolf. "KiDS-1000 Cosmology: Multi-probe Weak Gravitational Lensing and Spectroscopic Galaxy Clustering Constraints". In: *Astronomy & Astrophysics* 646 (2021), A140. DOI: [10.1051/0004-6361/202039063](https://doi.org/10.1051/0004-6361/202039063) (cit. on p. 23).

## Bibliography

- [Hik+19] Chiaki Hikage, Masamune Oguri, Takashi Hamana, Surhud More, Rachel Mandelbaum, Masahiro Takada, Fabian Köhlinger, Hironao Miyatake, Atsushi J. Nishizawa, Hiroaki Aihara, Robert Armstrong, James Bosch, Jean Coupon, Anne Ducout, Paul Ho, Bau-Ching Hsieh, Yutaka Komiyama, François Lanusse, Alexie Leauthaud, Robert H. Lupton, Elinor Medezinski, Sogo Mineo, Shoken Miyama, Satoshi Miyazaki, Ryoma Murata, Hitoshi Murayama, Masato Shirasaki, Cristóbal Sifón, Melanie Simet, Joshua Speagle, David N. Spergel, Michael A. Strauss, Naoshi Sugiyama, Masayuki Tanaka, Yousuke Utsumi, Shiang-Yu Wang, and Yoshihiko Yamada. “Cosmology from Cosmic Shear Power Spectra with Subaru Hyper Suprime-Cam First-Year Data”. In: *Publications of the Astronomical Society of Japan* 71 (1, 2019), p. 43. DOI: [10.1093/pasj/psz010](https://doi.org/10.1093/pasj/psz010) (cit. on p. 23).
- [Hor86] K. Horne. “An Optimal Extraction Algorithm for CCD Spectroscopy.” In: *Publications of the Astronomical Society of the Pacific* 98 (1, 1986), pp. 609–617. DOI: [10.1086/131801](https://doi.org/10.1086/131801) (cit. on p. 27).
- [Hou+21] Jiamin Hou, Ariel G. Sánchez, Ashley J. Ross, Alex Smith, Richard Neveux, Julian Bautista, Etienne Burtin, Cheng Zhao, Román Scoccimarro, Kyle S. Dawson, Arnaud de Mattia, Axel de la Macorra, Hélion du Mas des Bourboux, Daniel J. Eisenstein, Héctor Gil-Marín, Brad W. Lyke, Faizan G. Mohammad, Eva-Maria Mueller, Will J. Percival, Graziano Rossi, Mariana Vargas Magaña, Pauline Zarrouk, Gong-Bo Zhao, Jonathan Brinkmann, Joel R. Brownstein, Chia-Hsun Chuang, Adam D. Myers, Jeffrey A. Newman, Donald P. Schneider, and M. Vivek. “The Completed SDSS-IV Extended Baryon Oscillation Spectroscopic Survey: BAO and RSD Measurements from Anisotropic Clustering Analysis of the Quasar Sample in Configuration Space between Redshift 0.8 and 2.2”. In: *Monthly Notices of the Royal Astronomical Society* 500 (1, 2021), pp. 1201–1221. DOI: [10.1093/mnras/staa3234](https://doi.org/10.1093/mnras/staa3234) (cit. on p. 22).
- [How+15] Cullan Howlett, Ashley J. Ross, Lado Samushia, Will J. Percival, and Marc Manera. “The Clustering of the SDSS Main Galaxy Sample - II. Mock Galaxy Catalogues and a Measurement of the Growth of Structure from Redshift Space Distortions at  $z = 0.15$ ”. In: *Monthly Notices of the Royal Astronomical Society* 449 (1, 2015), pp. 848–866. DOI: [10.1093/mnras/stu2693](https://doi.org/10.1093/mnras/stu2693) (cit. on p. 22).
- [Hub29] Edwin Hubble. “A Relation between Distance and Radial Velocity among Extra-Galactic Nebulae”. In: *Proceedings of the National Academy of Sciences* 15.3 (15, 1929), pp. 168–173. DOI: [10.1073/pnas.15.3.168](https://doi.org/10.1073/pnas.15.3.168) (cit. on p. 16).
- [Kai87] Nick Kaiser. “Clustering in Real Space and in Redshift Space”. In: *Monthly Notices of the Royal Astronomical Society* 227 (1, 1987), pp. 1–21. DOI: [10.1093/mnras/227.1.1](https://doi.org/10.1093/mnras/227.1.1) (cit. on p. 22).
- [Kam+20] Vikrant Kamble, Kyle Dawson, Hélion du Mas des Bourboux, Julian Bautista, and Donald P. Scheinder. “Measurements of Effective Optical Depth in the Ly $\alpha$  Forest from the BOSS DR12 Quasar Sample”. In: *The Astrophysical Journal* 892 (1, 2020), p. 70. DOI: [10.3847/1538-4357/ab76bd](https://doi.org/10.3847/1538-4357/ab76bd) (cit. on p. 32).
- [Kes+19] R Kessler et al. “First Cosmology Results Using Type Ia Supernova from the Dark Energy Survey: Simulations to Correct Supernova Distance Biases”. In: *Monthly Notices of the Royal Astronomical Society* 485.1 (1, 2019), pp. 1171–1187. DOI: [10.1093/mnras/stz463](https://doi.org/10.1093/mnras/stz463) (cit. on p. 18).

## Bibliography

- [KL20] Alex G. Kim and Eric V. Linder. “Complementarity of Peculiar Velocity Surveys and Redshift Space Distortions for Testing Gravity”. In: *Physical Review D* 101 (1, 2020), p. 023516. DOI: [10.1103/PhysRevD.101.023516](https://doi.org/10.1103/PhysRevD.101.023516) (cit. on p. 18).
- [Kir+13] David Kirkby, Daniel Margala, Anže Slosar, Stephen Bailey, Nicolás G. Busca, Timothée Delubac, James Rich, Julian E. Bautista, Michael Blomqvist, Joel R. Brownstein, Bill Carithers, Rupert A. C. Croft, Kyle S. Dawson, Andreu Font-Ribera, Jordi Miralda-Escudé, Adam D. Myers, Robert C. Nichol, Nathalie Palanque-Delabrouille, Isabelle Pâris, Patrick Petitjean, Graziano Rossi, David J. Schlegel, Donald P. Schneider, Matteo Viel, David H. Weinberg, and Christophe Yèche. “Fitting Methods for Baryon Acoustic Oscillations in the Lyman-\$\alpha\$ Forest Fluctuations in BOSS Data Release 9”. In: *Journal of Cosmology and Astro-Particle Physics* 2013.3 (2013), p. 024. DOI: [10.1088/1475-7516/2013/03/024](https://doi.org/10.1088/1475-7516/2013/03/024) (cit. on p. 31).
- [Kit+12] Francisco-Shu Kitaura, Raul E. Angulo, Yehuda Hoffman, and Stefan Gottlöber. “Estimating Cosmic Velocity Fields from Density Fields and Tidal Tensors”. In: *Monthly Notices of the Royal Astronomical Society* 425 (1, 2012), pp. 2422–2435. DOI: [10.1111/j.1365-2966.2012.21589.x](https://doi.org/10.1111/j.1365-2966.2012.21589.x) (cit. on p. 51).
- [LS93] Stephen D. Landy and Alexander S. Szalay. “Bias and Variance of Angular Correlation Functions”. In: *The Astrophysical Journal* 412 (1993), p. 64. DOI: [10.1086/172900](https://doi.org/10.1086/172900) (cit. on p. 52).
- [LSS12] Khee-Gan Lee, Nao Suzuki, and David N. Spergel. “Mean-Flux-Regulated Principal Component Analysis Continuum Fitting of Sloan Digital Sky Survey Ly $\alpha$  Forest Spectra”. In: *The Astronomical Journal* 143 (1, 2012), p. 51. DOI: [10.1088/0004-6256/143/2/51](https://doi.org/10.1088/0004-6256/143/2/51) (cit. on p. 32).
- [Les11] Julien Lesgourgues. “The Cosmic Linear Anisotropy Solving System (CLASS) I: Overview”. In: (14, 2011) (cit. on p. 21).
- [LCL00] Antony Lewis, Anthony Challinor, and Anthony Lasenby. “Efficient Computation of Cosmic Microwave Background Anisotropies in Closed Friedmann-Robertson-Walker Models”. In: *The Astrophysical Journal* 538 (1, 2000), pp. 473–476. DOI: [10.1086/309179](https://doi.org/10.1086/309179) (cit. on pp. 21, 35).
- [Lin03] Eric V. Linder. “Exploring the Expansion History of the Universe”. In: *Physical Review Letters* 90 (1, 2003), p. 091301. DOI: [10.1103/PhysRevLett.90.091301](https://doi.org/10.1103/PhysRevLett.90.091301) (cit. on p. 12).
- [Lup+01] R. Lupton, J. E. Gunn, Z. Ivezić, G. R. Knapp, and S. Kent. “The SDSS Imaging Pipelines”. In: 238 (1, 2001), p. 269 (cit. on p. 24).
- [Lyk+20] Brad W. Lyke, Alexandra N. Higley, J. N. McLane, Danielle P. Schurhammer, Adam D. Myers, Ashley J. Ross, Kyle Dawson, Solène Chabanier, Paul Martini, Nicolás G. Busca, Hélion du Mas des Bourboux, Mara Salvato, Alina Streblyanska, Pauline Zarrouk, Etienne Burtin, Scott F. Anderson, Julian Bautista, Dmitry Bizyaev, W. N. Brandt, Jonathan Brinkmann, Joel R. Brownstein, Johan Comparat, Paul Green, Axel de la Macorra, Andrea Muñoz Gutiérrez, Jiamin Hou, Jeffrey A. Newman, Nathalie Palanque-Delabrouille, Isabelle Pâris, Will J. Percival, Patrick Petitjean, James Rich, Graziano Rossi, Donald P. Schneider, Alexander Smith, M. Vivek, and Benjamin Alan Weaver. “The Sloan Digital Sky Survey Quasar Catalog: Sixteenth

- Data Release". In: *The Astrophysical Journal Supplement Series* 250 (1, 2020), p. 8. DOI: [10.3847/1538-4365/aba623](https://doi.org/10.3847/1538-4365/aba623) (cit. on p. 38).
- [Mad+90] S. J. Maddox, G. Efstathiou, W. J. Sutherland, and J. Loveday. "Galaxy Correlations on Large Scales." In: *Monthly Notices of the Royal Astronomical Society* 242 (1, 1990), p. 43. DOI: [10.1093/mnras/242.1.43P](https://doi.org/10.1093/mnras/242.1.43P) (cit. on p. 9).
- [Mas+13] K. W. Masui, E. R. Switzer, N. Banavar, K. Bandura, C. Blake, L.-M. Calin, T.-C. Chang, X. Chen, Y.-C. Li, Y.-W. Liao, A. Natarajan, U.-L. Pen, J. B. Peterson, J. R. Shaw, and T. C. Voytek. "Measurement of 21 Cm Brightness Fluctuations at z 0.8 in Cross-correlation". In: *The Astrophysical Journal Letters* 763.1 (2013), p. L20. DOI: [10.1088/2041-8205/763/1/L20](https://doi.org/10.1088/2041-8205/763/1/L20) (cit. on p. 66).
- [Mat+94] J. C. Mather, E. S. Cheng, D. A. Cottingham, R. E. Eplee Jr., D. J. Fixsen, T. Hewagama, R. B. Isaacman, K. A. Jensen, S. S. Meyer, P. D. Noerdlinger, S. M. Read, L. P. Rosen, R. A. Shafer, E. L. Wright, C. L. Bennett, N. W. Boggess, M. G. Hauser, T. Kellogg, S. H. Moseley Jr., R. F. Silverberg, G. F. Smoot, R. Weiss, and D. T. Wilkinson. "Measurement of the Cosmic Microwave Background Spectrum by the COBE FIRAS Instrument". In: *The Astrophysical Journal* 420 (1, 1994), pp. 439–444. DOI: [10.1086/173574](https://doi.org/10.1086/173574) (cit. on p. 20).
- [McD03] Patrick McDonald. "Toward a Measurement of the Cosmological Geometry at  $z \sim 2$ : Predicting Ly $\alpha$  Forest Correlation in Three Dimensions and the Potential of Future Data Sets". In: *The Astrophysical Journal* 585 (1, 2003), pp. 34–51. DOI: [10.1086/345945](https://doi.org/10.1086/345945) (cit. on p. 30).
- [McD+00] Patrick McDonald, Jordi Miralda-Escudé, Michael Rauch, Wallace L. W. Sargent, Tom A. Barlow, Renyue Cen, and Jeremiah P. Ostriker. "The Observed Probability Distribution Function, Power Spectrum, and Correlation Function of the Transmitted Flux in the Ly $\alpha$  Forest". In: *The Astrophysical Journal* 543 (1, 2000), pp. 1–23. DOI: [10.1086/317079](https://doi.org/10.1086/317079) (cit. on p. 30).
- [McD+06] Patrick McDonald, Uroš Seljak, Scott Burles, David J. Schlegel, David H. Weinberg, Renyue Cen, David Shih, Joop Schaye, Donald P. Schneider, Neta A. Bahcall, John W. Briggs, J. Brinkmann, Robert J. Brunner, Masataka Fukugita, James E. Gunn, Željko Ivezić, Stephen Kent, Robert H. Lupton, and Daniel E. Vanden Berk. "The Ly $\alpha$  Forest Power Spectrum from the Sloan Digital Sky Survey". In: *The Astrophysical Journal Supplement Series* 163 (1, 2006), pp. 80–109. DOI: [10.1086/444361](https://doi.org/10.1086/444361); (cit. on p. 30).
- [McD+05] Patrick McDonald, Uroš Seljak, Renyue Cen, David Shih, David H. Weinberg, Scott Burles, Donald P. Schneider, David J. Schlegel, Neta A. Bahcall, John W. Briggs, J. Brinkmann, Masataka Fukugita, Željko Ivezić, Stephen Kent, and Daniel E. Vanden Berk. "The Linear Theory Power Spectrum from the Ly $\alpha$  Forest in the Sloan Digital Sky Survey". In: *The Astrophysical Journal* 635 (1, 2005), pp. 761–783. DOI: [10.1086/497563](https://doi.org/10.1086/497563) (cit. on p. 30).
- [McQ+06] Matthew McQuinn, Oliver Zahn, Matias Zaldarriaga, Lars Hernquist, and Steven R. Furlanetto. "Cosmological Parameter Estimation Using 21 Cm Radiation from the Epoch of Reionization". In: *The Astrophysical Journal* 653 (1, 2006), pp. 815–834. DOI: [10.1086/505167](https://doi.org/10.1086/505167) (cit. on p. 66).

- [MFC11] Andrei Mesinger, Steven Furlanetto, and Renyue Cen. “21CMFAST: A Fast, Seminumerical Simulation of the High-Redshift 21-Cm Signal”. In: *Monthly Notices of the Royal Astronomical Society* 411.2 (2011), p. 955. DOI: [10.1111/j.1365-2966.2010.17731.x](https://doi.org/10.1111/j.1365-2966.2010.17731.x) (cit. on p. 66).
- [MCR18] R. Benton Metcalf, Rupert A. C. Croft, and Alessandro Romeo. “Noise Estimates for Measurements of Weak Lensing from the Ly  $\alpha$  Forest”. In: *Monthly Notices of the Royal Astronomical Society* 477.2 (2018), p. 2841. DOI: [10.1093/mnras/sty806](https://doi.org/10.1093/mnras/sty806) (cit. on p. 41).
- [MTC20] R. Benton Metcalf, Nicolas Tessore, and Rupert A. C. Croft. “Reconstructing the Gravitational Lensing Potential from the Lyman- $\alpha$  Forest”. In: *Astronomy and Astrophysics* 642 (2020), A122. DOI: [10.1051/0004-6361/202038056](https://doi.org/10.1051/0004-6361/202038056) (cit. on p. 41).
- [Moh+20] Faizan G. Mohammad, Will J. Percival, Hee-Jong Seo, Michael J. Chapman, D. Bianchi, Ashley J. Ross, Cheng Zhao, Dustin Lang, Julian Bautista, Jonathan Brinkmann, Joel R. Brownstein, Etienne Burtin, Chia-Hsun Chuang, Kyle S. Dawson, Sylvain de la Torre, Arnaud de Mattia, Sarah Eftekhari-Zadeh, Sébastien Fromentéau, Héctor Gil-Marín, Jiamin Hou, Eva-Maria Mueller, Richard Neveux, Romain Paviot, Anand Raichoor, Graziano Rossi, Donald P. Schneider, Amélie Tamone, Jeremy L. Tinker, Rita Tojeiro, Mariana Vargas Magaña, and Gong-Bo Zhao. “The Completed SDSS-IV Extended Baryon Oscillation Spectroscopic Survey: Pairwise-Inverse Probability and Angular Correction for Fibre Collisions in Clustering Measurements”. In: *Monthly Notices of the Royal Astronomical Society* 498 (1, 2020), pp. 128–143. DOI: [10.1093/mnras/staa2344](https://doi.org/10.1093/mnras/staa2344) (cit. on p. 53).
- [Mou+00] Jeremy R. Mould, John P. Huchra, Wendy L. Freedman, Robert C. Kennicutt Jr., Laura Ferrarese, Holland C. Ford, Brad K. Gibson, John A. Graham, Shaun M. G. Hughes, Garth D. Illingworth, Daniel D. Kelson, Lucas M. Macri, Barry F. Madore, Shoko Sakai, Kim M. Sebo, Nancy A. Silbermann, and Peter B. Stetson. “The Hubble Space Telescope Key Project on the Extragalactic Distance Scale. XXVIII. Combining the Constraints on the Hubble Constant”. In: *The Astrophysical Journal* 529 (1, 2000), pp. 786–794. DOI: [10.1086/308304](https://doi.org/10.1086/308304) (cit. on p. 9).
- [Mue+21] Eva-Maria Mueller, Mehdi Rezaie, Will J. Percival, Ashley J. Ross, Rossana Ruggeri, Hee-Jong Seo, Hector Gil-Marín, Julian Bautista, Joel R. Brownstein, Kyle Dawson, Axel de la Macorra, Nathalie Palanque-Delabrouille, Graziano Rossi, Donald P. Schneider, and Christophe Yèche. “The Clustering of Galaxies in the Completed SDSS-IV Extended Baryon Oscillation Spectroscopic Survey: Primordial Non-Gaussianity in Fourier Space”. 25, 2021 (cit. on p. 47).
- [Mye+15] Adam D. Myers, Nathalie Palanque-Delabrouille, Abhishek Prakash, Isabelle Pâris, Christophe Yèche, Kyle S. Dawson, Jo Bovy, Dustin Lang, David J. Schlegel, Jeffrey A. Newman, Patrick Petitjean, Jean Paul Kneib, Pierre Laurent, Will J. Percival, Ashley J. Ross, Hee-Jong Seo, Jeremy L. Tinker, Eric Armengaud, Joel Brownstein, Etienne Burtin, Zheng Cai, Johan Comparat, Mansi Kasliwal, Shrinivas R. Kularki, Russ Laher, David Levitan, Cameron K. McBride, Ian D. McGreer, Adam A. Miller, Peter Nugent, Eran Ofek, Graziano Rossi, John Ruan, Donald P. Schneider, Branimir Sesar, Alina Streblyanska, Jason Surace, and for the SDSS-IV/eBOSS collaboration. “The SDSS-IV Extended Baryon Oscillation Spectroscopic Survey:

## Bibliography

- Quasar Target Selection". In: *The Astrophysical Journal Supplement Series* 221.2 (2, 2015), p. 27. DOI: [10.1088/0067-0049/221/2/27](https://doi.org/10.1088/0067-0049/221/2/27) (cit. on p. 25).
- [Nev+20] Richard Neveux, Etienne Burtin, Arnaud de Mattia, Alex Smith, Ashley J. Ross, Jiamin Hou, Julian Bautista, Jonathan Brinkmann, Chia-Hsun Chuang, Kyle S. Dawson, Héctor Gil-Marín, Brad W. Lyke, Axel de la Macorra, Hélion du Mas des Bourboux, Faizan G. Mohammad, Eva-Maria Müller, Adam D. Myers, Jeffrey A. Newman, Will J. Percival, Graziano Rossi, Donald Schneider, M. Vivek, Pauline Zarrouk, Cheng Zhao, and Gong-Bo Zhao. "The Completed SDSS-IV Extended Baryon Oscillation Spectroscopic Survey: BAO and RSD Measurements from the Anisotropic Power Spectrum of the Quasar Sample between Redshift 0.8 and 2.2". In: *Monthly Notices of the Royal Astronomical Society* 499 (1, 2020), pp. 210–229. DOI: [10.1093/mnras/staa2780](https://doi.org/10.1093/mnras/staa2780) (cit. on p. 22).
- [NB00] Adi Nusser and Enzo Branchini. "On the Least Action Principle in Cosmology". In: *Monthly Notices of the Royal Astronomical Society* 313 (1, 2000), pp. 587–595. DOI: [10.1046/j.1365-8711.2000.03261.x](https://doi.org/10.1046/j.1365-8711.2000.03261.x) (cit. on p. 51).
- [ND92] Adi Nusser and Avishai Dekel. "Tracing Large-Scale Fluctuations Back in Time". In: *The Astrophysical Journal* 391 (1, 1992), p. 443. DOI: [10.1086/171360](https://doi.org/10.1086/171360) (cit. on p. 51).
- [Oku+16] Teppei Okumura, Chiaki Hikage, Tomonori Totani, Motonari Tonegawa, Hiroyuki Okada, Karl Glazebrook, Chris Blake, Pedro G. Ferreira, Surhud More, Atsushi Taruya, Shinji Tsujikawa, Masayuki Akiyama, Gavin Dalton, Tomotsugu Goto, Takashi Ishikawa, Fumihide Iwamuro, Takahiko Matsubara, Takahiro Nishimichi, Kouji Ohta, Ik Koh Shimizu, Ryuichi Takahashi, Naruhisa Takato, Naoyuki Tamura, Kiyoto Yabe, and Naoki Yoshida. "The Subaru FMOS Galaxy Redshift Survey (Fast-Sound). IV. New Constraint on Gravity Theory from Redshift Space Distortions at  $z \sim 1.4$ ". In: *Publications of the Astronomical Society of Japan* 68.3 (1, 2016). DOI: [10.1093/pasj/psw029](https://doi.org/10.1093/pasj/psw029) (cit. on p. 20).
- [Pad+08] Nikhil Padmanabhan, David J. Schlegel, Douglas P. Finkbeiner, J. C. Barentine, Michael R. Blanton, Howard J. Brewington, James E. Gunn, Michael Harvanek, David W. Hogg, Željko Ivezić, David Johnston, Stephen M. Kent, S. J. Kleinman, Gillian R. Knapp, Jurek Krzesinski, Dan Long, Eric H. Neilsen Jr., Atsuko Nitta, Craig Loomis, Robert H. Lupton, Sam Roweis, Stephanie A. Snedden, Michael A. Strauss, and Douglas L. Tucker. "An Improved Photometric Calibration of the Sloan Digital Sky Survey Imaging Data". In: *The Astrophysical Journal* 674 (1, 2008), pp. 1217–1233. DOI: [10.1086/524677](https://doi.org/10.1086/524677) (cit. on p. 24).
- [PWC09] Nikhil Padmanabhan, Martin White, and J. D. Cohn. "Reconstructing Baryon Oscillations: A Lagrangian Theory Perspective". In: *Physical Review D* 79 (1, 2009), p. 063523. DOI: [10.1103/PhysRevD.79.063523](https://doi.org/10.1103/PhysRevD.79.063523) (cit. on p. 53).
- [Pad+12] Nikhil Padmanabhan, Xiaoying Xu, Daniel J. Eisenstein, Richard Scalzo, Antonio J. Cuesta, Kushal T. Mehta, and Eyal Kazin. "A 2 per Cent Distance to  $z = 0.35$  by Reconstructing Baryon Acoustic Oscillations - I. Methods and Application to the Sloan Digital Sky Survey". In: *Monthly Notices of the Royal Astronomical Society* 427.3 (2012), p. 2132. DOI: [10.1111/j.1365-2966.2012.21888.x](https://doi.org/10.1111/j.1365-2966.2012.21888.x) (cit. on pp. 51, 53).

## Bibliography

- [Pal+16] N. Palanque-Delabrouille, Ch. Magneville, Ch. Yèche, I. Pâris, P. Petitjean, E. Burtin, K. Dawson, I. McGreer, A. D. Myers, G. Rossi, D. Schlegel, D. Schneider, A. Streblyanska, and J. Tinker. “The Extended Baryon Oscillation Spectroscopic Survey: Variability Selection and Quasar Luminosity Function”. In: *Astronomy and Astrophysics* 587 (1, 2016), A41. DOI: [10.1051/0004-6361/201527392](https://doi.org/10.1051/0004-6361/201527392) (cit. on p. 25).
- [Pal+20] Nathalie Palanque-Delabrouille, Christophe Yèche, Nils Schöneberg, Julien Lesgourgues, Michael Walther, Solène Chabanier, and Eric Armengaud. “Hints, Neutrino Bounds, and WDM Constraints from SDSS DR14 Lyman-\$\upalpha\$ and Planck Full-Survey Data”. In: *Journal of Cosmology and Astroparticle Physics* 2020.04 (2020), pp. 038–038. DOI: [10.1088/1475-7516/2020/04/038](https://doi.org/10.1088/1475-7516/2020/04/038) (cit. on p. 30).
- [Pâr+11] I. Pâris, P. Petitjean, E. Rollinde, E. Aubourg, N. Busca, R. Charlassier, T. Delubac, J.-Ch Hamilton, J.-M. Le Goff, N. Palanque-Delabrouille, S. Peirani, Ch Pichon, J. Rich, M. Vargas-Magaña, and Ch Yèche. “A Principal Component Analysis of Quasar UV Spectra at  $z \sim 3$ ”. In: *Astronomy and Astrophysics* 530 (2011), A50. DOI: [10.1051/0004-6361/201016233](https://doi.org/10.1051/0004-6361/201016233) (cit. on p. 32).
- [Par+12] David Parkinson, Signe Riemer-Sørensen, Chris Blake, Gregory B. Poole, Tamara M. Davis, Sarah Brough, Matthew Colless, Carlos Contreras, Warrick Couch, Scott Croom, Darren Croton, Michael J. Drinkwater, Karl Forster, David Gilbank, Mike Gladders, Karl Glazebrook, Ben Jelliffe, Russell J. Jurek, I.-hui Li, Barry Madore, D. Christopher Martin, Kevin Pimbblet, Michael Pracy, Rob Sharp, Emily Wisnioski, David Woods, Ted K. Wyder, and H. K. C. Yee. “The WiggleZ Dark Energy Survey: Final Data Release and Cosmological Results”. In: *Physical Review D* 86.10 (2012), p. 103518. DOI: [10.1103/PhysRevD.86.103518](https://doi.org/10.1103/PhysRevD.86.103518) (cit. on p. 20).
- [Pav+22] Romain Paviot, Sylvain de la Torre, Arnaud de Mattia, Cheng Zhao, Julian Bautista, Etienne Burtin, Kyle Dawson, Stéphanie Escoffier, Eric Jullo, Anand Raichoor, Ashley J. Ross, and Graziano Rossi. “Angular Systematics-Free Cosmological Analysis of Galaxy Clustering in Configuration Space”. In: *Monthly Notices of the Royal Astronomical Society* 512 (1, 2022), pp. 1341–1356. DOI: [10.1093/mnras/stac560](https://doi.org/10.1093/mnras/stac560) (cit. on p. 34).
- [Pee89] P. J. E. Peebles. “Tracing Galaxy Orbits Back in Time”. In: *The Astrophysical Journal* 344 (1, 1989), p. L53. DOI: [10.1086/185529](https://doi.org/10.1086/185529) (cit. on p. 51).
- [PB17] Will J. Percival and Davide Bianchi. “Using Angular Pair Upweighting to Improve 3D Clustering Measurements”. In: *Monthly Notices of the Royal Astronomical Society: Letters* 472.1 (2017), pp. L40–L44. DOI: [10.1093/mnrasl/slx135](https://doi.org/10.1093/mnrasl/slx135) (cit. on p. 53).
- [Per+99] S. Perlmutter, G. Aldering, G. Goldhaber, R. A. Knop, P. Nugent, P. G. Castro, S. Deustua, S. Fabbro, A. Goobar, D. E. Groom, I. M. Hook, A. G. Kim, M. Y. Kim, J. C. Lee, N. J. Nunes, R. Pain, C. R. Pennypacker, R. Quimby, C. Lidman, R. S. Ellis, M. Irwin, R. G. McMahon, P. Ruiz-Lapuente, N. Walton, B. Schaefer, B. J. Boyle, A. V. Filippenko, T. Matheson, A. S. Fruchter, N. Panagia, H. J. M. Newberg, W. J. Couch, and Supernova Cosmology Project. “Measurements of Omega and Lambda from 42 High-Redshift Supernovae”. In: *The Astrophysical Journal* 517 (1, 1999), pp. 565–586. DOI: [10.1086/307221](https://doi.org/10.1086/307221) (cit. on p. 9).

- [Pez+17] A. Pezzotta, S. de la Torre, J. Bel, B. R. Granett, L. Guzzo, J. A. Peacock, B. Garilli, M. Scudegger, M. Bolzonella, U. Abbas, C. Adami, D. Bottini, A. Cappi, O. Cucciati, I. Davidzon, P. Franzetti, A. Fritz, A. Iovino, J. Krywult, V. Le Brun, O. Le Fèvre, D. Maccagni, K. Małek, F. Marulli, M. Polletta, A. Pollo, L. a. M. Tasca, R. Tojeiro, D. Vergani, A. Zanichelli, S. Arnouts, E. Branchini, J. Coupon, G. De Lucia, J. Koda, O. Ilbert, F. Mohammad, T. Moutard, and L. Moscardini. “The VIMOS Public Extragalactic Redshift Survey (VIPERS). The Growth of Structure at  $0.5 < z < 1.2$  from Redshift-Space Distortions in the Clustering of the PDR-2 Final Sample”. In: *Astronomy and Astrophysics* 604 (2017), A33. DOI: [10.1051/0004-6361/201630295](https://doi.org/10.1051/0004-6361/201630295) (cit. on p. 20).
- [Pit+21] Cyril Pitrou, Alain Coc, Jean-Philippe Uzan, and Elisabeth Vangioni. “A New Tension in the Cosmological Model from Primordial Deuterium?” In: *Monthly Notices of the Royal Astronomical Society* 502.2 (10, 2021), pp. 2474–2481. DOI: [10.1093/mnras/stab135](https://doi.org/10.1093/mnras/stab135) (cit. on p. 19).
- [Pla+20] Planck Collaboration et al. “Planck 2018 Results. VI. Cosmological Parameters”. In: *Astronomy and Astrophysics* 641 (1, 2020), A6. DOI: [10.1051/0004-6361/201833910](https://doi.org/10.1051/0004-6361/201833910) (cit. on p. 21).
- [PM14] A. Pourtsidou and R. Benton Metcalf. “Weak Lensing with 21 Cm Intensity Mapping at  $z \sim 2\text{--}3$ ”. In: *Monthly Notices of the Royal Astronomical Society* 439 (1, 2014), pp. L36–L40. DOI: [10.1093/mnrasl/slt175](https://doi.org/10.1093/mnrasl/slt175) (cit. on p. 41).
- [PM15] A. Pourtsidou and R. Benton Metcalf. “Gravitational Lensing of Cosmological 21 Cm Emission”. In: *Monthly Notices of the Royal Astronomical Society* 448 (1, 2015), pp. 2368–2383. DOI: [10.1093/mnras/stv102](https://doi.org/10.1093/mnras/stv102) (cit. on p. 41).
- [Pra+16] Abhishek Prakash, Timothy C. Licquia, Jeffrey A. Newman, Ashley J. Ross, Adam D. Myers, Kyle S. Dawson, Jean-Paul Kneib, Will J. Percival, Julian E. Bautista, Johan Comparat, Jeremy L. Tinker, David J. Schlegel, Rita Tojeiro, Shirley Ho, Dustin Lang, Sandhya M. Rao, Cameron K. McBride, Guangtun Ben Zhu, Joel R. Brownstein, Stephen Bailey, Adam S. Bolton, Timothée Delubac, Vivek Mariappan, Michael R. Blanton, Beth Reid, Donald P. Schneider, Hee-Jong Seo, Aurelio Carnero Rosell, and Francisco Prada. “The SDSS-IV Extended Baryon Oscillation Spectroscopic Survey: Luminous Red Galaxy Target Selection”. In: *The Astrophysical Journal Supplement Series* 224 (1, 2016), p. 34. DOI: [10.3847/0067-0049/224/2/34](https://doi.org/10.3847/0067-0049/224/2/34) (cit. on pp. 25, 47).
- [Rai+17] A. Raichoor, J. Comparat, T. Delubac, J.-P. Kneib, Ch Yèche, K. S. Dawson, W. J. Percival, A. Dey, D. Lang, D. J. Schlegel, C. Gorgoni, J. Bautista, J. R. Brownstein, V. Mariappan, H.-J. Seo, J. L. Tinker, A. J. Ross, Y. Wang, G.-B. Zhao, J. Moustakas, N. Palanque-Delabrouille, E. Jullo, J. A. Newmann, F. Prada, and G. B. Zhu. “The SDSS-IV Extended Baryon Oscillation Spectroscopic Survey: Final Emission Line Galaxy Target Selection”. In: *Monthly Notices of the Royal Astronomical Society* 471 (1, 2017), pp. 3955–3973. DOI: [10.1093/mnras/stx1790](https://doi.org/10.1093/mnras/stx1790) (cit. on p. 25).
- [Rai+20] Anand Raichoor, Arnaud de Mattia, Ashley J Ross, Cheng Zhao, Shadab Alam, Santiago Avila, Julian Bautista, Jonathan Brinkmann, Joel R Brownstein, Etienne Burtin, Michael J Chapman, Chia-Hsun Chuang, Johan Comparat, Kyle S Dawson, Arjun Dey, Hélion du Mas des Bourboux, Jack Elvin-Poole, Violeta Gonzalez-Perez, Claudio Gorgoni, Jean-Paul Kneib, Hui Kong, Dustin Lang, John Moustakas,

- Adam D Myers, Eva-Maria Müller, Seshadri Nadathur, Jeffrey A Newman, Will J Percival, Mehdi Rezaie, Graziano Rossi, Vanina Ruhlmann-Kleider, David J Schlegel, Donald P Schneider, Hee-Jong Seo, Amélie Tamone, Jeremy L Tinker, Rita Tojeiro, M Vivek, Christophe Yèche, and Gong-Bo Zhao. “The Completed SDSS-IV Extended Baryon Oscillation Spectroscopic Survey: Large-Scale Structure Catalogues and Measurement of the Isotropic BAO between Redshift 0.6 and 1.1 for the Emission Line Galaxy Sample”. In: *Monthly Notices of the Royal Astronomical Society* 500.3 (11, 2020), pp. 3254–3274. DOI: [10.1093/mnras/staa3336](https://doi.org/10.1093/mnras/staa3336) (cit. on p. 66).
- [Rav+22] Corentin Ravoux, Eric Armengaud, Julian Bautista, Jean-Marc Le Goff, Nathalie Palanque-Delabrouille, James Rich, Michael Walther, and Christophe Yèche. “First Measurement of the Correlation between Cosmic Voids and the Lyman-\$\alpha\$ Forest”. 21, 2022 (cit. on p. 44).
- [Rei+16] Beth Reid, Shirley Ho, Nikhil Padmanabhan, Will J. Percival, Jeremy Tinker, Rita Tojeiro, Martin White, Daniel J. Eisenstein, Claudia Maraston, Ashley J. Ross, Ariel G. Sánchez, David Schlegel, Erin Sheldon, Michael A. Strauss, Daniel Thomas, David Wake, Florian Beutler, Dmitry Bizyaev, Adam S. Bolton, Joel R. Brownstein, Chia-Hsun Chuang, Kyle Dawson, Paul Harding, Francisco-Shu Kitaura, Alexie Leauthaud, Karen Masters, Cameron K. McBride, Surhud More, Matthew D. Olmstead, Daniel Oravetz, Sebastián E. Nuza, Kaike Pan, John Parejko, Janine Pforr, Francisco Prada, Sergio Rodríguez-Torres, Salvador Salazar-Albornoz, Lado Samushia, Donald P. Schneider, Claudia G. Scóccola, Audrey Simmons, and Mariana Vargas-Magana. “SDSS-III Baryon Oscillation Spectroscopic Survey Data Release 12: Galaxy Target Selection and Large-Scale Structure Catalogues”. In: *Monthly Notices of the Royal Astronomical Society* 455 (1, 2016), pp. 1553–1573. DOI: [10.1093/mnras/stv2382](https://doi.org/10.1093/mnras/stv2382) (cit. on p. 25).
- [RPR19] M. J. Reid, D. W. Pesce, and A. G. Riess. “An Improved Distance to NGC 4258 and Its Implications for the Hubble Constant”. In: *The Astrophysical Journal* 886.2 (2019), p. L27. DOI: [10.3847/2041-8213/ab552d](https://doi.org/10.3847/2041-8213/ab552d) (cit. on p. 17).
- [Rez+21] Mehdi Rezaie, Ashley J. Ross, Hee-Jong Seo, Eva-Maria Mueller, Will J. Percival, Grant Merz, Reza Katebi, Razvan C. Bunescu, Julian Bautista, Joel R. Brownstein, Etienne Burtin, Kyle Dawson, Héctor Gil-Marín, Jiamin Hou, Eleanor B. Lyke, Axel de la Macorra, Graziano Rossi, Donald P. Schneider, Pauline Zarrouk, and Gong-Bo Zhao. “Primordial Non-Gaussianity from the Completed SDSS-IV Extended Baryon Oscillation Spectroscopic Survey I: Catalogue Preparation and Systematic Mitigation”. In: *Monthly Notices of the Royal Astronomical Society* 506.3 (28, 2021), pp. 3439–3454. DOI: [10.1093/mnras/stab1730](https://doi.org/10.1093/mnras/stab1730) (cit. on p. 47).
- [Rez+20] Mehdi Rezaie, Hee-Jong Seo, Ashley J. Ross, and Razvan C. Bunescu. “Improving Galaxy Clustering Measurements with Deep Learning: Analysis of the DECaLS DR7 Data”. In: *Monthly Notices of the Royal Astronomical Society* 495 (1, 2020), pp. 1613–1640. DOI: [10.1093/mnras/staa1231](https://doi.org/10.1093/mnras/staa1231) (cit. on p. 47).
- [Rie20] Adam G. Riess. “The Expansion of the Universe Is Faster than Expected”. In: *Nature Reviews Physics* 2.1 (2020), pp. 10–12. DOI: [10.1038/s42254-019-0137-0](https://doi.org/10.1038/s42254-019-0137-0) (cit. on p. 16).

## Bibliography

- [Rie+21] Adam G. Riess, Stefano Casertano, Wenlong Yuan, J. Bradley Bowers, Lucas Macri, Joel C. Zinn, and Dan Scolnic. “Cosmic Distances Calibrated to 1% Precision with Gaia EDR3 Parallaxes and Hubble Space Telescope Photometry of 75 Milky Way Cepheids Confirm Tension with  $\Omega$ ”. In: 908.1 (2021), p. L6. DOI: [10.3847/2041-8213/abdbaf](https://doi.org/10.3847/2041-8213/abdbaf) (cit. on p. 16).
- [Rie+98] Adam G. Riess, Alexei V. Filippenko, Peter Challis, Alejandro Clocchiatti, Alan Diercks, Peter M. Garnavich, Ron L. Gilliland, Craig J. Hogan, Saurabh Jha, Robert P. Kirshner, B. Leibundgut, M. M. Phillips, David Reiss, Brian P. Schmidt, Robert A. Schommer, R. Chris Smith, J. Spyromilio, Christopher Stubbs, Nicholas B. Suntzeff, and John Tonry. “Observational Evidence from Supernovae for an Accelerating Universe and a Cosmological Constant”. In: *The Astronomical Journal* 116 (1, 1998), pp. 1009–1038. DOI: [10.1086/300499](https://doi.org/10.1086/300499) (cit. on p. 9).
- [Rog+18] Keir K. Rogers, Simeon Bird, Hiranya V. Peiris, Andrew Pontzen, Andreu Font-Ribera, and Boris Leistedt. “Correlations in the Three-Dimensional Lyman-alpha Forest Contaminated by High Column Density Absorbers”. In: *Monthly Notices of the Royal Astronomical Society* 476.3 (2018), p. 3716. DOI: [10.1093/mnras/sty603](https://doi.org/10.1093/mnras/sty603) (cit. on p. 35).
- [Ros+20] Ashley J. Ross, Julian Bautista, Rita Tojeiro, Shadab Alam, Stephen Bailey, Etienne Burtin, Johan Comparat, Kyle S. Dawson, Arnaud de Mattia, Hélion du Mas des Bourboux, Héctor Gil-Marín, Jiamin Hou, Hui Kong, Brad W. Lyke, Faizan G. Mohammad, John Moustakas, Eva-Maria Mueller, Adam D. Myers, Will J. Percival, Anand Raichoor, Mehdi Rezaie, Hee-Jong Seo, Alex Smith, Jeremy L. Tinker, Pauline Zarrouk, Cheng Zhao, Gong-Bo Zhao, Dmitry Bizyaev, Jonathan Brinkmann, Joel R. Brownstein, Aurelio Carnero Rosell, Solène Chabanier, Peter D. Choi, Chia-Hsun Chuang, Irene Cruz-Gonzalez, Axel de la Macorra, Sylvain de la Torre, Stephanie Escoffier, Sébastien Fromenteau, Alexandra Higley, Eric Jullo, Jean-Paul Kneib, Jacob N. McLane, Andrea Muñoz-Gutiérrez, Richard Neveux, Jeffrey A. Newman, Christian Nitschelm, Nathalie Palanque-Delabrouille, Romain Paviot, Anthony R. Pullen, Graziano Rossi, Vanina Ruhlmann-Kleider, Donald P. Schneider, Mariana Vargas Magaña, M. Vivek, and Yucheng Zhang. “The Completed SDSS-IV Extended Baryon Oscillation Spectroscopic Survey: Large-scale Structure Catalogues for Cosmological Analysis”. In: *Monthly Notices of the Royal Astronomical Society* 498 (1, 2020), pp. 2354–2371. DOI: [10.1093/mnras/staa2416](https://doi.org/10.1093/mnras/staa2416) (cit. on pp. 45, 48).
- [Ros+12] Nicholas P. Ross, Adam D. Myers, Erin S. Sheldon, Christophe Yèche, Michael A. Strauss, Jo Bovy, Jessica A. Kirkpatrick, Gordon T. Richards, Éric Aubourg, Michael R. Blanton, W. N. Brandt, William C. Carithers, Rupert A. C. Croft, Robert da Silva, Kyle Dawson, Daniel J. Eisenstein, Joseph F. Hennawi, Shirley Ho, David W. Hogg, Khee-Gan Lee, Britt Lundgren, Richard G. McMahon, Jordi Miralda-Escudé, Nathalie Palanque-Delabrouille, Isabelle Pâris, Patrick Petitjean, Matthew M. Pieri, James Rich, Natalie A. Roe, David Schiminovich, David J. Schlegel, Donald P. Schneider, Anže Slosar, Nao Suzuki, Jeremy L. Tinker, David H. Weinberg, Anya Weyant, Martin White, and W. Michael Wood-Vasey. “The SDSS-III Baryon Oscillation Spectroscopic Survey: Quasar Target Selection for Data Release Nine”. In: *The Astrophysical Journal Supplement Series* 199.1 (2012), p. 3. DOI: [10.1088/0067-0049/199/1/3](https://doi.org/10.1088/0067-0049/199/1/3) (cit. on p. 25).

## Bibliography

- [Sán20] Ariel G. Sánchez. “Arguments against Using  $\hat{h}$  Mpc Units in Observational Cosmology”. In: *Physical Review D* 102.12 (2, 2020), p. 123511. DOI: [10.1103/PhysRevD.102.123511](https://doi.org/10.1103/PhysRevD.102.123511) (cit. on pp. 16, 61).
- [Sán+17] Ariel G. Sánchez, Jan Niklas Grieb, Salvador Salazar-Albornoz, Shadab Alam, Florian Beutler, Ashley J. Ross, Joel R. Brownstein, Chia-Hsun Chuang, Antonio J. Cuesta, Daniel J. Eisenstein, Francisco-Shu Kitaura, Will J. Percival, Francisco Prada, Sergio Rodríguez-Torres, Hee-Jong Seo, Jeremy Tinker, Rita Tojeiro, Mariana Vargas-Magaña, Jose A. Vazquez, and Gong-Bo Zhao. “The Clustering of Galaxies in the Completed SDSS-III Baryon Oscillation Spectroscopic Survey: Combining Correlated Gaussian Posterior Distributions”. In: *Monthly Notices of the Royal Astronomical Society* 464.2 (2017), p. 1493. DOI: [10.1093/mnras/stw2495](https://doi.org/10.1093/mnras/stw2495) (cit. on pp. 62, 64).
- [Sar+19] E. Sarpa, C. Schimd, E. Branchini, and S. Matarrese. “BAO Reconstruction: A Swift Numerical Action Method for Massive Spectroscopic Surveys”. In: *Monthly Notices of the Royal Astronomical Society* 484 (1, 2019), pp. 3818–3830. DOI: [10.1093/mnras/stz278](https://doi.org/10.1093/mnras/stz278) (cit. on p. 51).
- [Sar+21] E. Sarpa, A. Veropalumbo, C. Schimd, E. Branchini, and S. Matarrese. “Extended Fast Action Minimization Method: Application to SDSS-DR12 Combined Sample”. In: *Monthly Notices of the Royal Astronomical Society* 503 (1, 2021), pp. 540–556. DOI: [10.1093/mnras/stab378](https://doi.org/10.1093/mnras/stab378) (cit. on p. 51).
- [Sco+18] D. M. Scolnic, D. O. Jones, A. Rest, Y. C. Pan, R. Chornock, R. J. Foley, M. E. Huber, R. Kessler, G. Narayan, A. G. Riess, S. Rodney, E. Berger, D. J. Brout, P. J. Challis, M. Drout, D. Finkbeiner, R. Lunnan, R. P. Kirshner, N. E. Sanders, E. Schlafly, S. Smartt, C. W. Stubbs, J. Tonry, W. M. Wood-Vasey, M. Foley, J. Hand, E. Johnson, W. S. Burgett, K. C. Chambers, P. W. Draper, K. W. Hodapp, N. Kaiser, R. P. Kudritzki, E. A. Magnier, N. Metcalfe, F. Bresolin, E. Gall, R. Kotak, M. McCrum, and K. W. Smith. “The Complete Light-curve Sample of Spectroscopically Confirmed SNe Ia from Pan-STARRS1 and Cosmological Constraints from the Combined Pantheon Sample”. In: *The Astrophysical Journal* 859 (1, 2018), p. 101. DOI: [10.3847/1538-4357/aab9bb](https://doi.org/10.3847/1538-4357/aab9bb) (cit. on p. 18).
- [Sef+16] E. Sefusatti, M. Crocce, R. Scoccimarro, and H. M. P. Couchman. “Accurate Estimators of Correlation Functions in Fourier Space”. In: *Monthly Notices of the Royal Astronomical Society* 460 (1, 2016), pp. 3624–3636. DOI: [10.1093/mnras/stw1229](https://doi.org/10.1093/mnras/stw1229) (cit. on p. 54).
- [Seo+16] Hee-Jong Seo, Florian Beutler, Ashley J. Ross, and Shun Saito. “Modeling the Reconstructed BAO in Fourier Space”. In: *Monthly Notices of the Royal Astronomical Society* 460.3 (11, 2016), pp. 2453–2471. DOI: [10.1093/mnras/stw1138](https://doi.org/10.1093/mnras/stw1138) (cit. on p. 57).
- [Seo+10] Hee-Jong Seo, Jonathan Eckel, Daniel J. Eisenstein, Kushal Mehta, Marc Metchnik, Nikhil Padmanabhan, Phillip Pinto, Ryuichi Takahashi, Martin White, and Xiaoying Xu. “High-Precision Predictions for the Acoustic Scale in the Nonlinear Regime”. In: *The Astrophysical Journal* 720 (1, 2010), pp. 1650–1667. DOI: [10.1088/0004-637X/720/2/1650](https://doi.org/10.1088/0004-637X/720/2/1650) (cit. on p. 51).

## Bibliography

- [She+16] Yue Shen, W. N. Brandt, Gordon T. Richards, Kelly D. Denney, Jenny E. Greene, C. J. Grier, Luis C. Ho, Bradley M. Peterson, Patrick Petitjean, Donald P. Schneider, Charling Tao, and Jonathan R. Trump. “The Sloan Digital Sky Survey Reverberation Mapping Project: Velocity Shifts of Quasar Emission Lines”. In: *The Astrophysical Journal* 831.1 (2016), p. 7. DOI: [10.3847/0004-637X/831/1/7](https://doi.org/10.3847/0004-637X/831/1/7) (cit. on p. 38).
- [Slo+11] Anže Slosar, Andreu Font-Ribera, Matthew M. Pieri, James Rich, Jean-Marc Le Goff, Éric Aubourg, Jon Brinkmann, Nicolas Busca, Bill Carithers, Romain Charlaisier, Marina Cortês, Rupert Croft, Kyle S. Dawson, Daniel Eisenstein, Jean-Christophe Hamilton, Shirley Ho, Khee-Gan Lee, Robert Lupton, Patrick McDonald, Bumbarija Medolin, Demitri Muna, Jordi Miralda-Escudé, Adam D. Myers, Robert C. Nichol, Nathalie Palanque-Delabrouille, Isabelle Pâris, Patrick Petitjean, Yodovina Piškur, Emmanuel Rollinde, Nicholas P. Ross, David J. Schlegel, Donald P. Schneider, Erin Sheldon, Benjamin A. Weaver, David H. Weinberg, Christophe Yèche, and Donald G. York. “The Lyman-\$\alpha\$ Forest in Three Dimensions: Measurements of Large Scale Flux Correlations from BOSS 1st-Year Data”. In: *Journal of Cosmology and Astroparticle Physics* 2011.9 (2011), p. 001. DOI: [10.1088/1475-7516/2011/09/001](https://doi.org/10.1088/1475-7516/2011/09/001) (cit. on p. 31).
- [Slo+13] Anže Slosar, Vid Iršič, David Kirkby, Stephen Bailey, Nicolás G. Busca, Timothée Delubac, James Rich, Éric Aubourg, Julian E. Bautista, Vaishali Bhardwaj, Michael Blomqvist, Adam S. Bolton, Jo Bovy, Joel Brownstein, Bill Carithers, Rupert A. C. Croft, Kyle S. Dawson, Andreu Font-Ribera, J.-M. Le Goff, Shirley Ho, Klaus Honscheid, Khee-Gan Lee, Daniel Margala, Patrick McDonald, Bumbarija Medolin, Jordi Miralda-Escudé, Adam D. Myers, Robert C. Nichol, Pasquier Noterdaeme, Nathalie Palanque-Delabrouille, Isabelle Pâris, Patrick Petitjean, Matthew M. Pieri, Yodovina Piškur, Natalie A. Roe, Nicholas P. Ross, Graziano Rossi, David J. Schlegel, Donald P. Schneider, Nao Suzuki, Erin S. Sheldon, Uroš Seljak, Matteo Viel, David H. Weinberg, and Christophe Yèche. “Measurement of Baryon Acoustic Oscillations in the Lyman-\$\alpha\$ Forest Fluctuations in BOSS Data Release 9”. In: *Journal of Cosmology and Astro-Particle Physics* 04 (1, 2013), p. 026. DOI: [10.1088/1475-7516/2013/04/026](https://doi.org/10.1088/1475-7516/2013/04/026); (cit. on p. 31).
- [Squ+20] Square Kilometre Array Cosmology Science Working Group, David J. Bacon, Richard A. Battye, Philip Bull, Stefano Camera, Pedro G. Ferreira, Ian Harrison, David Parkinson, Alkistis Pourtsidou, Mário G. Santos, Laura Wolz, Filipe Abdalla, Yashar Akrami, David Alonso, Sambatra Andrianomena, Mario Ballardini, José Luis Bernal, Daniele Bertacca, Carlos A. P. Bengaly, Anna Bonaldi, Camille Bonvin, Michael L. Brown, Emma Chapman, Song Chen, Xuelei Chen, Steven Cunningham, Tamara M. Davis, Clive Dickinson, José Fonseca, Keith Grainge, Stuart Harper, Matt J. Jarvis, Roy Maartens, Natasha Maddox, Hamsa Padmanabhan, Jonathan R. Pritchard, Alvise Raccanelli, Marzia Rivi, Sambit Roychowdhury, Martin Sahlén, Dominik J. Schwarz, Thilo M. Siewert, Matteo Viel, Francisco Villaescusa-Navarro, Yidong Xu, Daisuke Yamauchi, and Joe Zuntz. “Cosmology with Phase 1 of the Square Kilometre Array Red Book 2018: Technical Specifications and Performance Forecasts”. In: *Publications of the Astronomical Society of Australia* 37 (1, 2020), e007. DOI: [10.1017/pasa.2019.51](https://doi.org/10.1017/pasa.2019.51) (cit. on p. 68).

- [Str+02] Michael A. Strauss, David H. Weinberg, Robert H. Lupton, Vijay K. Narayanan, James Annis, Mariangela Bernardi, Michael Blanton, Scott Burles, A. J. Connolly, Julianne Dalcanton, Mamoru Doi, Daniel Eisenstein, Joshua A. Frieman, Masataka Fukugita, James E. Gunn, Željko Ivezić, Stephen Kent, Rita S. J. Kim, G. R. Knapp, Richard G. Kron, Jeffrey A. Munn, Heidi Jo Newberg, R. C. Nichol, Sadanori Okamura, Thomas R. Quinn, Michael W. Richmond, David J. Schlegel, Kazuhiro Shimasaku, Mark SubbaRao, Alexander S. Szalay, Dan Vanden Berk, Michael S. Vogeley, Brian Yanny, Naoki Yasuda, Donald G. York, and Idit Zehavi. “Spectroscopic Target Selection in the Sloan Digital Sky Survey: The Main Galaxy Sample”. In: *The Astronomical Journal* 124 (1, 2002), pp. 1810–1824. DOI: [10.1086/342343](https://doi.org/10.1086/342343) (cit. on p. 25).
- [Tam+20] Amélie Tamone, Anand Raichoor, Cheng Zhao, Arnaud de Mattia, Claudio Gorgoni, Etienne Burtin, Vanina Ruhlmann-Kleider, Ashley J. Ross, Shadab Alam, Will J. Percival, Santiago Avila, Michael J. Chapman, Chia-Hsun Chuang, Johan Comparat, Kyle S. Dawson, Sylvain de la Torre, Hélion du Mas des Bourboux, Stephanie Escoffier, Violeta Gonzalez-Perez, Jiamin Hou, Jean-Paul Kneib, Faizan G. Mohammad, Eva-Maria Mueller, Romain Paviot, Graziano Rossi, Donald P. Schneider, Yuting Wang, and Gong-Bo Zhao. “The Completed SDSS-IV Extended Baryon Oscillation Spectroscopic Survey: Growth Rate of Structure Measurement from Anisotropic Clustering Analysis in Configuration Space between Redshift 0.6 and 1.1 for the Emission Line Galaxy Sample”. In: *Monthly Notices of the Royal Astronomical Society* (1, 2020). DOI: [10.1093/mnras/staa3050](https://doi.org/10.1093/mnras/staa3050) (cit. on pp. 22, 49).
- [Tar+12] Atsushi Taruya, Francis Bernardeau, Takahiro Nishimichi, and Sandrine Codis. “Direct and Fast Calculation of Regularized Cosmological Power Spectrum at Two-Loop Order”. In: *Physical Review D* 86 (1, 2012), p. 103528. DOI: [10.1103/PhysRevD.86.103528](https://doi.org/10.1103/PhysRevD.86.103528) (cit. on p. 59).
- [TNS10] Atsushi Taruya, Takahiro Nishimichi, and Shun Saito. “Baryon Acoustic Oscillations in 2D: Modeling Redshift-Space Power Spectrum from Perturbation Theory”. In: *Physical Review D* 82 (1, 2010), p. 063522. DOI: [10.1103/PhysRevD.82.063522](https://doi.org/10.1103/PhysRevD.82.063522) (cit. on p. 59).
- [Vil+18] Francisco Villaescusa-Navarro, Shy Genel, Emanuele Castorina, Andrej Obuljen, David N. Spergel, Lars Hernquist, Dylan Nelson, Isabella P. Carucci, Annalisa Pillepich, Federico Marinacci, Benedikt Diemer, Mark Vogelsberger, Rainer Weinberger, and Rüdiger Pakmor. “Ingredients for 21 Cm Intensity Mapping”. In: *The Astrophysical Journal* 866.2 (2018), p. 135. DOI: [10.3847/1538-4357/aadba0](https://doi.org/10.3847/1538-4357/aadba0) (cit. on p. 66).
- [WRW14] Lile Wang, Beth Reid, and Martin White. “An Analytic Model for Redshift-Space Distortions”. In: *Monthly Notices of the Royal Astronomical Society* 437 (1, 2014), pp. 588–599. DOI: [10.1093/mnras/stt1916](https://doi.org/10.1093/mnras/stt1916) (cit. on p. 59).
- [Wei+13] David H. Weinberg, Michael J. Mortonson, Daniel J. Eisenstein, Christopher Hirata, Adam G. Riess, and Eduardo Rozo. “Observational Probes of Cosmic Acceleration”. In: *Physics Reports* 530.2 (10, 2013), pp. 87–255. DOI: [10.1016/j.physrep.2013.05.001](https://doi.org/10.1016/j.physrep.2013.05.001) (cit. on p. 12).

## Bibliography

- [Wol+22] Laura Wolz, Alkistis Pourtsidou, Kiyoshi W. Masui, Tzu-Ching Chang, Julian E. Bautista, Eva-Maria Müller, Santiago Avila, David Bacon, Will J. Percival, Steven Cunnington, Chris Anderson, Xuelei Chen, Jean-Paul Kneib, Yi-Chao Li, Yu-Wei Liao, Ue-Li Pen, Jeffrey B. Peterson, Graziano Rossi, Donald P. Schneider, Jaswant Yadav, and Gong-Bo Zhao. “H I Constraints from the Cross-Correlation of eBOSS Galaxies and Green Bank Telescope Intensity Maps”. In: *Monthly Notices of the Royal Astronomical Society* 510 (1, 2022), pp. 3495–3511. DOI: [10.1093/mnras/stab3621](https://doi.org/10.1093/mnras/stab3621) (cit. on pp. 66–68).
- [Won+19] Kenneth C. Wong, Sherry H. Suyu, Geoff C.-F. Chen, Cristian E. Rusu, Martin Millon, Dominique Sluse, Vivien Bonvin, Christopher D. Fassnacht, Stefan Taubenberger, Matthew W. Auger, Simon Birrer, James H. H. Chan, Frederic Courbin, Stefan Hilbert, Olga Tihhonova, Tommaso Treu, Adriano Agnello, Xuheng Ding, Inh Jee, Eiichiro Komatsu, Anowar J. Shajib, Alessandro Sonnenfeld, Roger D. Blandford, Léon V. E. Koopmans, Philip J. Marshall, and Georges Meylan. “H0LiCOW - XIII. A 2.4 per Cent Measurement of H0 from Lensed Quasars: 5.3sigma Tension between Early- and Late-Universe Probes”. In: *Monthly Notices of the Royal Astronomical Society* 498 (1, 2019), pp. 1420–1439. DOI: [10.1093/mnras/stz3094](https://doi.org/10.1093/mnras/stz3094) (cit. on p. 17).
- [Yor+00] Donald G. York et al. “The Sloan Digital Sky Survey: Technical Summary”. In: *The Astronomical Journal* 120 (1, 2000), pp. 1579–1587. DOI: [10.1086/301513](https://doi.org/10.1086/301513) (cit. on p. 24).
- [You+22] Samantha Youles, Julian E. Bautista, Andreu Font-Ribera, David Bacon, James Rich, David Brooks, Tamara M. Davis, Kyle Dawson, Govinda Dhungana, Peter Doel, Kevin Fanning, Enrique Gaztañaga, Satya Gontcho A. Gontcho, Alma X. Gonzalez-Morales, Julien Guy, Klaus Honscheid, Vid Iršič, Robert Kehoe, David Kirkby, Theodore Kisner, Martin Landriau, Laurent Le Guillou, Michael E. Levi, Axel de la Macorra, Paul Martini, Andrea Muñoz-Gutiérrez, Nathalie Palanque-Delabrouille, Ignasi Pérez-Ràfols, Claire Poppett, César Ramírez-Pérez, Michael Schubnell, Gregory Tarlé, and Michael Walther. “The Effect of Quasar Redshift Errors on Lyman-\$\alpha\$ Forest Correlation Functions”. 13, 2022. DOI: [10.48550/arXiv.2205.06648](https://arxiv.org/abs/2205.06648) (cit. on pp. 35, 38, 40).
- [Zar+18] Pauline Zarrouk, Etienne Burtin, Héctor Gil-Marín, Ashley J. Ross, Rita Tojeiro, Isabelle Pâris, Kyle S. Dawson, Adam D. Myers, Will J. Percival, Chia-Hsun Chuang, Gong-Bo Zhao, Julian Bautista, Johan Comparat, Violeta González-Pérez, Salman Habib, Katrin Heitmann, Jiamin Hou, Pierre Laurent, Jean-Marc Le Goff, Francisco Prada, Sergio A. Rodríguez-Torres, Graziano Rossi, Rossana Ruggieri, Ariel G. Sánchez, Donald P. Schneider, Jeremy L. Tinker, Yuting Wang, Christophe Yèche, Falk Baumgarten, Joel R. Brownstein, Sylvain de la Torre, Hélion du Mas des Bourboux, Jean-Paul Kneib, Vivek Mariappan, Nathalie Palanque-Delabrouille, John Peacock, Patrick Petitjean, Hee-Jong Seo, and Cheng Zhao. “The Clustering of the SDSS-IV Extended Baryon Oscillation Spectroscopic Survey DR14 Quasar Sample: Measurement of the Growth Rate of Structure from the Anisotropic Correlation Function between Redshift 0.8 and 2.2”. In: *Monthly Notices of the Royal Astronomical Society* 477 (1, 2018), pp. 1639–1663. DOI: [10.1093/mnras/sty506](https://doi.org/10.1093/mnras/sty506) (cit. on p. 38).

## Bibliography

- [Zel70] Ya B. Zel'dovich. “Gravitational Instability: An Approximate Theory for Large Density Perturbations.” In: *Astronomy and Astrophysics* 5 (1970), pp. 84–89 (cit. on p. 51).
- [Zha+21] Cheng Zhao, Chia-Hsun Chuang, Julian Bautista, Arnaud de Mattia, Anand Rai-choor, Ashley J. Ross, Jiamin Hou, Richard Neveux, Charling Tao, Etienne Burtin, Kyle S. Dawson, Sylvain de la Torre, Héctor Gil-Marín, Jean-Paul Kneib, Will J. Percival, Graziano Rossi, Amélie Tamone, Jeremy L. Tinker, Gong-Bo Zhao, Shadab Alam, and Eva-Maria Mueller. “The Completed SDSS-IV Extended Baryon Oscillation Spectroscopic Survey: 1000 Multi-Tracer Mock Catalogues with Redshift Evolution and Systematics for Galaxies and Quasars of the Final Data Release”. In: *Monthly Notices of the Royal Astronomical Society* 503 (1, 2021), pp. 1149–1173. DOI: [10.1093/mnras/stab510](https://doi.org/10.1093/mnras/stab510) (cit. on pp. 45, 46, 50, 52).